5-2022

Railcar Wheel Impact Detection Utilizing Vibration-Based Wireless Onboard Condition Monitoring Modules

Marco A. Barrera
The University of Texas Rio Grande Valley

Recommended Citation

Barrera, Marco A., "Railcar Wheel Impact Detection Utilizing Vibration-Based Wireless Onboard Condition Monitoring Modules" (2022). *Theses and Dissertations*. 826.
https://scholarworks.utrgv.edu/etd/826

RAILCAR WHEEL IMPACT DETECTION UTILIZING VIBRATION-BASED WIRELESS ONBOARD CONDITION MONITORING MODULES

A Thesis

by

MARCO A. BARRERA

Submitted in Partial Fulfillment of the

Requirements for the Degree of

MASTER OF SCIENCE IN ENGINEERING

Major Subject: Mechanical Engineering

The University of Texas Rio Grande Valley

May 2022

RAILCAR WHEEL IMPACT DETECTION UTILIZING VIBRATION-BASED WIRELESS ONBOARD CONDITION MONITORING MODULES

A Thesis
by
MARCO A. BARRERA

COMMITTEE MEMBERS

Dr. Constantine Tarawneh
Chair of Committee

Dr. Heinrich Foltz
Committee Member

Dr. Arturo Fuentes
Committee Member

Dr. Stephen Crown
Committee Member

May 2022

ABSTRACT

Barrera, Marco A., Railcar Wheel Impact Detection Utilizing Vibration-Based Wireless Onboard Condition Monitoring Modules. Master of Science in Engineering (MSE), May, 2022, 113 pp., 20 tables, 52 figures, references, 51 titles.

The current limitations in established rail transport condition monitoring methods have motivated the UTCRS railway research team at UTRGV to investigate a novel solution that can address these deficiencies through wired, onboard, and vibration-based analytics. Due to the emergence of the Internet of Things (IoT), the research team has now transitioned into developing wireless modules that take advantage of the rapid data processing and wireless communication features these systems possess. This has enabled UTCRS to partner with Hum Industrial Technology, Inc. to assist them in the development of their "Boomerang" wireless condition monitoring system. Designed to revolutionize the way the railway industry monitors rolling stock assets; the product is intended to provide preemptive maintenance scheduling through the continuous monitoring of railcar wheels and bearings. Ultimately, customers can save time, money, and avoid potentially catastrophic events. The wheel condition monitoring capabilities of the Boomerang were evaluated through various laboratory experiments that mimicked rail service operating conditions. The possible optimization of the system by incorporating a filter was also investigated. To further validate the efficacy of the prototype, a pilot field test consisting of 40 modules was conducted. The exhibited agreement between the laboratory and field pilot test data as well as the detection of a faulty wheelset demonstrates the functionality of the sensor module as a railcar wheel health monitoring device.

DEDICATION

Esta tesis esta dedicada a mi familia y amigos. Quisiera agradecer especialmente a mis padres Araseli y Marco Antonio Barrera por su apoyo incondicional y por criarme con humildad. Ustedes me han enseñado que con esfuerzo, preseverancia, y dedicacion cualquier sueño se puede cumplir. Gracias por siempre empujarme a ser un buen estudiante y estar alli en las buenas y malas. Para mi hermano Manuel Alejandro, me haz ayudado a ser un mejor ejemplo a seguir para ti ya que somos de los primeros en la familia en hacer una carrera universitaria. Todo se puede en esta vida con la mentalidad correcta pero siempre hay que mantener los pies en la tierra. A mis abuelitos Lupe, Mimi, Pepe, y Calaya, los quiero demasiado. Gracias por su amor y por creer en mi en cada paso de mi carrera. A mis tios y primos, son demasiados para mencionar, pero gracias de todo corazon por brindarme su apoyo y consejos. Me siento afortunado de los momentos de conviviencia con ustedes; me hacen recordar lo bonito de la vida. Y pues como no dedicarle algo a mis amigos. Ya sea los que han estado alli desde mi infancia o los que eh sido afortunado de conocer en el transcurso de esta carrera, mil gracias por estar alli cuando mas se necesita despejar la mente de tanto trabajo con risas y anecdotas. Inclusivamente, seria insensato de mi parte si no agradeciera tambien sus consejos y apoyo; es algo que me ah servido mucho en esta carrera llamada vida. Un abrazo fuerte a todos.

ACKNOWLEDGMENTS

I want to specially thank Dr. Constantine Tarawneh for taking a chance on me years ago as an undergraduate by hiring me as a part of his research team. Thank you for believing in me and allowing me to demonstrate that I am a hard-working and dedicated student. Your mentorship has been of great influence in my collegiate career and the opportunity of working for you has allowed me to become a better engineer. Thank you for pushing not only me but many of my peers. Your strive for excellence is unmatched, and I am sure you will keep molding leaders and great engineers for years to come.

Dr. Heinrich Foltz, your support in this project cannot go unspoken. Thank you for offering your expertise at will when available. Your input paved the way in the resolution of many electrical challenges faced in this project. I wish I had taken one of your courses.

To the UTCRS team, it has been a great journey learning, laughing, and working alongside you. I greatly appreciate the support you gave me in completing this project. I know I have made life-long friendships and I sincerely hope for the best in each of your futures. Joseph Montalvo and Jonas Cuanang, I cannot thank you enough for being there even though you are fulfilling your engineering careers outside of UTCRS. Your coding expertise was instrumental in the completion of this thesis. Again, thank you.

Finally, I would like to acknowledge Hum Industrial Technology, Inc. for allowing me to be part of their innovative efforts. Brent and Byron, thank you for the opportunity. This experience will surely be one of the highlights of my early engineering career.

TABLE OF CONTENTS

Page

LIST OF TABLES

LIST OF FIGURES

CHAPTER I

INTRODUCTION & BACKGROUND

1.1 Railway Industry Impact

The railway industry serves as one of the most efficient and principal modes of bulk commodity and passenger transport in the world. It enables consumers and businesses to connect to destinations and goods in a cost-effective, safe, and reliable manner. In 2019, nearly 28% of all freight was transported via rail [1]. This highlights the dependability and productivity that has therefore empowered the industry to transcend over the years into a socio-economic pillar for various countries. One distinguishable beneficiary is the United States, which has approximately 140,000 miles of operating rail networks nationwide that employ both freight and passenger lines [1], [2]. In 2018, an article was published by the Regional Economic Studies Institute of Towson University that analyzed the economic and fiscal impact of Class 1 railroads (i.e., the largest rail network in the U.S.) in 2017 for the United States [3]. The study delineated that Class 1 railroads supported approximately 1.1 million jobs which corresponded to about $71.3 billion in wages. In addition, the total economic output was of about $219.5 billion, generating a combined state, local, and federal tax revenue of about $25.9 billion. The total job, wage, and economic output alone accounted for 0.8%, 0.9%, and 1.1% of the U.S economy for 2017, respectively [3]. As census statistics demonstrate an increase in U.S metropolitan areas, the reliance on rail transport is anticipated to continue to alleviate the probable increase in intercity traffic congestion, to meet product volume demand, and to combat fuel emission effects [4], [5].

1.2 Rolling Stock Wheels

Around 1.6 million freight rail cars operate in North America offering a variety of shipping solutions including: auto-rack cars, boxcars, gondolas, flatcars, hoppers, covered hoppers, and tanks [6], [7]. In turn, the principal element affording these rail service units their transporting capability is their wheels. Based on the estimated amount of freight cars in service, approximately 12.8 million wheels are currently in operation.

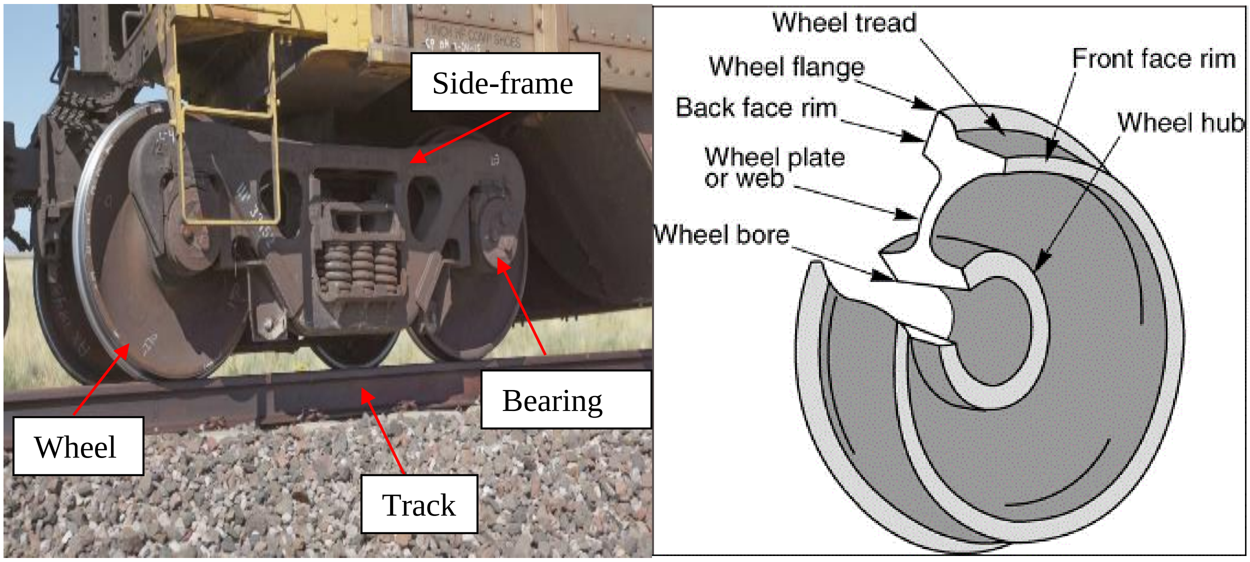

Figure 1. Railcar bogie in field operation (left) and railcar wheel diagram (right) [8], [9]

To have the robustness for continuous cargo hauls, railcar wheels are forged and hot rolled out of carbon steel. Element content percentages, material purity, and care in temperature gradient regulation are crucial as any inhomogeneity in the wheel forming procedure can lead to internal defects that can prematurely compromise the integrity of the component. After being formed, the wheel rims are heat treated and quenched to reach a specific hardness for their intended operations. Table 1 displays five common wheel classes that conform to specific carbon content and hardness. The wheels are also peened with steel shot creating beneficial residual stresses within the wheel to improve fatigue and stress cracking resistance. The final step, before going into service, includes the inspection of wheel batches by ultrasonic and magnetic particle techniques to determine whether there are any internal incongruencies with Association of American Railroads (AAR) specifications. [10]

Table 1. Common railcar wheel classes and their recommended manufacturing standards [10]

Wheel Class	**Carbon Content [%]**	**Recommended Brinell Hardness [HBW]**
Class L	0.47 Max	197-277
Class A	0.47-0.57	255-321
Class B	0.57-0.67	302-341
Class C	0.67-0.77	321-363
Class D	0.67-0.77	341-415

Once in operation, however, wheelsets become prone to defect propagation associated with wheel-rail induced wear [11], [12]. Their exposure to diverse operating conditions such as train velocity, railcar load, track profile, climates, and even manufacturing flaws can further augment their susceptibility to degradation. Wheel deterioration manifests in three main forms. One involves those defects that are visually evident. Some examples of these defects, as seen in Figure 2, include wheel flats, spalls, shelling, and thermal cracks.

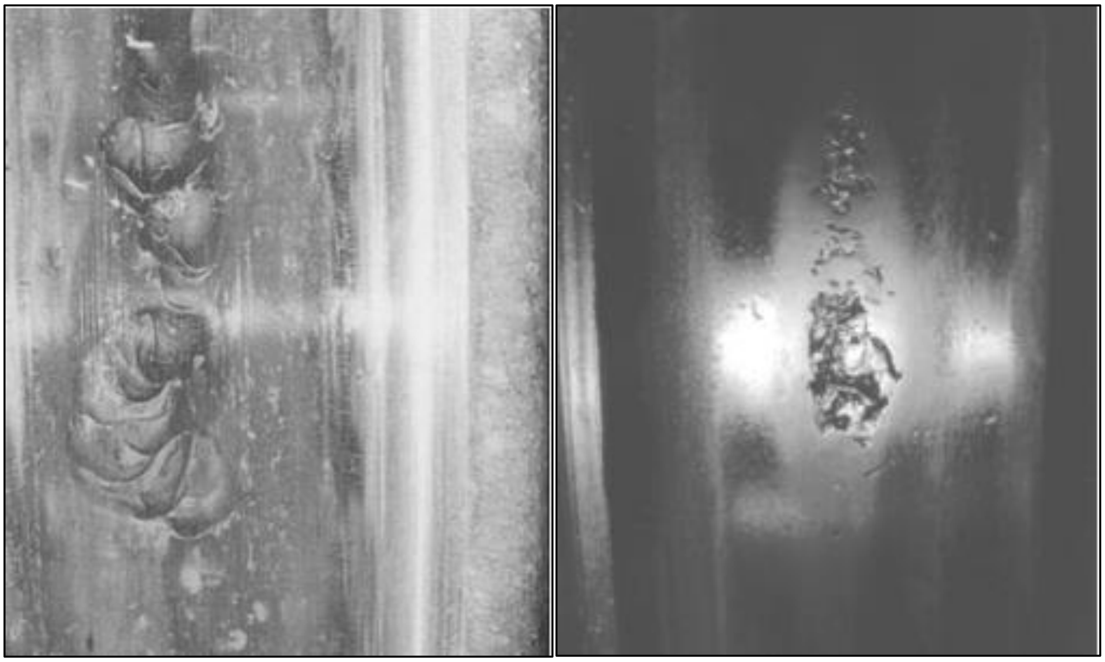

Figure 2. Wheel skid flat (left) and wheel shelling originating from skid flat (right) [13], [14]

The second type of defects, although recognizable by a trained eye, are those that require geometric validation of the external profile of the wheel with gauges to determine the presence of a fault. As depicted in Figure 3, examples of these defects include thin flanges, worn roots, hollow flanges, and deep flanges. The last defect classification is reserved for subsurface flaws which require techniques such as ultrasonic inspection to be detected . These defects include subsurface porosity and internal cracking which can lead to more catastrophic faults such as vertically split rims (VSR) or shattered rims (SR) [13],[15].

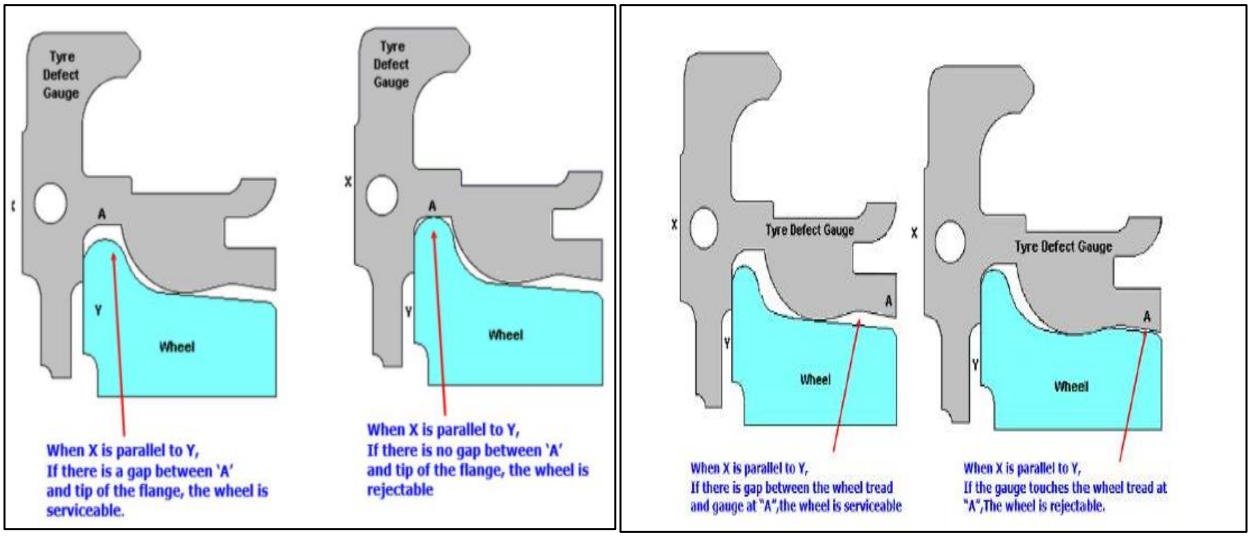

Figure 3. Deep flange (left) and hollow tread (right) [16]

In 2000, Nielsen and Johansson [17] conducted a preliminary study that adopted root causes for common wheel irregularities, setting the framework for understanding defect initiation mechanisms. Since then, continued wheel defect studies have enabled the creation of wheel defect practice codes that elaborately classify wheel defects and their causes. Table 2 categorizes condemnable wheel defects and their origin.

Table 2. Wheel defects and their leading causes [13]

Defect Type	Defect Cause
Thermal Cracks, Shelling, and Tread Checks	Surface Rolling Contact/Thermal Fatigue
Spalling, Wheel Flats, Scaled Wheels	Sliding Heat Generation
Flange Defects, Hollow Treads, Rolled Edges	Wear, Flow, and Improper Steering of Bogies
Cracked or Broken Web/Plates, Wheel Rims, Flanges, and Shattered Rims	Subsurface Originating Fatigue
Dented Flanges, Wheel Distortion, Out of Round Wheels	Impacts
Overheated Wheels, Wheel Flats, and Misaligned Break Gears	Braking

Overall, the described wheel defects can be significantly detrimental as they can affect the wheel-rail interaction causing high impact forces on the rail as the railcar navigates on the track, inflicting damage to the rail network, the cargo, and the rail vehicle's suspension system [11], [12], [18], [19]. This raises safety concerns for railway transport while also creating potentially superfluous expenditures due to delays, derailments, and increased maintenance costs. According to a 2006 article by Progressive Railroading, it can cost about \$25,000 to \$250,000 an hour for a railroad to clean up a derailment [20]. In the past decade, specifically from January 2010 to July 2021, the American railway industry has faced over 23,000 train accidents resulting in approximately 14,000 derailments and an overall financial toll of approximately \$3.4 billion [21]. Of these accidents, both wheel and track related mishaps have accounted for roughly 29% of accident occurrences equivalent to about 40.9% in damage affiliated expenditures (i.e., approximately \$1.4 billion in total costs) [21].

1.3 Maintenance Practices

The wide array of liabilities that wheel defects can impose demand for the implementation of appropriate countermeasures. Therefore, maintenance guidelines have been established by lead agencies governing the industry such as the Federal Railroad Administration

(FRA) and the Association for American Railroads (AAR). Table 3 displays a set of recommended practices for certain impact force signatures. As stated in Section 1.2, a notable characteristic of a defective wheel is the high impact forces that it inflicts on the track. Under current guidelines, 290 kN (65 kip) triggers a window for repair while 623 kN (140 kip) or more indicates a mandatory halt in operation [22]. However, the recurrence and gravity of these events promote that the industry should proclaim more proactive practices. Therefore, a study made by FRA suggests adjusting the established thresholds as presented in Table 4 [23]. If these amendments were to be enforced, 270 kN (60 kip) would signal the initial maintenance advisory and any wheel emitting 534 kN (120 kip) or more requires immediate inspection and removal from service.

Table 3. Contemporary WILD guidelines for freight services [22]

Impact Force [kip]	**Impact Force [kN]**	**Contemporary Recommended Practices**
65-79	290-351	Owner can choose to shop car for repair
80-89	356-396	If car is shopped for non-wheel repairs, then repair facility is allowed to conduct wheel related repairs as well
90-139	400-618	Operating railroad is required to shop car upon arrival to destination
140+	623+	Operating railroad is required to inspect train and move it at speeds under 48 km/h (30 mph) to set out affected car

Table 4. FRA suggested WILD guideline amendments [23]

Impact Force [kip]	**Impact Force [kN]**	**New Recommended Practices**
60	270	Issue maintenance advisory for affected car
70	311	Change wheel at the car’s next visit to repair shop
80	356	Condemn the wheel and replace at 1st opportunity
120+	534+	Stop train immediately for inspection and remove car from service at 1st opportunity

When the wheels are removed, reprofiling procedures can be conducted to salvage the wheel for continued use. For this to occur, the wheel profile attributes must still be within tolerances. Contrarily, if the wheel profile already exhibits excessive wear, the wheel is declared condemnable and the wheel is scrapped. To gauge condemnable wear, another standard targets the size of the defect rather than the effects it may radiate. A summary of these regulations can be found in Table 5. Any wheel displaying geometric characteristics that meet or exceed these limits are subject to interchange. An article published in April 2012 by Progressive Railroading recapped the events of TTCI's 17th annual AAR research review. One of the main topics of interest was renewal costs. According to Scott Cummings, TTCI's principal investigator at the time, an estimated 582,000 wheelset replacements are performed annually, equaling to roughly $828 million per year. On his behalf, this expenditure accounts for more than half of all repair costs [24].

Table 5. Wheel defect geometric limits [25]

Defect Type or Area	Wear Limit
Flat spots	2½ in. or more in length
Gouges or chips in flange	1½ in. in length and ½ in width
Shelled-out spots	2½ in. or more in length
Hollow worn treads	5/16 in. or more in depth
Flanges	1½ in. or more in height
Rims	Less than 1 in. in thickness

Most of these repairs are prompted by traditional wheel inspection techniques such as drive-by visual inspections and wheel profile measuring by trained personnel. But even if conducted by an experienced individual, these approaches lack accuracy and efficiency. For this reason, condition-based maintenance is a crucial asset for the railway industry as they signal maintenance based on the relayed wheelset condition data from either onboard or wayside health monitoring sensors. For wheels, the most prevalent condition monitoring hardware is known as the Wheel Impact Load Detector (WILD) which can be seen in Figure 4. These wayside detecting systems were first implemented in the early 1980s as a project funded by Amtrak and the Federal Railroad Administration (FRA) to detect defective wheels in the Northeast Corridor (NEC) of the U.S. rail system for the prevention of potential rail system and railcar suspension damage [22]. Using strategically track-mounted strain gauge sensors, WILDs monitor and detect the dynamic load behavior of passing railcar wheels by measuring the wheel to rail contact force. Wheels exceeding the predefined high impact load thresholds seen in are flagged for corrective/preventive maintenance.

This wheel monitoring method, however, is limited by the strategic placement of these sensors along the track. Progression of a pre-existing defect or the propagation of a new anomaly within the wheel profile will not be monitored nor detected until the next WILD location. Unfortunately, because continuous monitoring of the wheels is unachievable, a wheel can unexpectedly fail between WILD sites without warning. According to an implementation guide for wayside monitoring systems issued by the FRA in 2019, only about 185 WILD systems were operational nationwide as of 2017 [22].

Figure 4. Wheel impact load detector (WILD) [22]

Concerns with the reliability and accuracy of the system also arise. If the system is not operated within the specifications of the manufacturer, the accuracy and reliability of the WILD can be affected. Although varying from manufacturer to manufacturer, some of the most critical requirements to achieve optimal performance from these detectors include site size, incoming rail vehicle speed, peak wheel impact load, and the number of integrated WILD systems that can verify the readings of other WILDs. For example, a WILD system by Mermec^{TM} requires a site size of about 11 m (35 ft) and a minimum incoming railcar speed of 40 km/h (25 mph). A WILD system by L.B. Foster^{TM} requires a site size of about 15 m (50 ft) and a minimum passing railcar speed of 48 km/h (30 mph). As seen in Table 3, peak impacts of at least 290 kN (65 kip) are required to hold the railcar owner responsible for the affected rail unit for all AAR regulated railroads. There are currently no WILD data regulations for impact forces that progressively reach this limit.

Other traditional wheel monitoring systems include wheel profile measuring systems or WPMS. These wayside systems utilize laser-based scanning and high-speed digital cameras to detect worn wheel features which include high and thin flanges, thin rims, and hollow treads. But like WILDs, they are also limited by their absence along the rail track. As of March 15, 2017, only 15 WPMS were in operation nationwide [22]. An example of these systems is demonstrated in Figure 5.

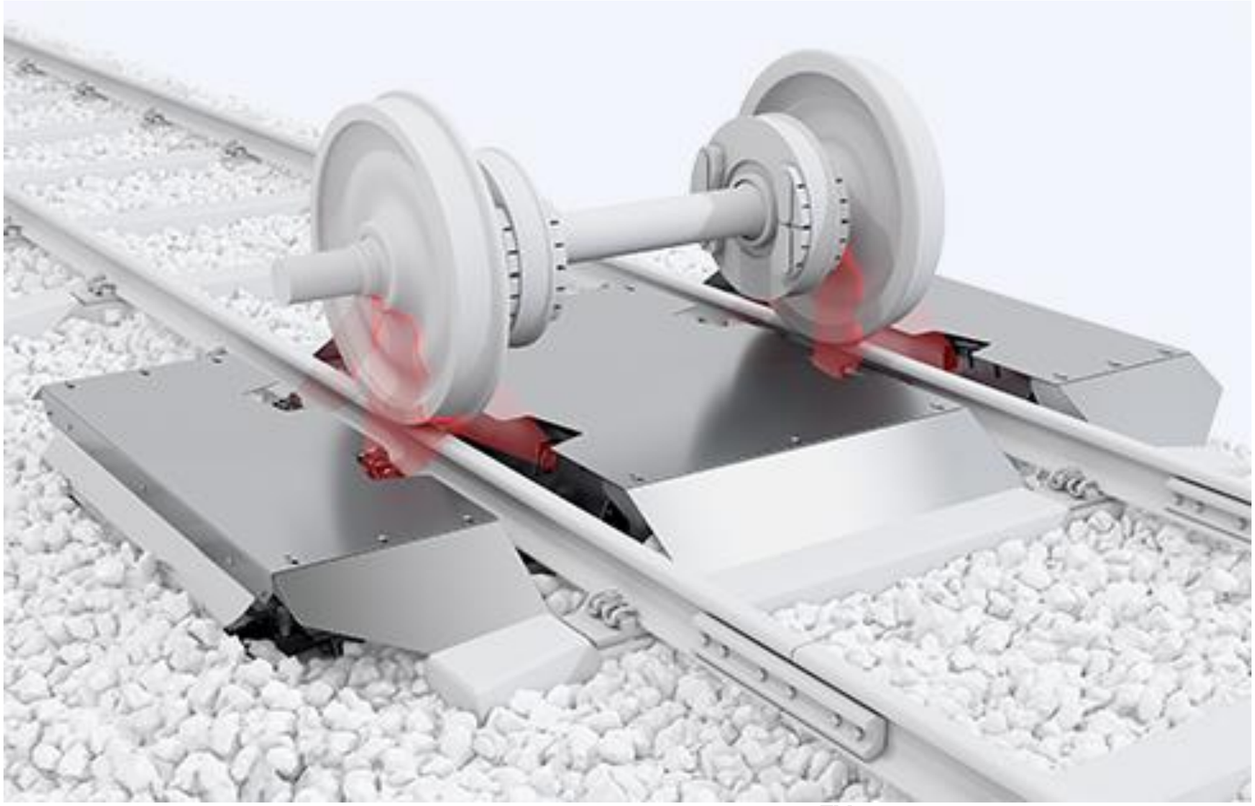

Figure 5. Wheel profile measuring system (WPMS) by Mermec^{TM} [26]

Even though WILD and WPMS systems have been used for decades to warn rail service operators of potential failures, they also possess the inherent characteristic of misdiagnosing components. The uncertainty of an imminent threat and lack of continuous condition feedback provokes urgency for a superior wheel health monitoring device.

1.4 Derailment Case Studies

The following two case studies were selected from detailed investigation reports by the Transportation Safety Board of Canada. The presented cases portray two derailment episodes where defective wheels were found to be the primary culprit of the accidents. These synopses highlight the gravity of such events and the poor judgement of current early detection measures.

1.4.1 Railway Investigation Report R14M0002 [27]

On January 7, 2014, Canadian National Railway Company (CN) freight train M30831-06 was travelling around 47 mph when 19 railcars and one distributed power locomotive derailed near Plaster Rock, New Brunswick. The derailed cars were transporting about 230,000 L of hydrocarbons including butane and crude oil. Ethanol and acid residue were also being transported. The accident caused the tanks to spill their cargo which triggered a fire that led to the evacuation of 150 residents within a 1.6 km radius of the area -- no injuries were reported. A diagram of the accident is shown in Figure 6. The investigation delineated that the primordial cause of the incident was a shattered rim (SR) from wheel L3 of railcar CRDX 15109. The fracture had originated from a fatigue crack triggered by subsurface porosity in the wheel tread. As seen in Figure 7, the crack propagated until reaching the wheel hub. After the crack caused part of the wheel tread to fall, wheel L3 then shifted from its axle seat inboard towards its mate (R3). In the process, derailment of CRDX 15109 inflicted repeated wheel impacts on the track causing the rail infrastructure to fail as well. About 350 feet of track were destroyed, creating a gap in the rail system which derailed the other 18 railcars.

Figure 6. Diagram of freight train M30831-06 derailment [27]

According to the investigators, CRDX 15109 had passed a WILD on January 6, 2014 (i.e., the day before the accident) under fully loaded conditions and no abnormality was reported. Previous inspections of the wheel profile had also been compliant with Class C AAR wheel standards. As the root cause of the SR was due to subsurface porosity, the report stated that ultrasonic testing (UT) had been performed when the wheel was manufactured in 1991, but the defective zone had gone undetected. In 2006, the wheel was removed from service for reprofiling, and another UT was conducted. The post-derailment metallurgical analysis of the component denoted that the porous region was about 3.2 mm (1/8 in) long and should have technically been detected. However, at the time, data logging of UT results was not a requirement.

Figure 7. Cracked wheel L3 of railcar CRDX 15109 [27]

1.4.2 Railway Investigation Report R18W0007 [15]

On January 6, 2018, Canadian National Railway Company (CN) freight train M31731-04 presented a train-initiated emergency brake stop in Rennie, Manitoba. After an inspection down the rail line was conducted by the operators, it was determined that 23 railcars had derailed. Out of these 23 railcars, 8 contained hazardous cargo including: liquid hydrocarbons, petroleum distillates, corrosive liquids, liquefied petroleum gas residue, and nickel sulfides -- no spills to the environment or injuries were reported.

Figure 8. Derailed railcar ATW400515 [15]

A vertically split rim (VSR) on wheel R4 of railcar ATW400515 was pronounced the cause of the derailment. Wheel R4 had broken off its wheel seat and translated inboard towards L4. As presented in Figure 9, post-derailment examination of the wheel concluded that the wheel failure began with three interconnecting wheel pieces of 15.2 cm, 33.0 cm, and 35.6 cm (6 in, 13 in, and 14 in) in length. Closer inspection of the components revealed oxidation within the adjoining borders of the 33.0 cm and 35.6 cm (13 in and 14 in) pieces, meaning that defects were present well before the failure occurred. The 15.2 cm (6 in) piece was never recovered, but the investigators hypothesize that this is where the fracture initiated.

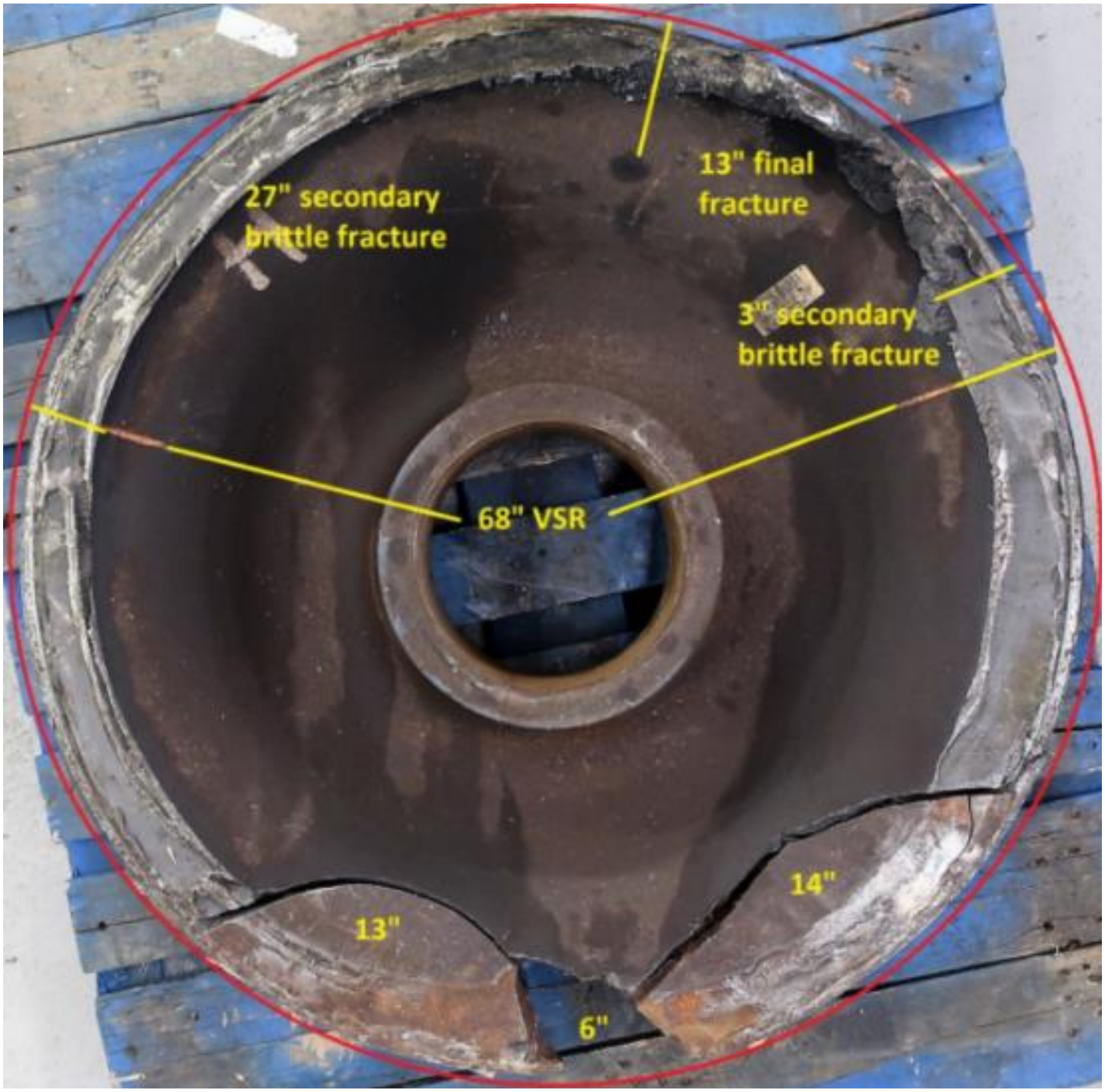

Figure 9. Failed wheel R4 of railcar ATW400515 [15]

Interestingly, the affected railcar wheel had passed 18 times through a WILD in the lapse of a month from December 6, 2017, to January 6, 2018 (i.e., the day of the failure). At an unloaded state, no wheel impacts exceeded 356 kN (80 kip) until four days before the accident (January 2, 2018) when the unit was loaded. Two days prior to the derailment, five WILD impact recordings demonstrated wheel impacts over 400 kN (90 kip). In AAR standards, these impact force readings are condemnable [22], yet CN standards dictate that anything between 400 and 623 kN (90-140 kip) is grounds for an opportunistic repair at the next Certified Car Inspection (CCI) port. Thus, the railcar remained in service and about 4½ hours later after emitting a peak impact of 485 kN (109 kip), the wheel catastrophically failed. Nevertheless, even by following AAR rules, the car would have traveled unmonitored until the next repair shop. Without knowledge of a worsening wheel condition, the car might have registered an impact worthy of an immediate halt in service. More suitable measures could have been taken with improved equipment and guidelines.

1.5 Transitioning Toward an Onboard Wheel Health Monitoring Device

The aforementioned incidents exemplify the limitations in present maintenance methods. With the current technological innovations, the introduction of a pioneering technology that can address these deficiencies to enable constant, reliable, and precise onboard component health monitoring is highly feasible. Over the past decade, the absence of continuous and effective monitoring solutions in the rail industry have motivated the University Transportation Center for Railway Safety (UTCRS) at the University of Texas Rio Grande Valley (UTRGV) to conduct research regarding the development of a vibration-based onboard health monitoring device for railcar bearings. Years of study have materialized into promising wired modules that can provide accurate and timely bearing health diagnostics that can characterize the condition of tapered-roller bearings and identify defects smaller than 6.45 cm^2 (1 in^2) [28]. Furthermore, current research practices at UTCRS have evolved into wirelessly transmitted bearing analytics via wireless modules and energy-harvesting devices that can support these systems using rail operation conditions [29], [30]. The significance of this work has recently captivated the attention of Hum Industrial Technology, Inc. (HUM), a private rail industry company that has patented the technology and developed an onboard monitoring system known as the Boomerang. The device can transmit real-time bearing condition metrics, enabling immediate prognostic feedback to railcar owners and operators. HUM entrusted UTCRS with the task of evaluating the sensor to optimize it for industrial integration. Comprehensive laboratory and field assessments were conducted that established the bearing monitoring efficacy of the system. However, because the module was still in its development stage, a margin of opportunity was available to evaluate any additional abilities the device might possess. Therefore, a concurrent investigation was enacted to investigate whether the module was also capable of detecting high wheel impacts with its instrumented accelerometers.

This thesis will present the work conducted to determine the wheel condition monitoring capabilities of the Boomerang. Chapter II provides a literary review on studies that have been conducted to propose novel wheel monitoring solutions or enhance current methods. Chapter III describes the equipment and methodologies used to arrive at a laboratory and field evaluation of the sensor. Chapter IV shows the laboratory response of the device under different scenarios the device might encounter in the field. In Chapter V, supplemental testing results are presented that can provide insight towards the optimization of the module in a foreseeable future. Field assessment results are discussed in Chapter VI and Chapter VII will focus on the encountered limitations, conclusive remarks, and proposed future work.

CHAPTER II

LITERARY REVIEW

The potential benefits the railway industry could reap with the development of a reliable wheel condition monitoring system make the subject a recurrent field of study. Certain research practices focus on developing novel wheel condition monitoring alternatives while others have tried to enhance established methods such as wheel impact load detectors (WILDs) or wheel profile measuring systems (WPMS). The following literature review exhibits a selection of these visionary wheel monitoring concepts.

2.1 WILD Enhancement Attempt [31]

As mentioned in Section 1.3, WILD systems are the dominant wheel monitoring method in the rail industry, but they lack reliability and rail line ubiquity. Nevertheless, a study made by Stratman, Liu, and Mahadevan in 2007 tried augmenting the potential of the WILD system by assessing the inefficiency of visual inspection, premature wheel removal, and the absence of WILD data standards regarding impact force progression into levels of concern. The strategy involved constructing two quantitative railcar wheel removal criterions by exploiting high impact and failed wheelset data collected from WILD systems.

The first criterion (C1) dealt with high impact data for wheels that exhibited condemnable 400 kN (90 kip) loads along with rapid increases in dynamic impact over time. Three consecutive impact readings with an increase of 67 kN (15 kip) or more between each reading needed to occur within a 50-day lapse or less with a peak dynamic impact of at least 311 kN (70 kip). By referencing a wheel failure database from a major North American railroad, they determined that at least 10.53% of the failing modes had this successive impact reading increase. This meant that if C1 were to be implemented along the time frame these failures occurred, then 10.53% of those failures could have been prevented. Furthermore, the data also revealed that approximately 200 wheels operated under this criterion per year in North America. A deeper analysis of this data for previous years revealed that the criterion could have detected 78.2% of affected wheels before traditional methods. This meant 156 damaged wheels were left in service causing additional rail infrastructure damage. Moreover, the wheelsets would have been removed, on average, 31.7 days prior to the day of failure. Thus, 31.7 days of additional rail unit and line potential damage could have been prevented. Figure 10 displays a wheel operating under this criterion.

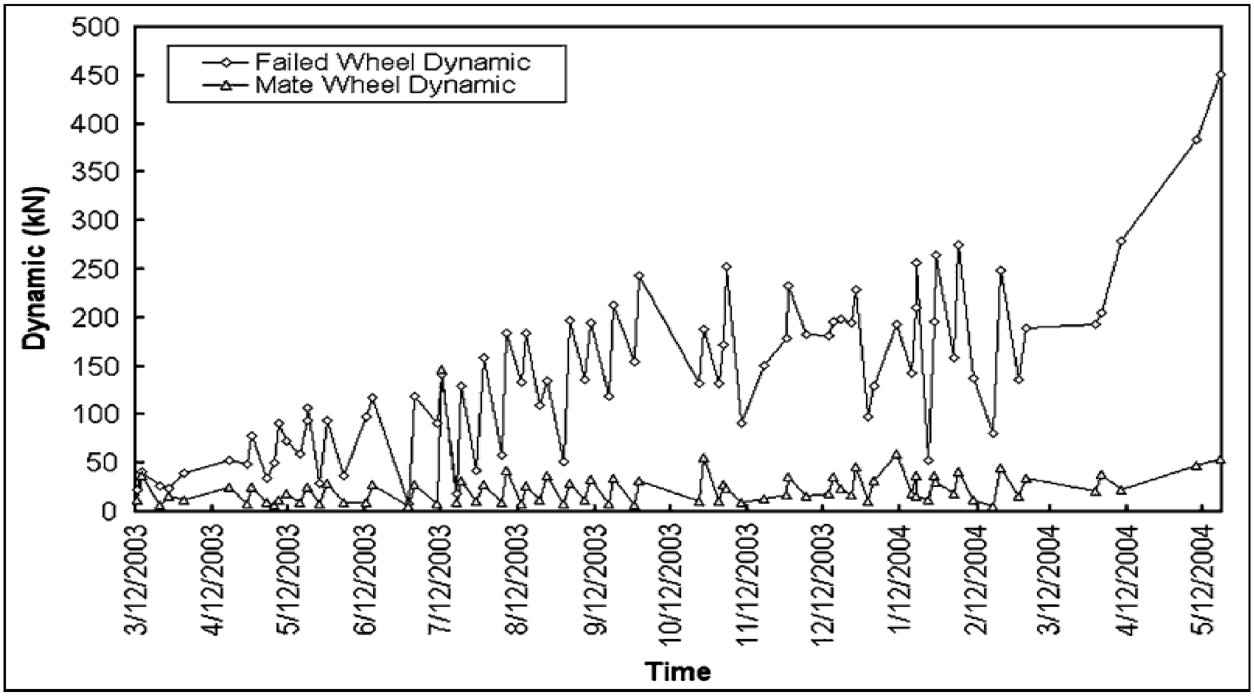

Figure 10. First criterion example (rapid increase in impact readings) [31]

The second criterion (C2) was developed with respect to normal impact reading wheels with a sudden increase in impact over a short period of time. Under this wheel removal strategy, the wheel needed to have a dynamic impact of at least 177.9 kN (40 kip) with three consecutive and incrementing impact readings of 8.9 kN (2 kip) or more between readings with an average increase of at least 44.5 kN (10 kip) between the three readings. This behavior needed to occur within a 20-day time frame. Furthermore, no impact reading 30 days prior to the initial impact deviation reading could be greater than 22.2 kN (5 kip) or less than 67 kN (15 kip) of the initial impact deviation value. Like the wheel failure database analysis of the first criterion, about 5.26% of the failures followed this trend. This indicated that implementation of this wheel removal methodology could have been prevented 5.26% of the failures. The data also illustrated that annually about 1400 wheels in North America follow this criterion. Based on previous year data, 47.5% of those wheels could have been detected early. Thus, 665 damaged wheels were left in service risking property and safety. Further analysis of the data in this database demonstrated that the wheels could have been removed about 66.6 days earlier, preventing unnecessary detriment along that time frame. Figure 11 demonstrates an example of a wheel displaying this behavior.

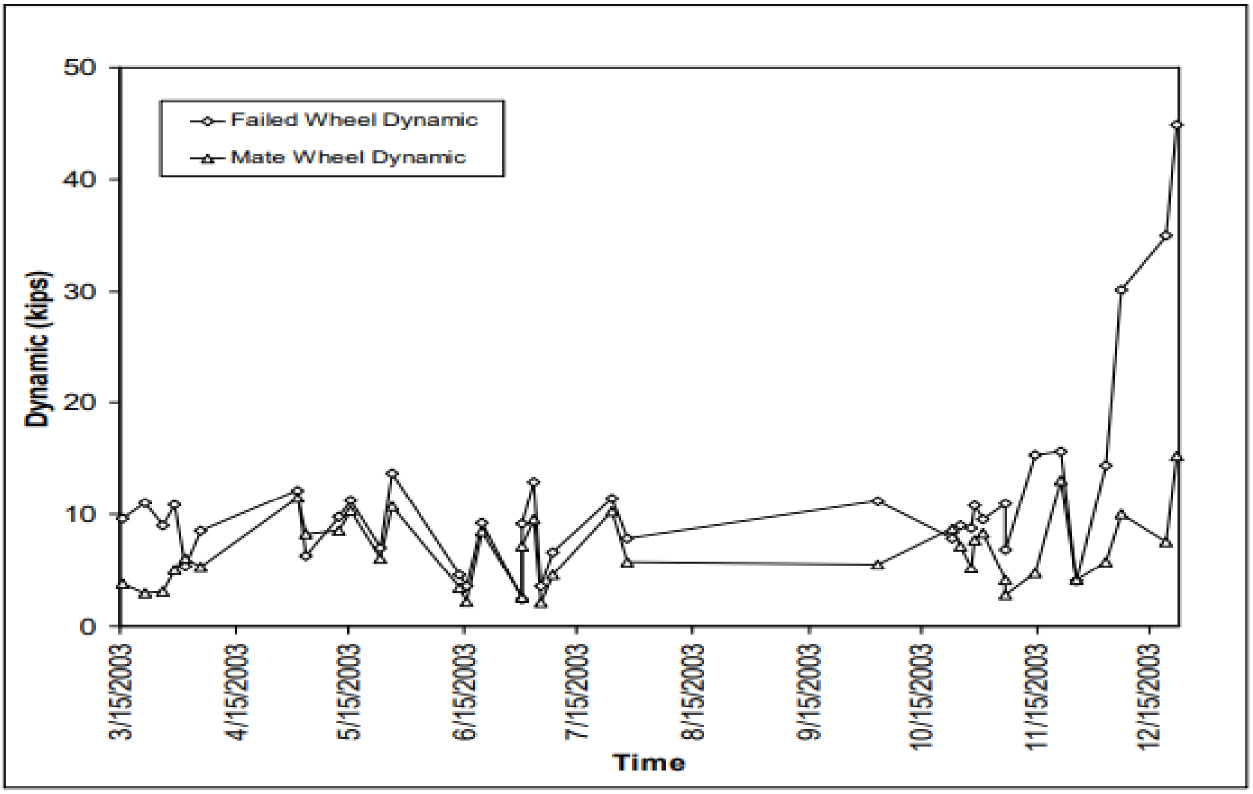

Figure 11. Second criterion example (sudden increase in impact reading) [31]

Application of the two criteria would significantly benefit railcar owners as 15.9% of wheel failures, on average, could have been prevented. Yet, although instrumental in further enhancing WILD inspection, the basis of this analysis is hindered by its reliance on the WILD itself. The sparsity of these sites inhibits continuous monitoring; therefore, wheel failure can still occur without warning. Nonetheless, the latter information can serve as the foundation for future wheel monitoring approaches that can employ machine-learning.

2.2 Investigated Alternatives

As established wheel methods pose significant deficiencies, researchers around the world continuously investigate novel methodologies for the detection of wheel defects in rolling stock. These solutions involve both wayside and onboard technologies. Their functionalities are devised from various techniques such as: vibrations, acoustics, ultrasonics, laser and high-speed camera, and fiber-optics, among others.

2.2.1 Vibration-Based Alternatives

Vibration-based methods take advantage of the mechanical perturbations produced by operating components to signal faults within the system. Generally, a non-normative increase in a vibration signature suggests the presence of component degradation [28]. Koenig et. al [32] published an article to address baggage cart-wheel failure in airports with the use of a vibration-based condition monitoring system. Although not intended for use in the railway industry, similar wheel-track dynamics were involved as in rail service. To evaluate the system and establish bad and good wheel thresholds, a pilot test was deployed in which vibration sensors were placed on each side of a baggage cart track to record baggage-cart wheel vibrations. As seen in Figure 12, photo sensors were also used to identify the passing cart by reading a binary code on the unit, facilitating data analysis by matching the cart to the data. The baggage-cart wheel data was collected and sent to a server for analysis for six months. The results revealed an increase in vibrations with increased age and use of the baggage-cart wheels establishing the method as a viable predictive model for condition-based maintenance. The study highlighted the capability of vibration-based usage for condition monitoring, yet an airport track system is less complex and environmentally exposed than the rail network. Accelerometers can be spaced out accordingly without conjuring prolonged interludes in data acquisition and the sensors can be protected with minimum efforts. In the rail industry, however, aside from having to construct ruggedized sensors for field installation, spacing out accelerometers for continuous monitoring could prove expensive and impractical.

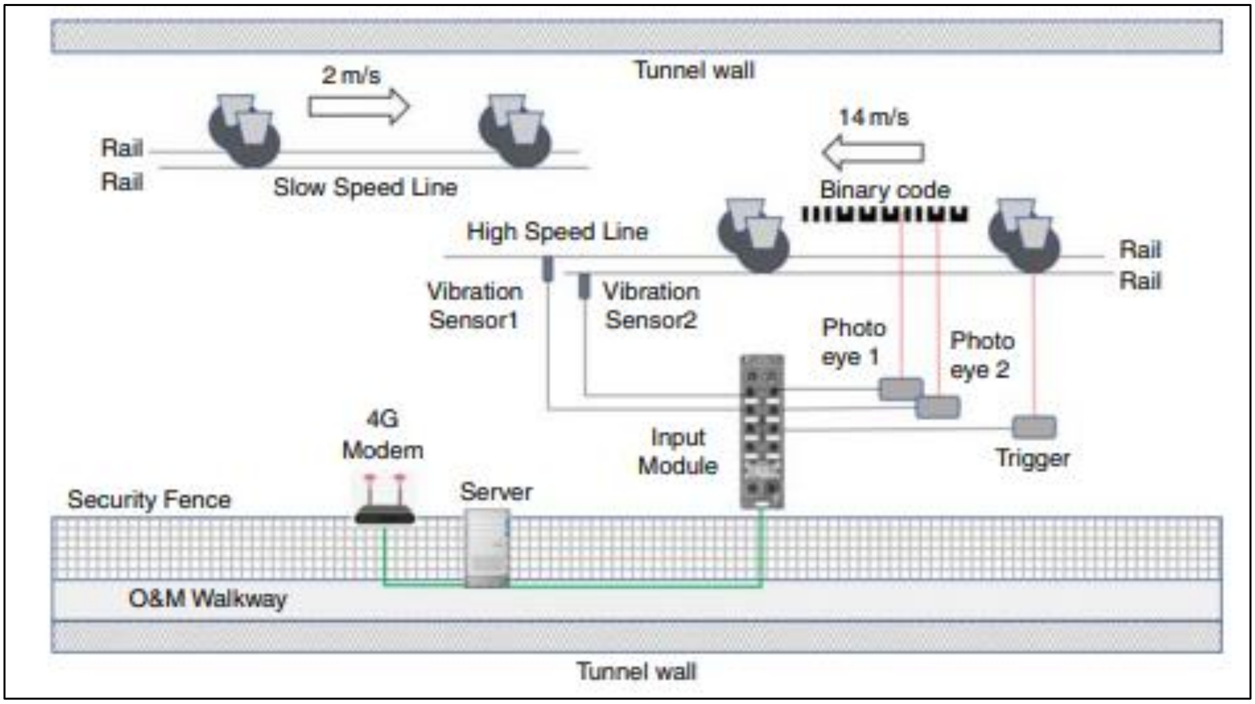

Figure 12. Koenig et. al. experimental setup [32]

Like Koenig, Barman and Hazarika [33] proposed a vibration-based wayside alternative but for the possible condition monitoring of trains of the Northeast Frontier Railway sector in India. An accelerometer, ADXL335, was placed on a rail joint fish plate to obtain dynamic railcar conditions to monitor five trains that operated at different speeds. Their respective vibration signals were collected and then analyzed in both time and frequency domains. While the authors claimed the time and frequency domain provided predictive conditions of different railcar components such as wheels, health monitoring could only be executed at the location where the accelerometer was placed. Data transfer and storage also required direct cable connections from the accelerometer to a laptop. The methodology resembles the mechanics of a WILD detector, meaning continuous monitoring is unachievable. For continuous asset monitoring to occur, the rail network must be instrumented by accelerometers at each stretch. Furthermore, the environment can rapidly jeopardize the integrity of the unprotected equipment. Without the introduction of an improved manner of data acquisition, the approach is unfeasible.

Another recent vibration-based method was presented by Sun et. al. [34] in a study that targeted polygonal wear of railway wheels (PWRW) in high-speed rails. A “sensor-less” fault detection framework was proposed where vertical axle-box vibration acceleration data would be used to detect the polygonal faults by employing an angle domain synchronous averaging technique (ADSAT). Models were constructed based on both simulations and field data, revealing that the method had better PWRW detection capabilities than traditional methods (i.e., those employing discrete time Fourier transforms). Noise suppression was also achieved under ideal conditions (i.e., simulations). However, the time to obtain and examine axle-box data from each railcar was not disclosed, making the real-time prognosis capability of the framework unknown. Furthermore, the fault detection algorithm has only been studied on PWRWs; detection of other defects was not discussed. Cancellation of noise from the field data also proved to be challenging due to the uncertainties in the operating environment.

2.2.2 Acoustic-Based Alternatives

The acoustic emissions from working components have also been used to signal non-normative operations. In 2010, Anastasopoulos et. al. [35] studied whether rail mounted acoustic emission (AE) sensors could detect faults on an on-line dynamic railcar to avoid the accessibility issues presented from traditional methods that relied on immobile railcars or off-track inspection. Extensive acoustic emission testing was conducted on both trams and trains with healthy and defective wheel conditions. Digital signal processing of hit-driven data (HDD) determined that at lower speeds, the AE sensors presented better resolution in terms of wheel defect detection than at higher speeds. For the tram data analysis, long waveform signals (WFS) were mainly used. Wheel flat detection was linked to voltage spikes and root mean square calculations of the data in the time-domain demonstrated that the time difference between axles could be monitored, allowing for the possible macroscopic observation of the signal levels that could lead to the detection of periodic (wheel flats) or continuous (bearing) noise. To put the findings into practice, a third field experiment was performed using a locomotive with one healthy and one defective wagon. The defective wagon contained artificial 2.5 cm (0.98 in) and 5 cm (1.97 in) wide flats running horizontally across the wheel rim surface. The results supported the theory of the tram-data analysis, as the defective car depicted periodic spikes in the average signal level versus time graphs, whereas the reference car displayed a smooth signal output. The results also demonstrated that the 5 cm (1.97 in) defect had higher signal amplitudes than the 2.5 cm (0.98 in) defect which highlights that the method could possibly gauge the severity of the wheel condition. However, because the AE sensors relied on wayside mounting and direct cable connections for data acquisition, the methodology was deemed unfit for continuous health monitoring. Complex digital signal processing is also required which further delays the relay of wheel health diagnostics. Another major drawback of this approach is its inability to detect the exact wheel in distress. The AE sensors can distinguish a healthy wheel from a defective one, yet they can only determine that a wheel on a railcar travelling along the instrumented track segment is defective but not the specific wheel in question.

A 2019 study by Bondarenko et. al. [36] also focused on wheel condition monitoring using the acoustic emissions of dynamic railcars. A field test was conducted using professional sound recording equipment coupled with an international standard that specified the conditions for obtaining reproducible acoustic emissions of railway transport units. The field measurements focused on five distinct sounds including: (1) rolling noise of wheels, (2) the wheel-rail impact interaction, (3) curve screeches, (4) brake-block and wheel interaction, and (5) the air release from the air brake control valves. After acquiring the data and conducting preliminary signal processing, spectrograms were used to illustrate the characteristic response for each acoustic signal of interest. Hilbert transforms were then used to construct envelopes of the acoustic signals to theoretically represent the field data. Using the field and theoretically obtained acoustic data, a microcontroller device, as seen in Figure 13, was devised and tested. The experiment entailed playing a videorecording of a moving train with a wheel flat on a smart phone.

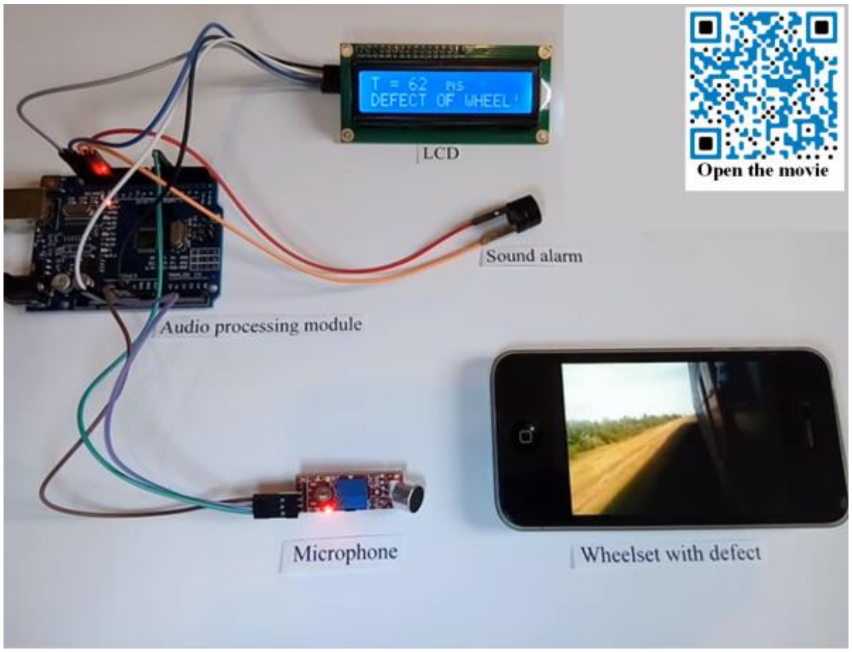

Figure 13. Acoustic-based microcontroller for wheel monitoring [36]

The controller successfully detected the wheel flat, demonstrating a slight improvement to Anastasopoulos' method as the proposed system could promptly communicate the presence of a wheel flat on the railcar. Unfortunately, it is unknown whether added noise can affect the functionality of the device. That is, when the researchers were obtaining the field data, ideal environment conditions were required as various elements could disrupt the results. Sound reflecting objects such as hills, bridges, or houses in the vicinity of the recording unit could disturb the noise field. Even wind speeds could not be greater than 5 m/s (16 ft/s) as they could affect data acquisition. In addition, like Anastasopoulos' method, although the device can detect wheel flats, the microcontroller cannot pinpoint which wheel contains the defect. This is an issue as additional resources must be allocated to identify the location of the defect for maintenance.

2.2.3 Ultrasonic-Based Alternatives

In ultrasonic-based methods, high frequency ultrasonic pulses of short wavelengths are introduced onto objects. Deviations in the incident waves or varied attenuations in the introduced pulses indicate the possible existence of surface or subsurface defects. This method has been the preferred non-destructive testing (NDT) method by the AAR in manufacturing and maintenance procedures of wheelsets, yet researchers have also tried developing solutions based on this technique. In 2008, Pau and Lebon [37] conducted a series of ultrasonic testing (UT) experiments to see to what extent wheel wear could affect wheel-rail contact and associated pressure distributions. At the time, the technique could be adopted to optimize established methods. A realistic wheel-rail system was used to conduct the tests where the regular flanged wheels would be abraded to resemble different degrees of tread wear (0.1-0.5 mm). The contact regions were mapped out with the use of a 15 MHz immersion probe partially submerged in water with the wheel. Different levels of wear were captured by using coefficient of reflection to graphically map contact, but UT data conversion into contact pressure was not immediate as various parameters needed to be assessed such as: surface roughness, incident wave frequency, and material type. A calibration procedure was needed to create the contact pressure matrix from the coefficients of reflection of the wheel tread interface. Nevertheless, counter formal (no wear exposure) to conformal (wear-exposed) transition was successfully obtained, leading to the knowledge that the abrasion procedure led to the decrease in 36% of the contact pressure. Yet, the researchers disclosed that the experimental setup was not feasible in field conditions, but with the advancements in technology the next studies would focus on the development of a prototype that could monitor rail traffic.

In 2018, Cavuto et. al. [38] expanded on the use of ultrasonics for wheelset flaw detection with laser ultrasonic testing (LUT). The study investigated whether common fatigue cracks in wheelsets could be detected without dismounting them from the railcar. The ultrasonic method used an air coupled ultrasonic probe that could detect the high energy emission of the pulsed laser. The unneeded contact from both the measurement and excitation devices promoted rapid testing. To conduct the study, wheelsets with fatigue cracks located in frequently manifested areas (i.e., axle and region between axle and wheel) were tested. A dismounted railcar wheelset was set onto a special fixture that harnessed the LUT system and allowed the rotation of the axle for full circumferential scanning by the laser. The results proved the ability of the LUT in detecting the cracks, but the study only proved that using the special laboratory setting. Field tests are needed to further validate its efficacy, yet, even if effective in the field, continuous wheel monitoring is improbable. The equipment setup needed to achieve the results is too bulky and suited for testing only one wheel at a time. Additional research is required to develop a more compact fixture that allows multiple wheels to be diagnosed wirelessly and continually.

2.2.4 Laser and High-Speed Camera-Based Alternatives

Laser and High-Speed Camera Techniques, such as the established Wheel Profile Measurement Systems, have also been subject to research. A thermal imaging study was conducted by Yamamoto [39] to investigate wheel-rail contact points as they are key contributor to vehicle dynamic characteristics. The experiment involved placing a thermal imaging camera on the truck frame close to the rail head. The test results confirmed that the contact points could be accurately identified under suitable thermographic conditions and that, in case of a derailment, the flange and gauge locations could be accurately detected. Yet, an adequate environment, finding a cost-efficient thermal imaging system, and vast computational power for image processing prevent this solution from becoming adopted as a continuous wheel health monitoring solution. This rationale can be extended onto other laser and high-speed camera-based solutions. Achieving continuous and qualitative surveillance of wheel-rail is highly unfeasible. The act can be achieved at strategic locations in a rail network, but to constantly monitor wheel-rail behavior would involve high-end imaging systems on each wheel of a railcar fleet. The heavy reliance on computing power and cooperating environment conditions excludes the approach from being a continuous monitoring contender.

2.2.5 Fiber-Optic-Based Alternatives

Attempts at using fiber optics as viable wheel monitoring alternatives have also been explored. Fiber optics are dielectric and passive meaning they need no electrical power [40]. They have low loss and their wide use in telecommunications allows them to be readily available and inexpensive. They are also immune to electromagnetic interference which can alter signals.

Anderson [40] presented a multimode fiber sensor for wheel flat detection in the Joint Rail Conference proceedings of 2006. His investigation revolved on using optical interferometry in which light is modally dispersed through the optic cable and mixes at the fiber end producing a phenomenon known as the speckle. If the fiber is immobile, then the speckle will be stable. However, if the cable experiences vibrations, then the speckle will flicker. For this sensor to work, the time dependence of the speckle must be measured. This entails applying digital signal processing and fast Fourier transforms to the time-domain of the signal. Based on the costly acquisition of detecting arrays, Anderson also proposed a simple detector measuring the time variance of the speckle pattern. To test the design, a single mode fiber was linked with a multimodal fiber which was then fixed to the detector assembly. The system was deployed for a field test by placing the fiber near a track. Healthy wheel and flat wheel data were collected and compared, demonstrating promise in the sensor for detecting wheel flats. The device, however, was susceptible to the environment such as ground vibrations unrelated to the rail traffic. The system also exhibited the inability of tracking which wheel was damaged.

In 2011, Chuliang Wei et. al. [41] studied the real-time monitoring capability of Fiber Bragg Grating (FBG) sensors in a field test in the East Rail line of the Hong Kong Mass Transit Railway (MTR). Immune to electromagnetic interference (EMI), these sensors are basically an optic filter with a response driven by mechanical and thermal perturbations. With the use of an interrogator, wavelength changes within the FBG are measured which can be used to measure the magnitude of the perturbations. For this study, the mechanical perturbations involving the rail strain response upon wheel-rail interaction and the frequency component, that solely revealed the quality of the interaction, were used to assess the condition of the passing wheels. Four sensors were mounted adjacent to each other on the track; two for a northbound train and two for a southbound train. The sensors were then linked to an interrogator through 2 km (1.24 mi) of outdoor optic cable. Radio frequency identification (RFID) and cameras were also employed to identify the passing trains. The strain results indicated that the FBG sensor could detect all 48 axles of the passing trains of which train weight and speed effects could also be observed. Furthermore, it was determined that railcars with bad wheels had noisier strain responses than those of railcars with good wheels. However, as the methodology is a developing technique, continued studies are required to assess the accuracy and reliability of the method.

Like Anderson, Kepak et. al. [42] proposed another fiber-optic based solution that would involve a trackside detection method based on a Mach-Zehnder fiber-optic interferometer that was powered by a distributed feedback laser diode. The method was tested on a track running through a railway bridge with the use of a 200 m (219 yd) long fiber link to connect the detection elements. The test was conducted on a four-hour interval which detected 18 dynamic trains. The results indicated that the train operation could be detected, and that the sensor was able to detect trains even on the other track which promotes an indirect installation of the components. Challenges that were encountered were polarization fading, drift in the signal, and other signal-based problems. The researchers emphasized that these issues must be addressed before deploying the system and that they will be the next focus of their research to ensure future deployment. The capability of the method in detecting defective wheels, however, was vague. Like other wayside mounted methods, it is unlikely that a specific wheel can be linked to a defective wheel signal. In addition, the fact that other trains were indirectly detected can be problematic due to possible signal overlapping.

2.2.6 Other Researched Alternatives

Researchers have also diverged from traditionally studied techniques, such as vibrations and acoustics, to discover novel wheel monitoring methods. The application of polyvinylidene fluoride (PVDF) piezoelectric sensor technology was studied by Wang et. al. [43] in 2012 to monitor wheel-rail contact forces of out of round wheels (OOR) and tackle the shortcomings of strain-gauge methods such as WILDs. The proposed PVDF sensor would be employed as a wayside detector attached to the rail web. A 3-D simulation of wheel-rail contact dynamics was conducted on a simulation software known as ADAMS/Rail and the characteristics of wheel-rail impacts due to OOR wheels were also studied. To compare the performance of the PVDF strain sensor to traditional strain gauges, an experiment was performed to test for dynamic sensing, electromagnetic interference, zero drift, and repeatability. The results of this experiment revealed that the PVDF sensor was superior to the strain gage in these parameters, and it also showed better frequency response. Sinusoidal, square, and random load inputs were accurately reflected as well. The results promoted the device as capable of performing in dynamic strain conditions providing real-time monitoring with long-term stability. Nonetheless, the outlined experimental procedure is enough to reveal that the methodology is far from being ready for industrial applications.

In 2020, Turabimana and Nkundineza [44] investigated the detection of wheel flange wear with an inductive displacement sensor. The proposed system was intended to work in both static and dynamic railcar states with the capability of using an embedded data drive to map the wheel flange thickness history of an operating wheel. To determine the wear on the flange, the voltage output of the sensor would be converted into a distance measurement. If a flange thickness would reach its wear limit, the operator would get notified of the hazardous status of the wheel. The study also presented a CAD model design of the sensor holder for placement on the bogie frame to which a finite element analysis was also executed. To test the measurement accuracy of the proposition, an inductive sensor (with a 0-5 mm measuring capability) in combination with a rotating disk in contact with a grinder (mimicked flange on rail) were used. The measurements were manually calibrated with a digital voltmeter and a micrometer. The system was able to record the flange thickness versus time with an error of about 0.03 mm. However, the researchers did state that the sensitivity of the device demonstrated change after use, meaning that frequent calibration is needed to prevent inaccurate measurements by the device. Aside from calibration issues, additional experiments need to be conducted to investigate whether the system is capable of monitoring rail service conditions.

2.3 The Internet of Things

Each identified solution proposes a creative wheel defect detecting alternative, but the potential of most is extinguished by the inability of constant monitoring, the complexity of obtaining data, or the lead time on research to establish a reliable solution. As technology continues to advance, however, remote data management has increasingly become more accessible through internet-based devices. Application of these “internet of things” systems has revolutionized the methods in which many industries have optimized system performance and component defect detection, providing real-time feedback through the implementation of rapid data processing and wireless communication. Despite these advancements, the rail industry has lingered stagnant in adopting these advanced prognostic strategies. However, some companies have already started to mobilize their incorporation. A subsidiary of Amsted, Amsted Digital Solutions, has been promoting an “internet of things” (IOT)-based, ultra-low power onboard sensor that enables continuous condition monitoring for wheels [45]. Some additional claims the company has regarding the railcar information the device can communicate are load statuses, hatch securement, temperature statuses, brake statuses, and predictive wheel and bearing analytics. The system transmits data via satellite to a cloud where the data is stored and analyzed via machine learning. Customers can then access information of their assets utilizing an online portal. There is, however, no supporting evidence available regarding the accuracy of the system in identifying atypical wheel conditions.

Figure 14. Amsted Digital Solutions ^{TM} Communication Unit (left) and Sensing Unit (right) [45]

Perpetuum is another wireless technology capable of rolling stock wheelset monitoring. Both wheels and bearings health metrics are diagnosed by a three-axis accelerometer and a temperature sensor. The device is mounted onboard rail units and powered through a "battery-less" system that uses an electromagnetic energy harvester with a claimed life expectancy of up to 100 years. The functionality of the device has been proven with over one billion miles of study, and as of December 2016, about 7000 units have been installed in over five countries. Yet, despite the solid track record, there is uncertainty regarding the installation compatibility of the system. That is, the device, as seen in Figure 15, is designed to fit specific railcar wheel hubs. Based on the information given in the company website, it is unknown whether these sensors are capable of being mounted onto other railcar wheel configurations [46], [47], [48].

Figure 15. Perpetuum system mounted on railcar wheel hub [46]

Viezo, a company that specializes in sensor technology development, has also taken interest in developing a railcar wheelset monitoring system. Their device, Powerail, is intended to monitor the condition of freight railcar bearings and wheels through vibration and temperature data [49]. With that said, Powerail utilizes a single vibration and temperature sensor with respective measurement ranges of 0 to 16g and -40 to 85℃ (-40 to 185°F). Plus, with the use of GPS, wagon locations can also be tracked. Powerail is mounted through a single bolt on the axle box of railcars and powered through a patent pending PVDF-based energy harvester known as PolyFilm™. The system is composed of eight sensors and a gateway, communicating via Bluetooth, and using LTE to transmit data. Both devices (i.e., the sensor and gateway) have an expected lifetime of about 10 years and data transmission is encrypted end to end, permitting only the customer to view asset statuses. The company is already accepting pre-orders; with the first field installation to be set for Q1 of 2022 [50]. Nevertheless, although wheel flat detection is expected, no explanation is provided as to how bearing and wheel metrics will be differentiated using the embedded sensors. The operating range of the accelerometer is also concerning. Lower tier operating ranges for accelerometers are associated with a higher sensitivity to motion. Their incorporation in devices such as cell phones allows features like step counting or changes in screen orientation to be achieved. However, in a service environment like the railway industry, a high sensitivity to vibration can cause the sensor to saturate in normal operations, creating reliability issues for the device.

Joining the railway technology race, Hum Industrial Technology presents a wireless sensor ensemble that capitalizes on GPS, LoRa technology, and years of supporting research to monitor rolling stock wheelsets. The wireless condition monitoring system consists of: (1) the Hum Boomerang: a wheel-bearing health monitoring module that mounts to railcar bearing adapters, and (2) the Hum Gateway: a railcar wall-mounted and solar-powered communication unit, used to process and transmit acquired data to an online dashboard for clients.

Two accelerometers and a temperature sensor assess the real-time health condition of rolling stock bearings and wheels. The pair of accelerometers manage vibration sensing for bearings, wheels, and other miscellaneous railyard activities while the temperature sensor serves as an additional bearing health monitoring aid. Data transmission can be achieved at custom time intervals, tailoring automated safety to the needs of the user. Like other emerging rail monitoring technologies, the GPS feature permits fleet location visibility. However, aside from providing critical event location pins, key insights into deviations from expected behavior, such as aberrant running conditions of the track, or yard impacts can also be mapped. Driving device communications, LoRa technology enables low-power and long-range wireless connectivity between the onboard devices. The onboard mounting capabilities of the devices deliver other significant advantages such as facilitating continuous monitoring, reducing exposure to wearing elements, and track condition monitoring. As of Q2 of 2021, three field deployments have been mobilized. Their success, highlighted in part in this thesis, has been influential in showcasing the product, accelerating product demand worldwide.

CHAPTER III

EXPERIMENTAL SETUP AND PRELIMINARY ASSESSMENTS

To properly evaluate the efficacy of the onboard module in detecting high wheel impacts associated with wheel profile irregularities, the Boomerang prototype must be tested in an environment that closely mimics rail service operations and atypical wheel behaviors. Hence, this chapter presents the experimental setup and equipment as well as the methodologies used to systematically evaluate and validate the performance of the prototype Boomerang device.

3.1 Single Bearing Test Rig

The University Transportation Center for Railway Safety (UTCRS) dynamic single bearing tester (SBT) pictured in Figure 16 was employed for this investigation to simulate the load and speed operating conditions a railcar experiences in the field. The SBT is designed to closely mimic rail service conditions of individual railcar tapered roller bearings of AAR classes E (6 in ×11 in), F (6½ in ×12 in), G (7 in ×12 in), or K (6½ in ×9 in). Listed in Table 6 are the dimensions and AAR rated load capacities of these four bearing classes.

Table 6. Bearing classes with dimensions and AAR rated load capacities

Bearing Class	Size [mm]	Size [in]	Load [kN]	Load [lbf]
Class E	152×278	6×11	117	26300
Class F	165×305	6½×12	153	34400
Class G	178×308	7×12	169	38000
Class K	165×229	6½×9	153	34400

In the field, a total of eight bearings equally support the load of a railcar, exerted vertically on them by the bogie side frames. Once in service, the railcar mainly operates under fully loaded or unloaded conditions. When fully loaded, the bearings support 100% of the load while at an unloaded state, the bearings only support about 17% of the full load. For example, if a railcar is equipped with class F or K bearings, then each bearing would support 153 kN (34.4 kip) and 26 kN (5.85 kip) at fully loaded (100%) and unloaded or empty (17%) states, respectively. On the SBT, the fully loaded and unloaded conditions a bearing experiences in rail service are achieved by positioning the test bearing at the end of a specialized axle cantilever style. Here, a load cell, driven by a hydraulic cylinder, vertically exerts load onto the bearing. The hydraulic cylinder can load bearing classes accommodated by the tester with up to 150% of their rated capacity. An Arduino-based load controller is also used to adjust and maintain desired pressure/load outputs manually or automatically.

Table 7. Single bearing tester (SBT) speed conversion table

Axle Speed [rpm]	**Equivalent Track Speed [km/h]**	**Equivalent Track Speed [mph]**
234	40	25
280	48	30
327	56	35
374	64	40
420	72	45
467	80	50
498	85	53
514	89	55
560	97	60
618	106	66
700	121	75
796	137	85

The SBT is also equipped with a 22 kW (30 hp) variable frequency motor that can simulate train traveling speeds of up to 137 km/h (85 mph). This permits the test bearing to be subjected to various test speeds. Commonly tested SBT speeds can be found in Table 7. Industrial-size fans producing an average airflow of 6 m/s (13.4 mph) are used to simulate the convection cooling conditions experienced by bearings in freight rail service.

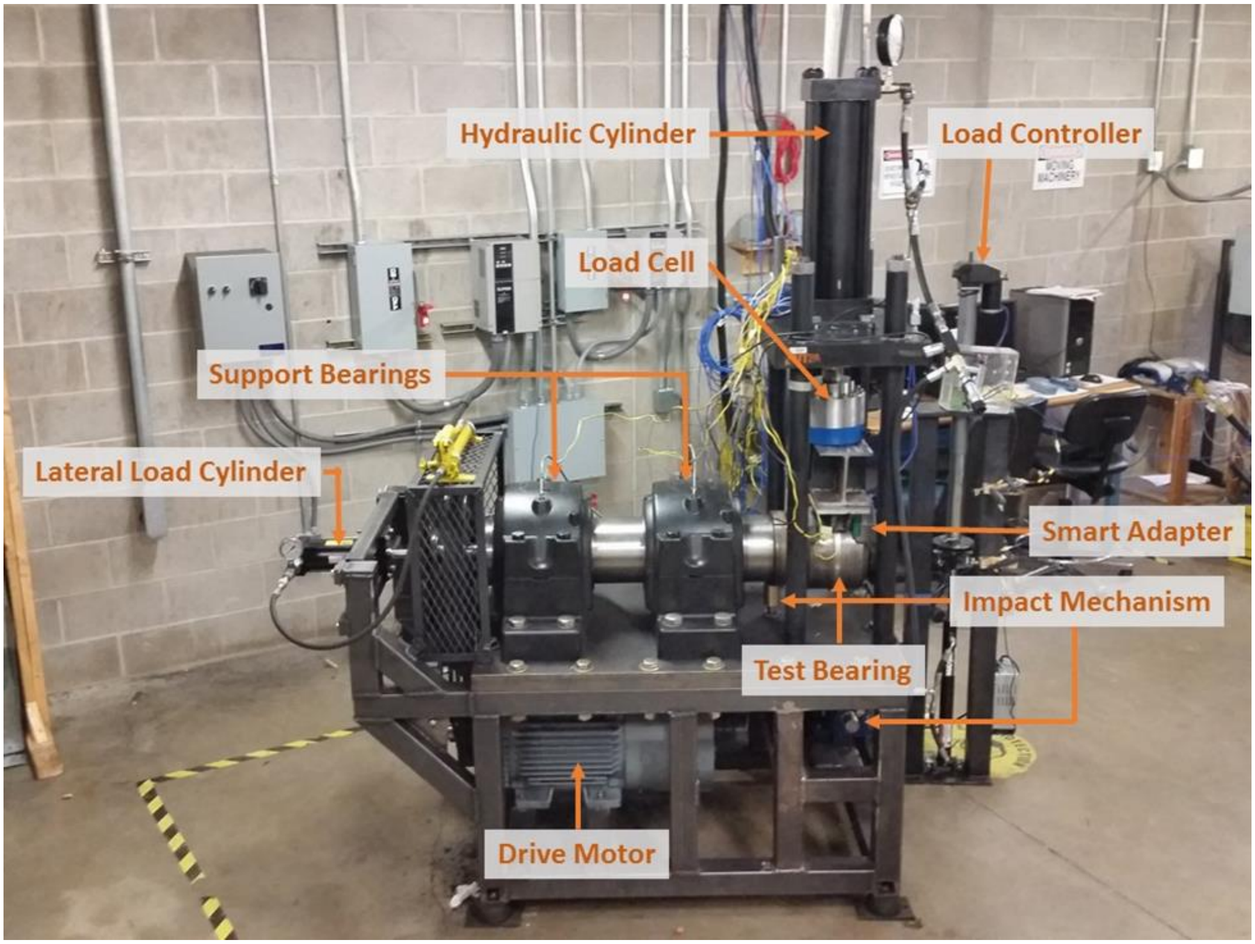

Figure 16. Single bearing testing rig (SBT)

3.2 Condition Monitoring Systems

To quantify the vibration levels in the performed railcar simulations, two onboard sensor modules were affixed to a specially machined class F bearing adapter. Namely, the two sensor modules were the HUM Boomerang prototype and the UTCRS wireless module (UWM). The modifications to the bearing adapter were methodically performed to allow both sensor modules to align their accelerometers radially with the bearing center in the loading zone as shown in Figure 17.

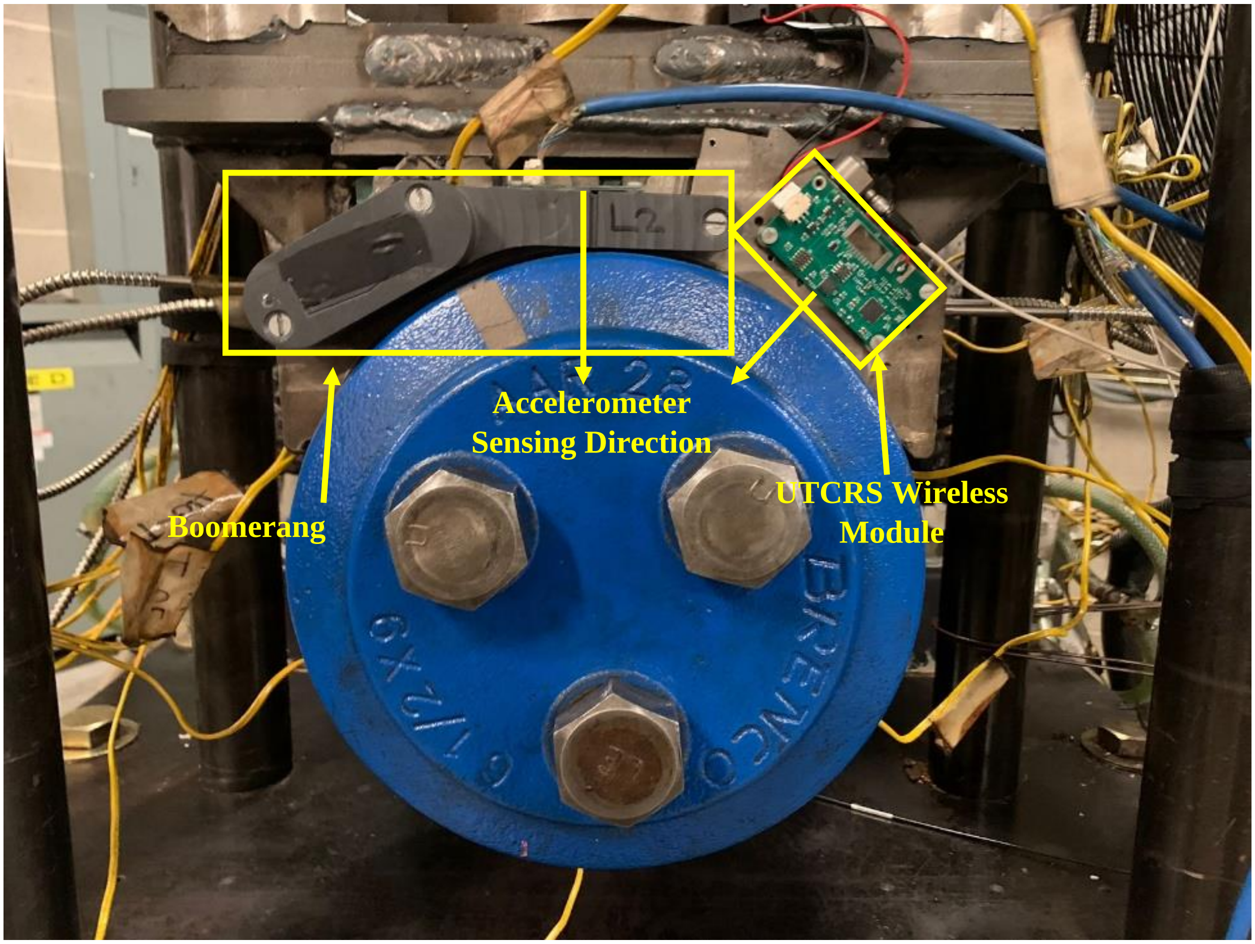

Figure 17. Boomerang and UTCRS wireless modules fixed to a bearing adapter for laboratory testing

3.2.1 Boomerang and Gateway Ensemble

As mentioned in Section 2.3, the HUM Boomerang prototype is part of an ensemble of wireless systems in which the condition monitoring module or Boomerang functions in combination with a solar-powered central communication unit known as the Gateway. The Gateway, presented in Figure 18, acts as the data relay bridge between the onboard condition monitoring module and the railcar owner. Specifically, the Gateway retrieves the attained data by the Boomerang utilizing LoRa technology. In field operations, rolling stock bearing information is then wirelessly transferred via cellular data transmission services and stored into HUM’s online dashboard. Here, the software interface of the server assumes control over data analysis, generating automated notifications for the end user when a bearing health index surpasses established thresholds. The Gateway is necessary for flashing the Boomerang with the latest software updates. Sampling time interval modifications, Boomerang-Gateway linking, and other programming procedures are also enabled by the Gateway.

Figure 18. HUM central communication unit (i.e., Gateway)

The Boomerang prototype, displayed in Figure 19, employs two accelerometers and one temperature sensor to provide timely bearing health conditions. For the purposes of this thesis, however, only the data output of the two accelerometers will be used, and they will be denoted as Accelerometer 1 (A1) and Accelerometer 2 (A2) for the rest of this thesis. A1 is a single-axis accelerometer with a data sampling capability of 5,200 samples per second. A2 is a three-axis accelerometer that can collect a maximum of 780 data samples per second for each axis. A1 and A2 have unique g-acceleration operation ranges. Accelerometer 1 has an operating capacity up to 100 g’s while Accelerometer 2 can collect g-accelerations at a maximum of 200 g’s.

Additionally, A2 has an integrated attribute that enables the maximum operating range to be adjusted to either 100 or 200 g's based on modifications to the main code that can be pushed to the Boomerang by flashing its main circuit board. Note that, once a measured value exceeds these disclosed ranges, the sensor will "saturate", and the exact g-reading will be undefined. If this occurs, the data will simply demonstrate values at the maximum limit of the sensor.

Figure 19. HUM Boomerang prototype

Both accelerometer vibration readings are acquired by the AC voltage fluctuations produced when they are mechanically stimulated. To harness the vibrational output in "g", a root mean square (RMS) operation must be performed to the voltage output. Hence, the Boomerang accelerometers provide bearing health metrics in two main ways: (1) root mean square (RMS) and (2) maximum acceleration [g]. The RMS index indicates the average bearing operating status, and it has been the preferred bearing diagnostic tool by UTCRS due to its successful predictive and accurate bearing health assessments over years of studies [28]. Any deviations from established thresholds signal the presence of an internal flaw either in the cup (outer ring), cones (inner rings), or rollers of the bearing. On the other hand, the maximum acceleration [g] signifies the absolute maximum vibration signature the accelerometer captured within an allotted data acquisition interval. The latest version of this sensor only allows both parameters to be obtained as numeric characters, yet they can be downloaded in a time-stamped manner through ".csv" files for further analysis. Current efforts are being conducted to allow downloadable raw vibration data for a more complete insight on component performance.

As this thesis is intended to present the high wheel impact sensing capabilities of the Boomerang, one of these parameters must be utilized to accomplish this feat. Although RMS has been vital in bearing condition monitoring for UTCRS, a different approach might be required for diagnosing a high impact wheel. This is due to how wheel impacts are instantaneous and acute in nature. In past studies, a periodic display of signal spikes within a data set have been proven to indicate their presence [35]. As an RMS operation involves taking an average of the acquired AC voltage data, this process could conceal these singularities. That is, a continuous signal can nullify any periodic episodes as more “average” data points are available. Considering this logic, the empirical data collected and presented for this thesis will be based on the maximum g output of the Boomerang.

3.2.2 UTCRS Wireless Module

The UTCRS wireless module (UWM), seen in Figure 20, is a battery-powered, onboard health monitoring sensor capable of collecting data at a sampling rate of 5,200 Hz. It is instrumented with a single-axis accelerometer, a temperature sensor, and a Bluetooth transmitter. With these features, the device can transmit bearing temperature and vibration data via Bluetooth to a Raspberry Pi 3 Model B+. The embedded accelerometer is the same as Accelerometer 1 (A1) of the Boomerang. However, instead of having the same 100g maximum, a modification in the UWM expands the operating range to a maximum of 123g. A Python^{TM}-based platform was used to perform data acquisition tasks. For this thesis, data acquisition was dependent on two main codes: (a) Multiwirelessfourseconds.py and (b) Multiwirelessfullbits.py.

Multiwirelessfourseconds.py (a) collects four seconds of RMS, maximum acceleration [g], and temperature data. These metrics can be transmitted in as fast as 15 seconds or at any time interval of interest thereafter, yet they can only be obtained as numeric characters.

Conversely, Multiwirelessfullbits.py (b) can only collect one second of RMS, maximum acceleration [g], and temperature data at a minimum transmission rate of one minute and 45 seconds. However, unlike (a), (b) can log both numeric characters and raw voltage values. For both codes, the values can be saved and downloaded as ".txt" files. In case of the numeric characters, their ".txt" file can be used to create Excel spreadsheets where the data can be organized and analyzed. The raw voltage values can be plugged into MATLAB® where three levels of vibration analysis can be performed: Level 1: converts the raw voltage data into RMS to indicate bearing health, Level 2: uses RMS to classify defect type with a specified degree of certainty, and Level 3: discloses the approximate size of the defect in terms of surface area [28].

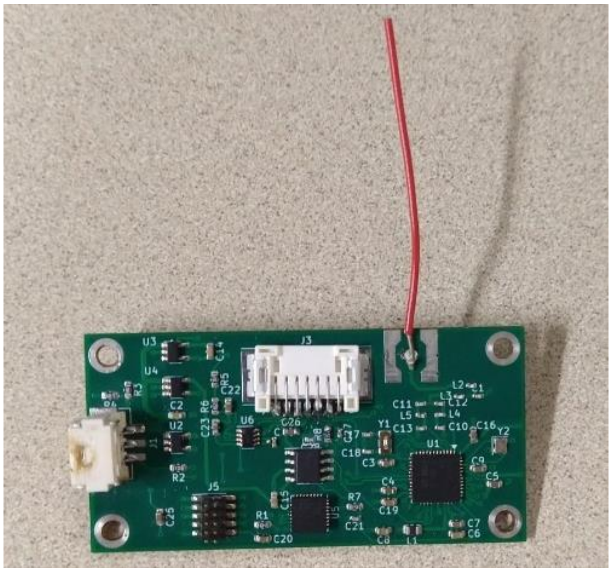

Figure 20. UTCRS wireless module (UWM)

3.3 Impact Mechanism Configuration

The impact system depicted in Figure 21 and Figure 22 was used to simulate the high wheel impacts a defective wheel would experience in rail service. The mechanism is assembled within the single bearing tester (SBT) frame, and it consists of five key components: an impact head, a spring-driven impact hammer, a lever, a cam, and an inverter drive motor. The inverter drive motor is a 7.46 kW (10 hp) variable frequency drive (VFD) motor. By configuring the input frequency or voltage on the VFD, the speed of the motor can be adjusted, allowing for different impact frequencies to be tested. Connected to the motor is a solid steel shaft retrofitted with a custom-made cam that sits between two journal bearings. The cam creates a rotational to translational energy conversion in the system as it is connected to a lever that sits on a small shaft between two smaller-size journal bearings. This lever, which is 21.51 cm (8.47 in) in length, has a Delrin homopolymer roller at the cam-lever interacting end to reduce friction and wear between the components. It connects to the impact hammer via a linkage housed within the impact mechanism frame securing the impact hammer and lever together using two clevis pins locked with cotter clips. Because the lever is connected to the impact hammer, the energy transfer between the cam and lever gets transferred to the impact hammer as well. This energy transfer, however, is limited to the rotation of the cam. Thus, to maximize the energy output of the impact hammer, a spring with a specified constant is fitted on top of the impact mechanism frame. The spring is secured into position under a square plate that is part of the impact hammer’s structure.

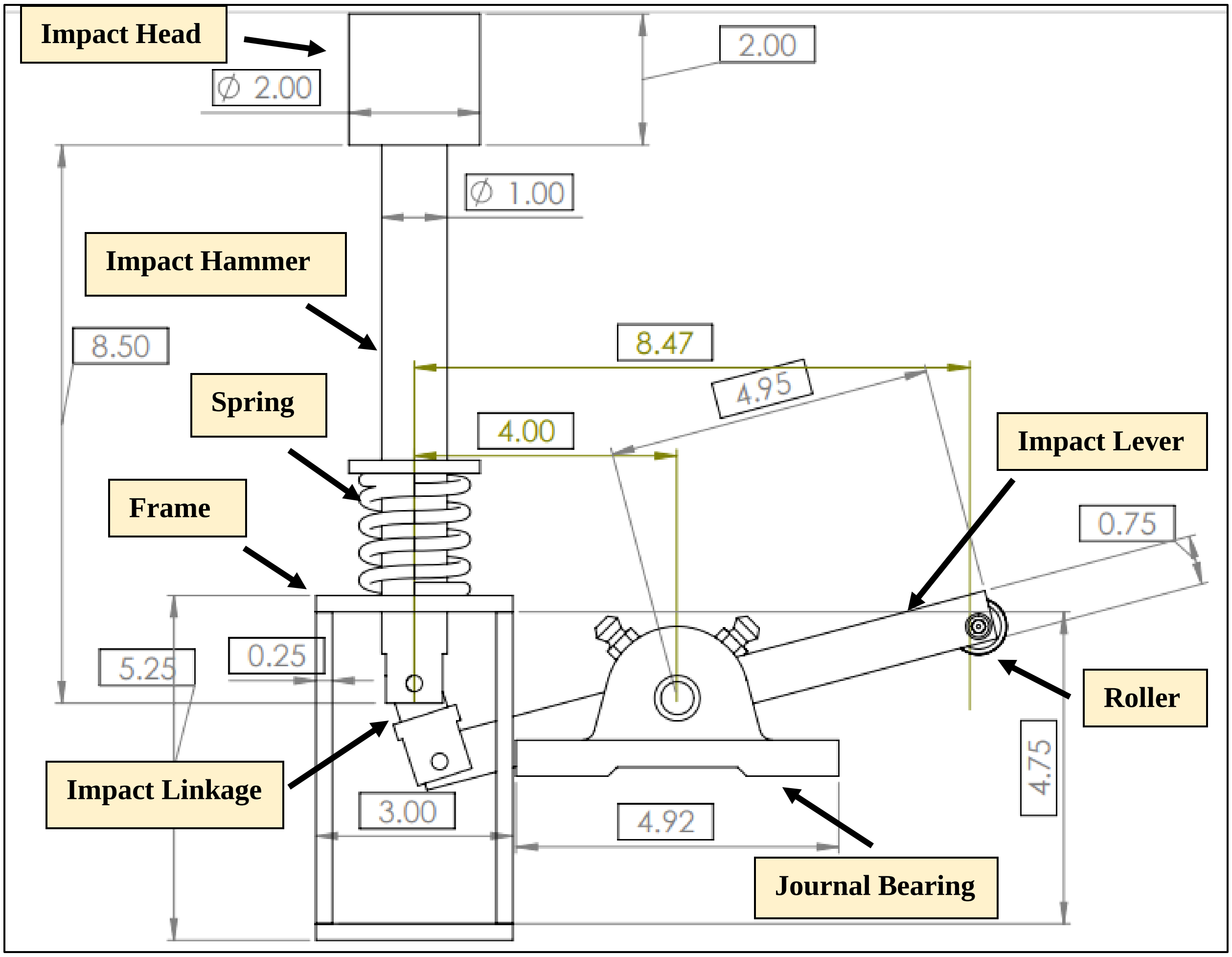

Figure 21. Impact mechanism CAD drawing (dimensions in inches)

Hence, to illustrate the operation of the impact mechanism, as the lever is pushed upwards by the rotation of the motor driven cam, the impact hammer is pulled down and the spring now has a substantial amount of potential energy from its deformation. As the cam keeps rotating, the geometry of the cam allows for the lever to be released causing the stored potential energy of the spring to become kinetic energy, catapulting the impact hammer into motion. Yet, to simulate a wheel impact, this mechanism needs to hit an area on the test axle that emulates a railcar wheel position on an actual railcar suspension frame. For this reason, a circular slot within the SBT frame is strategically positioned underneath a steel impact ring assembled onto the SBT axle. The geometry of the slot allows the impact hammer to protrude through the SBT frame, enabling an impact head to be fastened onto the protruding end of the impact hammer . Reanalyzing the behavior of the mechanism, as the impact head jolts upwards from the potential energy release of the spring, the impact ring, which simulates a railcar wheel on the test axle, provides a medium for this impact head to hit, replicating a high wheel impact.

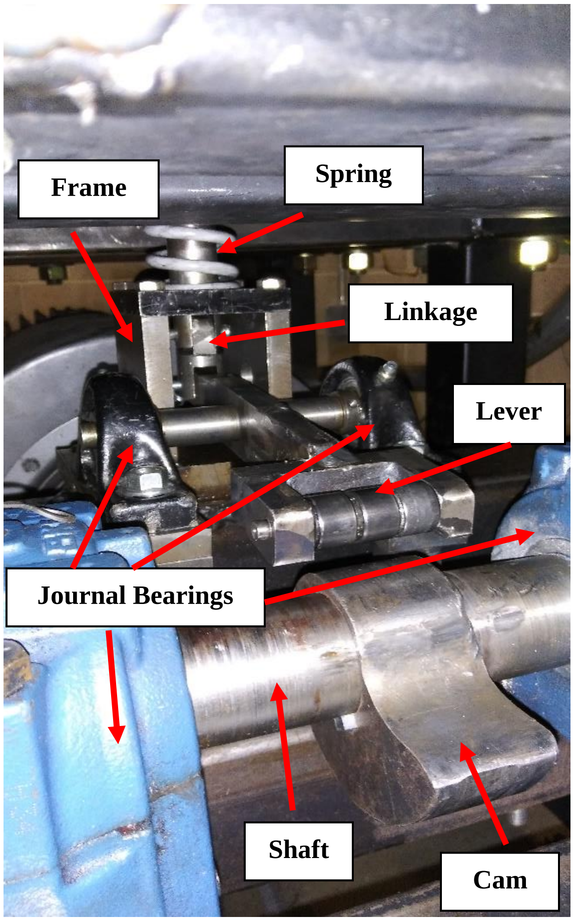

Figure 22. Impact mechanism components

The impact head, pictured in Figure 23, is fabricated from a solid steel cylinder that has been machined to provide a hollow end that permits the impact head to be fastened to the impact hammer via a pressure fitted Delrin homopolymer sleeve. Moreover, the impact head is retrofitted with an L-shaped steel bracket and a press-fitted brass pinned disk. The L-shaped bracket is used to equip the impact head with a shock accelerometer that can acquire acceleration data during impact testing. This bracket is affixed to the impact head via two threaded holes and screws. To suppress the wear that would be generated from the high-speed impact and axle rotation contact between the impact ring and head, a brass pinned disk was machined and press-fitted on top of the impact head. The disk has a diameter of 6.22 cm (2.45 in) and a thickness of 0.65 cm (0.26 in). The stem or pin section of the disk is 1.27 cm (0.50 in) in diameter with a length of 1.27 cm (0.50 in). The impact head was machined to house the entirety of the brass disk pin and about 0.32 cm (0.13 in) of the disk thickness. By pressure fitting the pinned disk, the piece is stabilized and primed to withstand frequent high impacts. Simultaneously, friction at impact contact is reduced, minimizing premature fractures associated with the harsh impact tests.

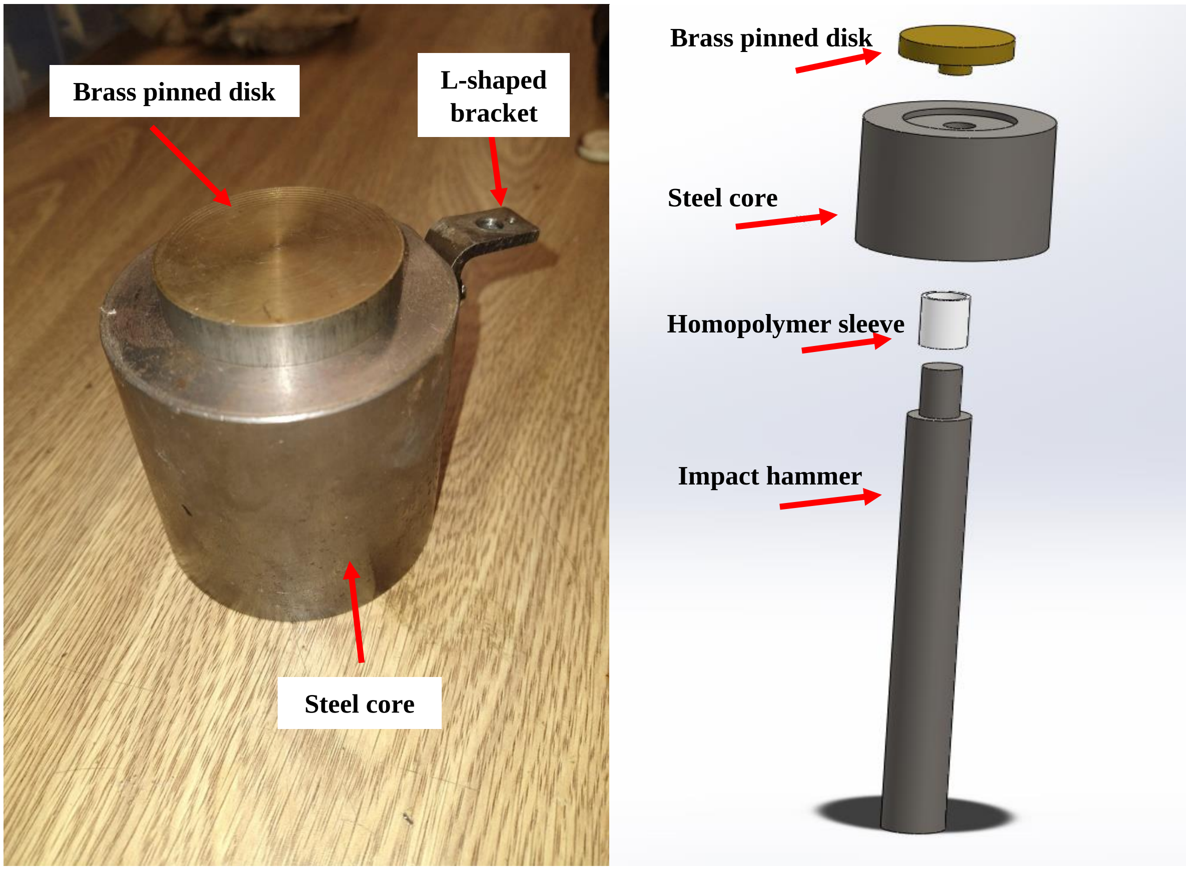

Figure 23. Impact head (left) and CAD drawing of impact head and hammer assembly (right)

3.3.1 Impact Mechanism Frequency Evaluation

The functionality of the impact system is based on several transfers of energy. In turn, these exchanges create mechanical losses that impede the VFD input frequencies from being true. In other words, a VFD input of 10 Hz will not equal a 10 Hz impact frequency output. To this end, an experiment was constructed using the SBT and impact system to determine the precise input to output frequency yield. The test involved 60 seconds of continuous impacts with a 67 N/mm (384 lb/in) spring for each VFD input frequency (i.e., 1-60 Hz). The reciprocal of the time between successive impacts for each input would then be used to calculate the actual output frequency. To acquire those impacts, a shock accelerometer with a 20,000g measuring range and a 0.2681 mV/g sensitivity (factory calibrated) was affixed to the L-shaped bracket of the impact head.

Figure 24. Brüel & Kjær shock accelerometer (20,000g measuring range)

A cable with a gold-plated BNC connector was then used to hook up the accelerometer to a National Instruments (NI) 9234 data acquisition cartridge that was attached to a National Instruments (NI) Compact Chassis (cDAQ-9174). Using the technical parameters of the accelerometer and the DAQ, a LabVIEW code was built to generate an Acceleration [g] vs. Time plot. After performing the tests, the g-acceleration per input frequency data was analyzed using MATLAB™ and the respective output frequencies were calculated. In effect, the analysis determined that the input to output capability of the VFD was skewed. The maximum output frequency that could be achieved was 3 Hz, or the equivalent of a 91.44 cm (36 in) railcar wheel containing a single anomaly traveling at roughly 31 km/h (19 mph). In addition, to get output impact frequencies of 1, 2, and 3 Hz, VFD frequency inputs of 19, 38, and 57 Hz are required, respectively. This relationship is presented in Table 8.

Table 8. VFD input to impact frequency output relationship for UTCRS impact mechanism

VFD Input [Hz]	Impact Frequency Output [Hz]
19	1
38	2
57	3

3.3.2 Impact Force Evaluation

To develop a sensible understanding of what impact forces the UTCRS impact mechanism can generate, another methodical experiment needed to be devised. Since the only viable approach of adjusting impact forces on the impact mechanism was by swapping springs, four additional springs with distinct spring constants were acquired to produce a spring to impact force correlation. In particular, the spring constants were 18, 26, 44, 51, and 67 N/mm (i.e., 104, 147, 249, 289, and 384 lb/in, respectively). Each selected spring was sequentially mounted onto the impact mechanism and tested for 30 seconds using the maximum impact frequency output of 3Hz. To gauge the resulting impact accelerations, the same 20,000g accelerometer setup mentioned in Section 3.3.1 was employed. After completing the tests, the acquired g-acceleration profiles for each spring were analyzed using MATLAB™.

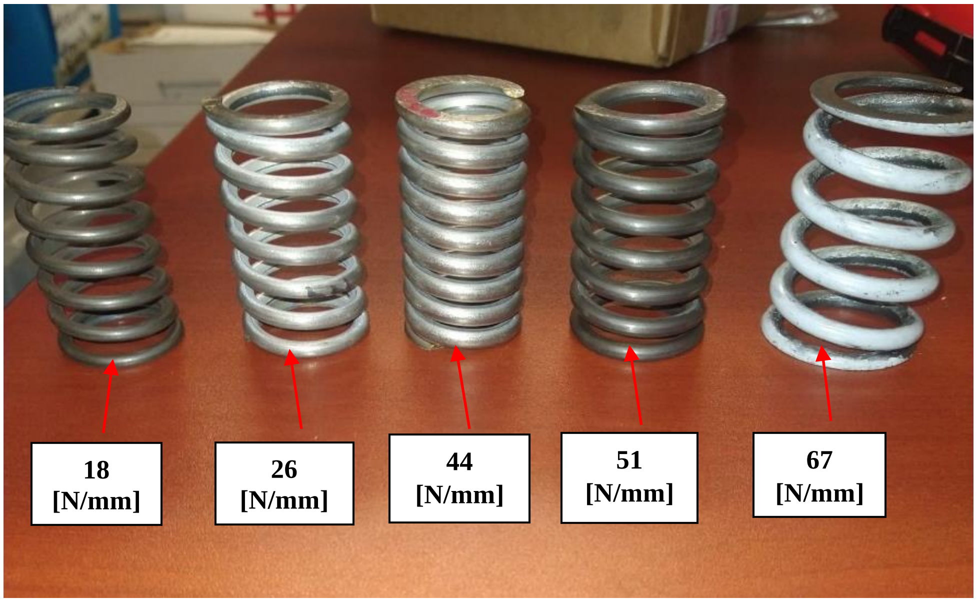

Figure 25. Selected springs with distinct spring constants

To demonstrate the MATLAB^{TM} analysis process, an impact acceleration profile plot of one of the tested springs can be observed in Figure 26. The data callouts depicted in the plot signal some of the maximum g-accelerations collected for a tested spring (67 N/mm or 384 lb/in). Overall, each successive and absolute maximum peak in the plot was used to compute the average g-acceleration peak and was repeated for each tested spring. The respective value was inserted into Equation 1 to calculate the impact force (F_N) in Newtons [N], where m is the combined mass of impact hammer and head in kilograms [kg] (i.e., 4.06 kg or 8.95 lb), g is the gravitational constant in [N/m^2], and G is the calculated average peak impact force acceleration in [g]. Then, by using Equation 2, the impact force in Newtons was converted into a pound force [lbf] value and denominated as F_{lbf}. The resultant impact forces for each spring are found in Table 9. Notably, the highest impact force that could be exerted was by the 67 N/mm (384 lb/in) spring which provided a force of about 320 kN (72 kip). To illustrate the relationship between the spring constants and the obtained impact forces, the data from Table 9 was used to derive

Figure 27. The plotted data was fitted with a linear regression model that corresponded to a goodness-of-fit (R^2) value of 99%.

$$F_N = m \times g \times G \tag{1}$$

$$F_{lbf} = F_N \times 0.2248 \tag{2}$$

Table 9. Spring constant to impact force relationship for UTCRS impact tester

Spring Constant [N/mm]	Spring Constant [lb/in]	g-acceleration [g]	Impact Force [kN]	Impact Force [kip]
18	104	1661	67	15
26	149	2063	85	19
44	249	6063	240	54
51	289	6646	267	60
67	384	8026	320	72

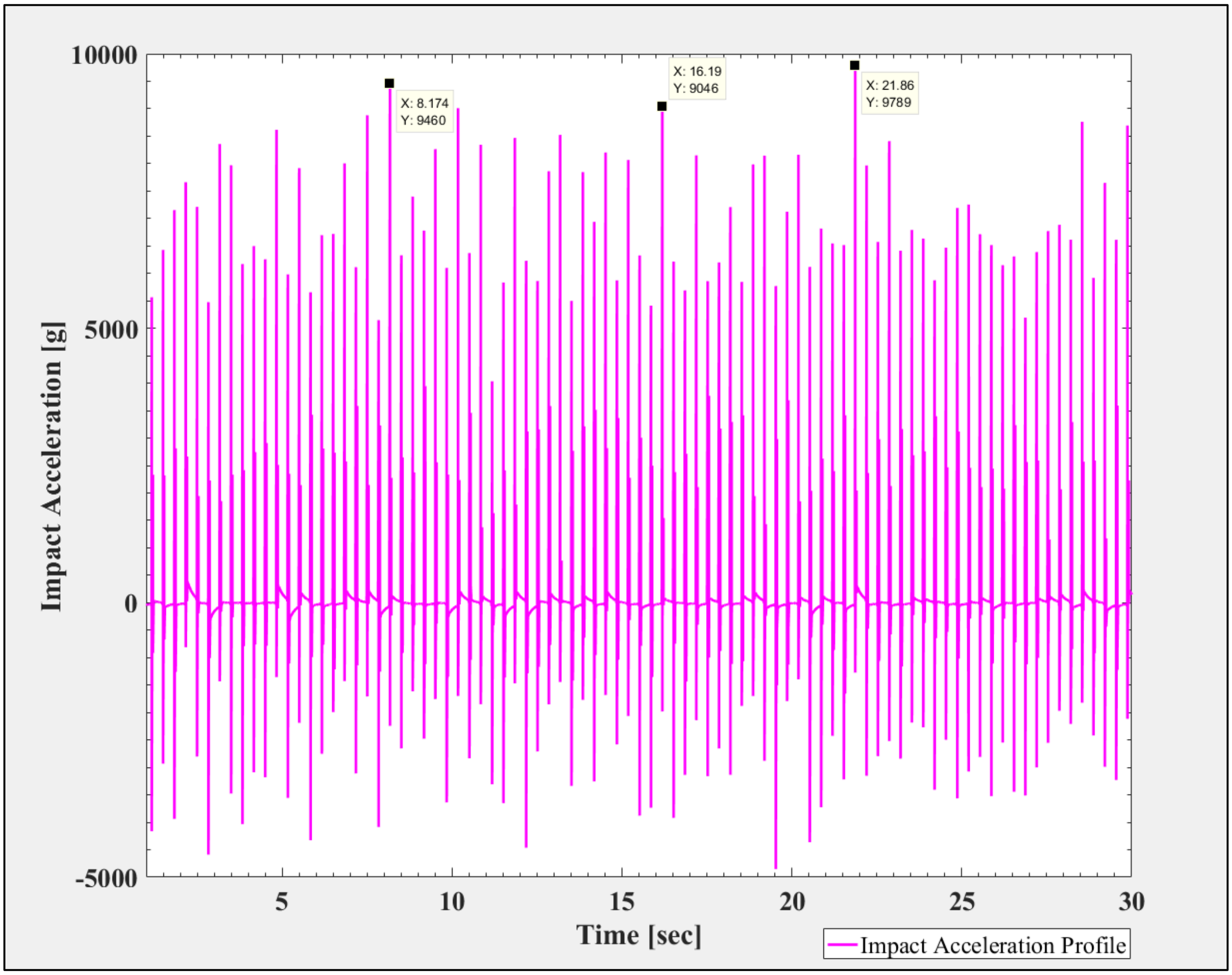

Figure 26. MATLAB generated plot for 67 N/mm (384 lb/in) spring impact acceleration profiles

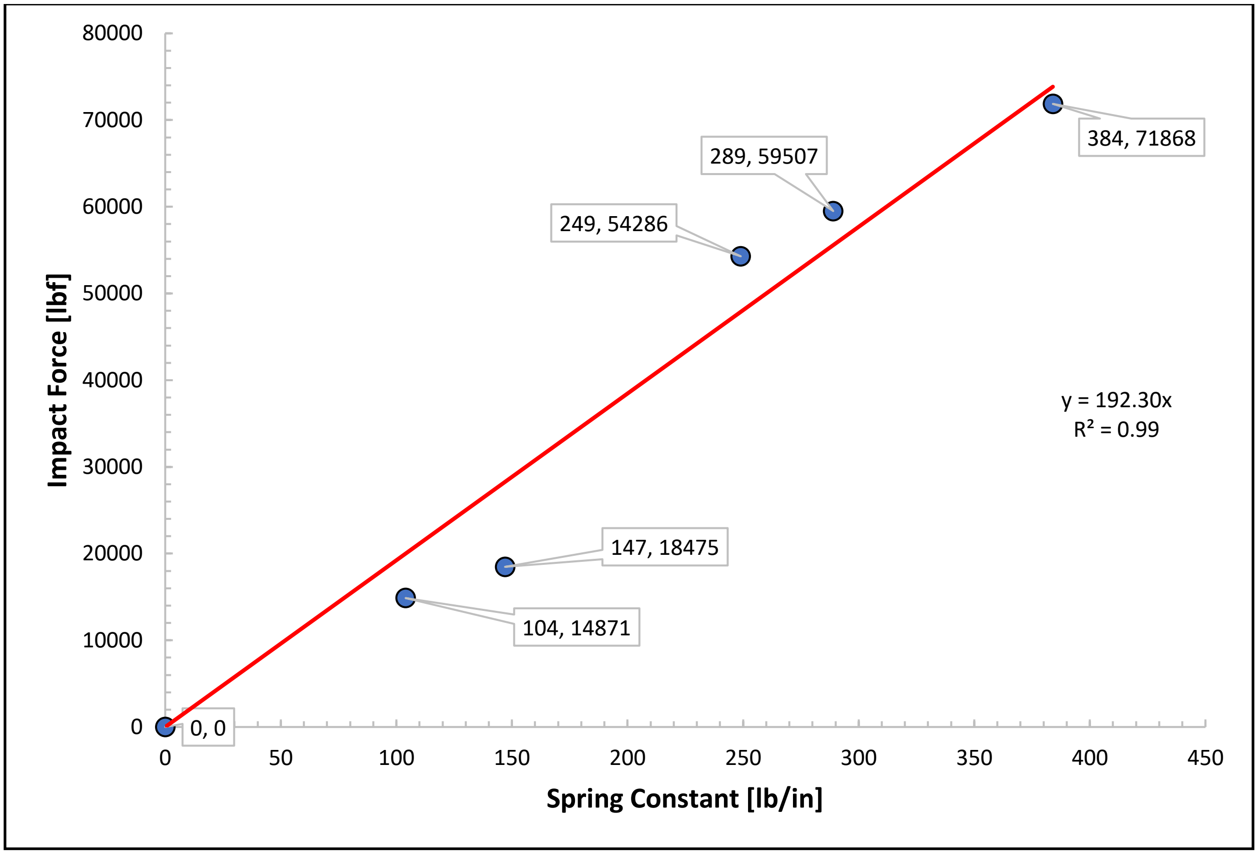

Figure 27. Linear regression fit correlating the spring constant [lb/in] to the impact force [lbf]

3.4 Boomerang Maximum Acceleration [g] to Impact Force Correlation

An effective wheel impact force criterion needed to be implemented to support future in-field wheel monitoring. As the high wheel impact detection capability of the Boomerang will be assessed through its maximum acceleration [g] output, an experiment was designed to determine the correlation between maximum g's and impact force. The experiment entailed the dynamic operation of a class F control (healthy) bearing on the SBT under the influence of 3 Hz impacts by each spring presented in Section 3.3.2. The control bearing was subjected to both unloaded (empty) and fully loaded railcar scenarios under dynamic operations of 40 and 85 km/h (25 and 53 mph). A total of 10 maximum g data points were collected per spring. Once the testing was completed, the average maximum g-acceleration output for the selected railcar conditions were calculated and organized in Table 10. It is important to state that the devised correlation was based on the maximum acceleration output of Accelerometer 2 (A2) only. Although Accelerometer 1 (A1) was functional in this experiment, a manufacturing error prevented A1 from being active for a field test that will be presented later in this thesis. Therefore, A1 data was excluded from this correlation. In addition, the results of this experiment were acquired utilizing the 200g setting of A2 to maximize the response of the device. With this in mind, an impact force of 72 kip resulted in an average maximum g-value of about 144g, while the lowest impact force of 15-kip corresponded to roughly 46g.

Table 10. Boomerang average maximum acceleration [g] output to impact force relationship (no filter)

Average Maximum Acceleration [g]	Impact Force [kN]	Impact Force [kip]
46	67	15
49	85	19
66	240	54
100	267	60
144	320	72

Since the Boomerang currently does not possess a feature that promptly informs railcar load conditions, it was redundant creating a maximum acceleration [g] to wheel impact force model that required both 17% (empty railcar) and 100% (full railcar) load conditions. Furthermore, railcar speed is variable and may change frequently especially in rail segments where the train passes through urban areas. Introducing an impact force index for each railcar speed would also prove to be unnecessarily complex. Hence, the devised relationship presented in Table 10 provides a simple provisional model for wheel condition tracking. Combined with FRA wheel impact guidelines, the latter could optimize maintenance intervention by following a series of thresholds that signal different levels of concern at each wheel impact force. This framework is bound to change with any modifications to the design of the Boomerang circuitry or with continued in-service acquisition of data. Nevertheless, the simplicity of the proposed model allows for swift enhancements.

3.5 Pilot Field Test Setup

A pilot test was conducted in cooperation with HUM and a private railroad to investigate the ability of the wireless module to detect high wheel impacts in field service operations. The study involved the assembly and installation of 40 wireless onboard condition monitoring devices on the bearing adapters of five randomly selected railcars of an active rail transport route. Over the course of two months, the installed Boomerangs transmitted wheelset health metrics to HUM's server where the data was downloaded and scrutinized. Upon observation, the data from two Boomerangs began indicating maximum acceleration values coincident to a laboratory simulated high wheel impact. The finding was presented to HUM, and a mutual agreement among all parties involved was reached to remove three wheelsets from service for examination. Specifically, the removed wheelsets would target the flagged wheelset and two apparently normal wheelsets to allow for a suitable comparison.

3.5.1 Field Installation

Prior to railcar installation, a total of 40 Boomerangs and five Gateways were assembled at UTCRS. Eight Boomerangs were programmed to communicate with a specific Gateway unit (i.e., eight Boomerangs per Gateway). This entailed prescribing each Gateway with a unique channel number to avoid communication interference between the modules as well as for future data organization practices. For example, "Gateway 1" was programmed to channel 10 and each of the eight Boomerangs pertaining to that Gateway were labeled in sequential order (i.e.,11, 12, 13, etc.).

Figure 28. Assembled Gateway and Boomerang units at UTCRS

Once fabricated and programmed, HUM then performed the onsite installation procedures. A single gateway was fixed per railcar while ensuring proper positioning of the fixture for optimal solar exposure and communication with the condition monitoring modules. Next, after modifying the railcar bearing adapters using basic drill and tap techniques, the Boomerangs that were programmed to the respective Gateway were secured onto the bearing adapter frontal plane via screws. This procedure was repeated for all five randomly selected rail transport units.

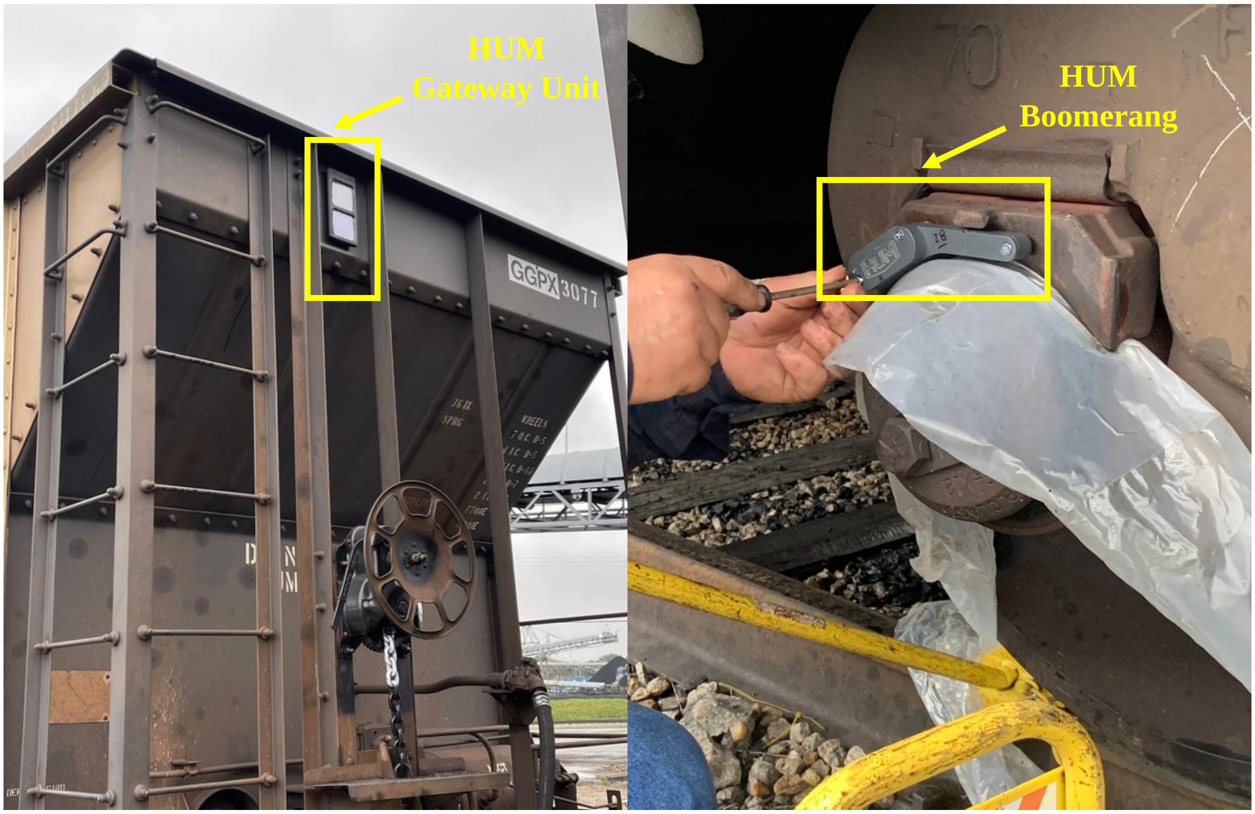

Figure 29. Installed HUM Gateway unit (left) and HUM Boomerang installation (right)

Subsequently, using their fixed positions, the Boomerangs were registered on the HUM server in conformity to the Association of American Railroad (AAR) wheel identification layout seen in Figure 30 to facilitate the identification of the sensors when conducting their data output analyses. As a note, AAR wheel identification states that railcar axle order begins at the hand brake end of the railcar which is denoted as the B-end. By using the B-end as a reference point, the left and right sides of the railcar can also be located.

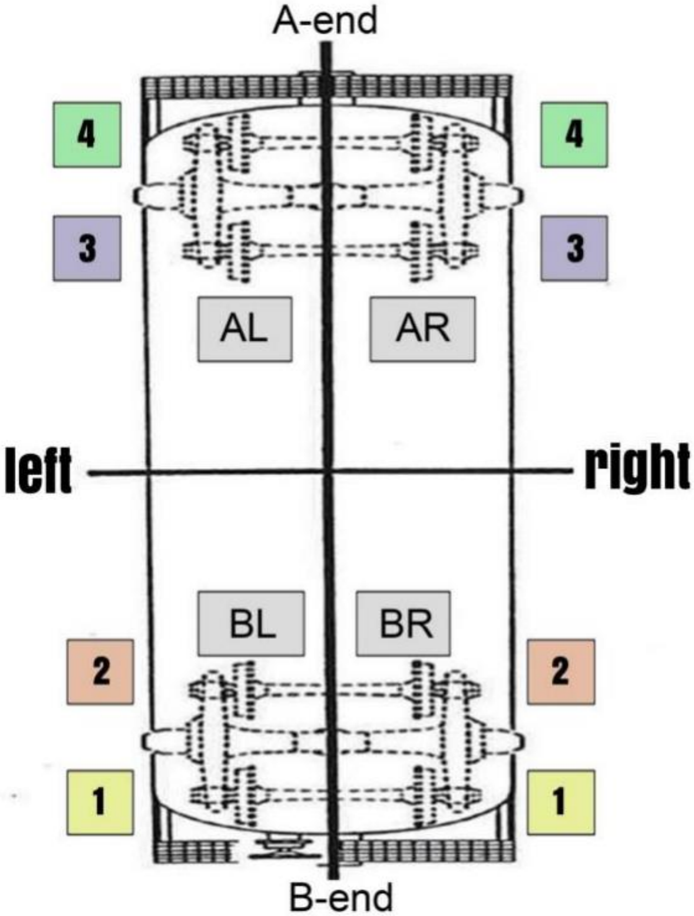

Figure 30. Railcar side and end identification diagram

3.5.2 Axle Removal Process and Inspection

Based on the event of two Boomerangs signaling high impact loads for a particular railcar wheelset, the UTCRS team convened with HUM representatives to notify them about the wheelset status. This information resulted in HUM requesting from the railcar owner the removal of the possibly atypically performing wheelset along with two apparently healthy wheelsets. Essentially, this request would allow for validation of the capability of the Boomerang to distinguish between standard and substandard wheelsets in rail service operation.


Figure 31. Wheelset removal process

After coordinating with the private railroad and the wheelset removal party, the UTCRS team traveled to the rail depot to oversee the removal and interchange process depicted in Figure 31. Once removed, the wheelset removal entity conducted careful inspection of the three wheelsets. This led to the identification of wheel flats and spalls on both wheel treads of the axle of interest, verifying the high wheel impact prognosis given by the Boomerangs. The other two wheelsets, used for comparison, demonstrated conformity to AAR wheel profile standards. An example of one the removed healthy wheelsets and the defective wheel set can be observed in Figure 32 and Figure 33, respectively. Following the AAR wheel identification diagram of Figure 30. Railcar side and end identification diagram, “L2” and “R2” indicate the left and right locations of the railcar while the “2” is the wheelset position.

Figure 32. Axle 2 low-concern wheelset (healthy)

Figure 33. Axle 2 high-concern wheelset (defective)

To illustrate the maximum g behavior of the three removed wheelsets, the pre-and post-wheel changeout maximum g indices of these removed axles was used to create maximum acceleration [g] versus speed [km/h] plots. These plots will be presented in Chapter VI and they will be supported by the maximum g and impact force correlations presented in Section 3.4.

CHAPTER IV

LABORATORY EVALUTION OF BOOMERANG PROTOTYPE

Although the purpose of this thesis is to assess the capability of the Boomerang in detecting high wheel impacts, it is important to restate that the other intended function of the device is to provide bearing health metrics for railcar owners. Therefore, if the module were to be employed for the relay of both wheel and bearing conditions, then the vibration sensors within the Boomerang should be capable of simultaneously diagnosing both components. This raises the question of whether the Boomerang can detect bearings with defects given the presence of high wheel impacts and vice versa. For this reason, this chapter demonstrates the how the Boomerang can identify high wheel impacts under the influence of three distinct and common bearing conditions which include: (1) all healthy bearing components, (2) a bearing with a defective cup (outer ring), and (3) a bearing with a defective cone (inner ring).

4.1 Laboratory Boomerang Evaluation Methodology

The high wheel impact detection efficacy of the Boomerang was evaluated by analyzing the maximum acceleration [g] data collected for impact and no-impact tests carried out on select class F bearings. The impact testing was conducted by employing the single bearing test rig (SBT) and impact mechanism described in Sections 3.1 and 3.3, respectively. Based on the results shown in Section 3.3.2, the 67 N/mm (384 lb/in) spring was installed on the impact system, replicating the highest attainable impact force of 320 kN (72 kip) by the mechanism. Furthermore, as the Boomerang is intended to identify wheel impacts at a wide range of railcar speeds, the device was tested under dynamic bearing operation of 40, 65, and 85 km/h (i.e., 25, 40, and 53 mph). For each tested speed, both fully loaded (153 kN or 34.4 kip per bearing) and unloaded (26 kN or 5.85 kip per bearing) railcar conditions were imposed on the selected bearings. These unloaded and loaded conditions will be represented as 17% and 100% load, respectively. The defective bearings were strategically placed on the SBT axle, allowing the defect to be on the outboard position. By doing so, the defect was adjacent to the condition monitoring module as seen in Figure 17, creating a worst-case scenario for the device. If the Boomerang can detect the wheel impact even under these conditions, then its functionality can be further validated. To mitigate component deterioration in the impact mechanism, only ten maximum g data points were collected for each impact condition. The average of the ten data points was then used to produce the figures and tables in Sections 4.2, 4.3, and 4.4. As field operations are transient, testing was performed without waiting for the SBT to reach steady-state conditions. In addition, Accelerometer 2 of the Boomerang was set to its 100g setting as a concurrent field test was being conducted with this variation. The 100g setting would also allow for a more suitable comparison with Accelerometer 1.

4.2 Laboratory Experiment 244: Wheel Impact Detection with a Control Bearing

In Experiment 244, a class F control (healthy, defect-free) bearing was used to investigate whether the Boomerang prototype could detect high wheel impacts while a bearing was operating with healthy components. Using the collected data from this experiment, the average maximum g output of both Boomerang accelerometers (A1 & A2) was calculated and is displayed in Table 11. Using these values, Figure 34 and Figure 35 were then generated to graphically represent the average maximum g response by the Boomerang for unloaded and fully loaded railcar conditions, respectively.

Table 11. Experiment 244 Boomerang Accelerometer 1 (A1) and Accelerometer 2 (A2) impact (I) and no-impact (NI) average maximum acceleration [g] results – control (healthy) bearing

Speed [km/h] / [mph]	**40 / 25**		**65 / 40**		**85 / 53**	
Railcar Load	17%	100%	17%	100%	17%	100%
A1 – I [g]	98	96	98	94	97	95
A1 – NI [g]	3	3	5	4	7	6
A2 – I [g]	99	81	98	86	99	90
A2 – NI [g]	2	2	3	3	5	4

Both accelerometers demonstrated an evident detection of the 320 kN (72 kip) impacts in terms of maximum g's. After the impact was introduced, both Accelerometer 1 (A1) and Accelerometer (A2) exhibited an average maximum acceleration near the 100g limit for all tested speeds and loads. For A1, the average maximum g output under impacts was about 96g for both loading conditions, while for A2, the average maximum g's registered under impacts was roughly 92g. On the other hand, under no-impact conditions, the highest registered maximum g output was 7g at 85 km/h and 17% load by A1. The gradual increase in maximum g's seen for the no-impact condition is a direct result of the increase in operating speed. Comparing the average maximum g output of A1 between all impact and no-impacts results yielded a difference of about 91g. For A2, the average difference between impact and no-impact maximum g's was approximately 89g.

Both accelerometers mostly presented higher maximum g's at an unloaded state (17% load) than under a full load (100% load). Furthermore, at 17% load, the maximum g values for A1 and A2 accelerometers neighbored each other with a difference of about ±2g. This 2g offset was also present in the no-impact results of each tested speed and load condition. Once the bearing was loaded and under impact, the maximum g proximity between sensors changed to a difference of about 9g on average. With that said, A1 registered higher maximum g's than A2 once a full load and impacts were introduced.

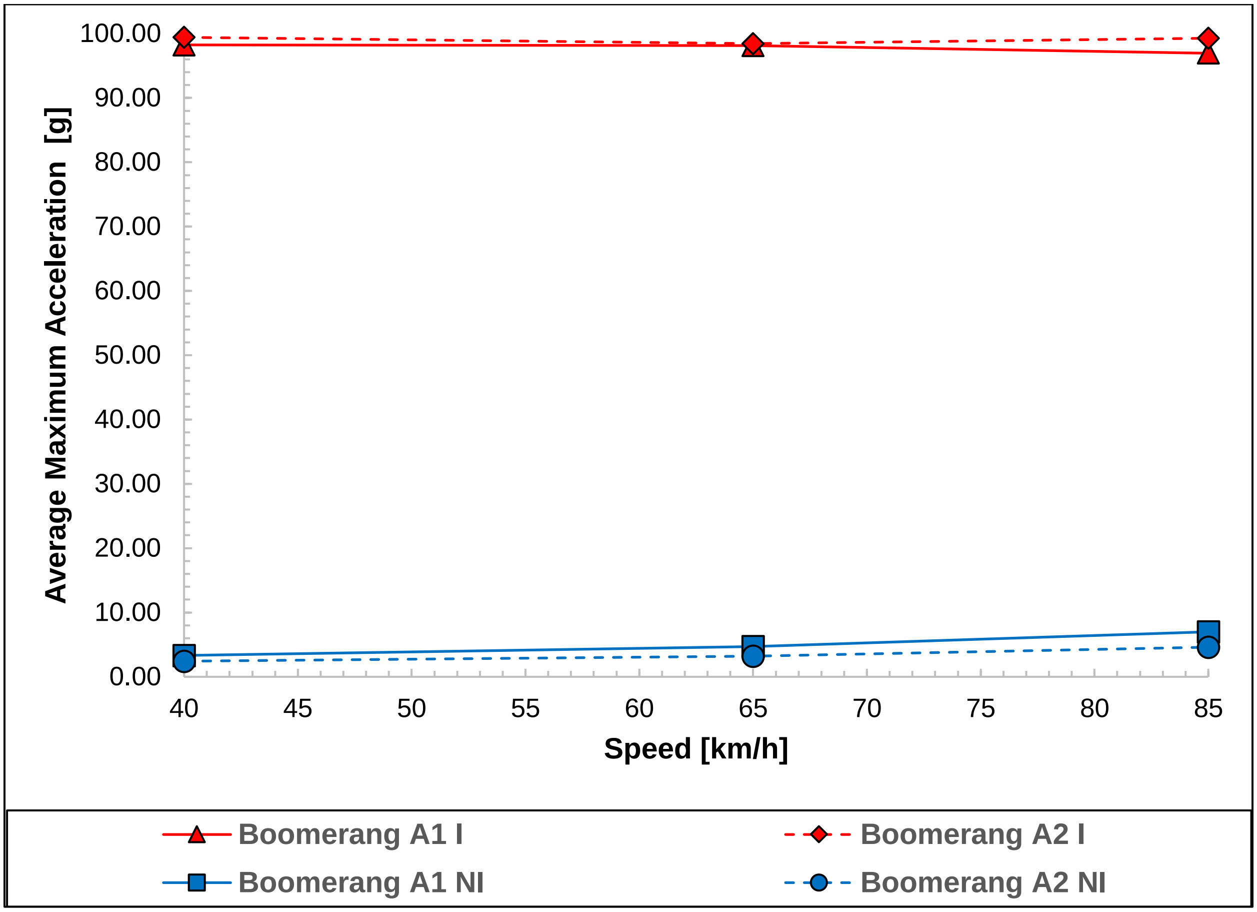

Figure 34. Experiment 244 unloaded control bearing impact (I) and no-impact (NI) Boomerang Accelerometer 1 (A1) and Accelerometer 2 (A2) average maximum [g] results

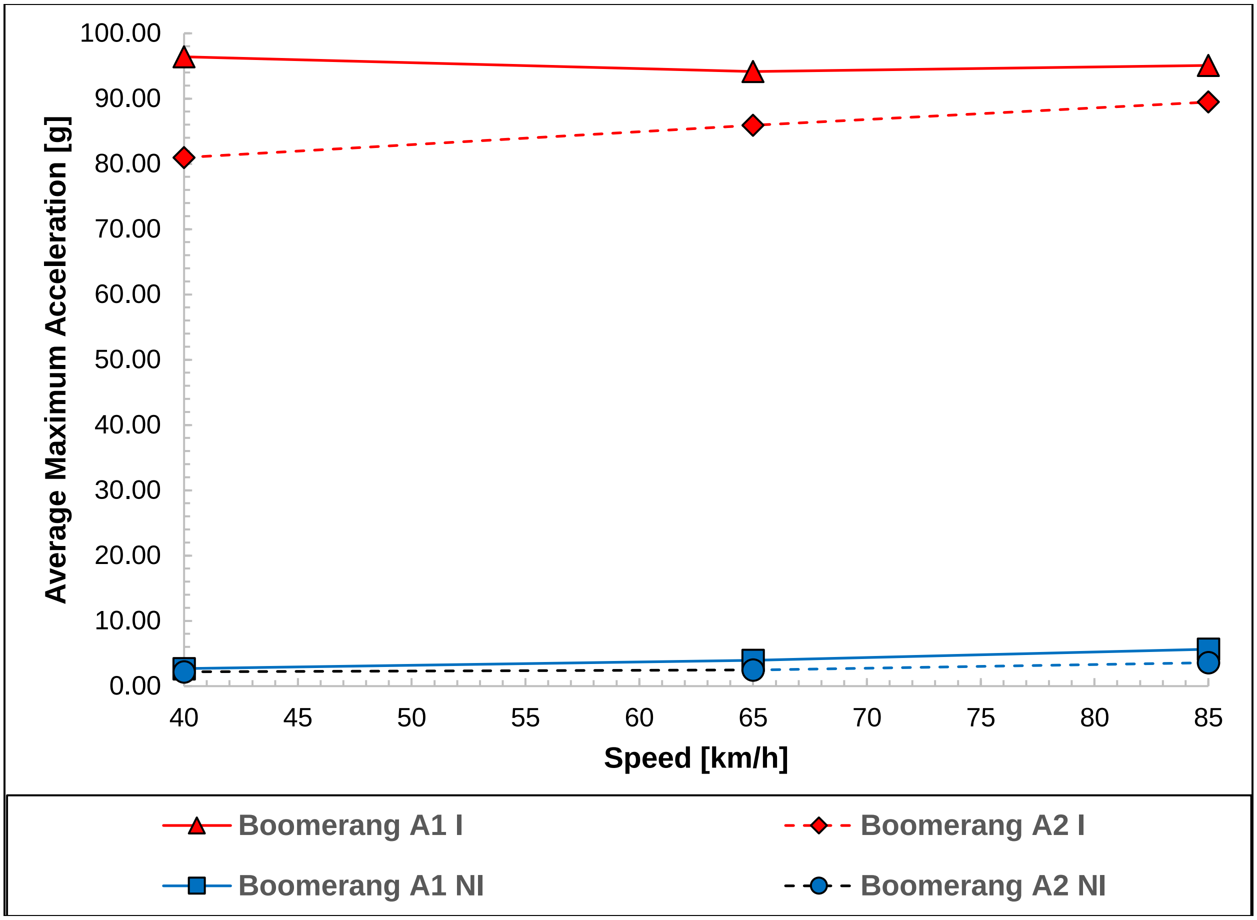

Figure 35. Experiment 244 loaded control bearing impact (I) and no-impact (NI) Boomerang Accelerometer 1 (A1) and Accelerometer 2 (A2) average maximum [g] results

4.3 Laboratory Experiment 245: Wheel Impact Detection with a Cone Defect

In laboratory Experiment 245, a class F bearing with a defective cone area of 11.16 cm^2 (1.73 in^2), pictured in Figure 36, was used to explore whether the Boomerang could detect a high wheel impact while a bearing with a cone defect was in operation. Like Experiment 244, the bearing ran under both loaded and unloaded conditions as well as at the same chosen railcar speeds of 40, 65, and 85 km/h (25, 40, and 53 mph). The data from the Boomerang accelerometers was collected and the average maximum g response was computed. These results are summarized in Table 12. Figure 37 and Figure 38 were then plotted to present a visual perspective on the unloaded and loaded response of the Boomerang, respectively.

Figure 36. Experiment 245 cone containing a raceway spall of 11.16 cm^2 (1.73 in^2)

Table 12. Experiment 245 Boomerang Accelerometer 1 (A1) and Accelerometer 2 (A2) impact (I) and no-impact (NI) average maximum acceleration [g] results – bearing with cone defect

Speed [km/h] / [mph]	**40 / 25**		**65 / 40**		**85 / 53**	
Railcar Load	17%	100%	17%	100%	17%	100%
A1 – I [g]	91	94	95	97	97	95
A1 – NI [g]	12	23	19	29	28	42
A2 – I [g]	67	82	77	75	78	89
A2 – NI [g]	8	39	13	38	19	48

Like the maximum g behavior seen in Section 4.2 (i.e., the control bearing experiment), both Boomerang accelerometers displayed a notable spike in maximum g's after an impact was introduced for all test conditions as seen in Figure 37 and Figure 38. Under impacts, Accelerometer 1 (A1) presented an average maximum g's of 95g while Accelerometer 2 (A2) exhibited an average maximum g's of 78g. All A2 maximum g values, with an impact, were lower than those of A1 by an average difference of about 17g. Since both accelerometers were programmed to acquire vibrations up to 100g, a possible rationale for this maximum g disparity is the lower sampling rate of the A2 accelerometer. Recall that A1 has a significantly higher sampling rate than A2 (i.e., 5,200 Hz versus 780 Hz, respectively). The higher sampling frequency may allow enhanced impact recognition as more data points are being collected per sampling interval, thus increasing the probability of detecting the full vibration signature of the impact.

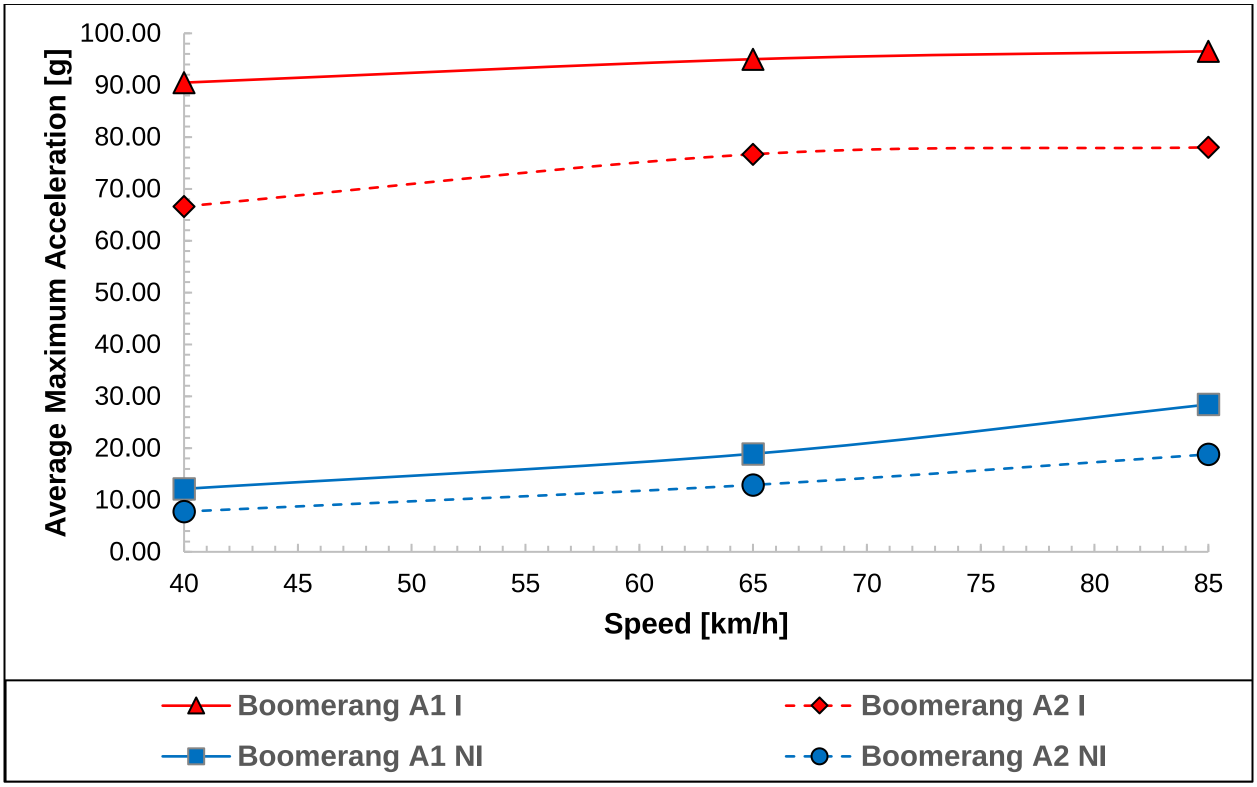

Figure 37. Experiment 245 unloaded bearing with cone spall impact (I) and no-impact (NI) Boomerang Accelerometer 1 (A1) and Accelerometer 2 (A2) average maximum[g] results

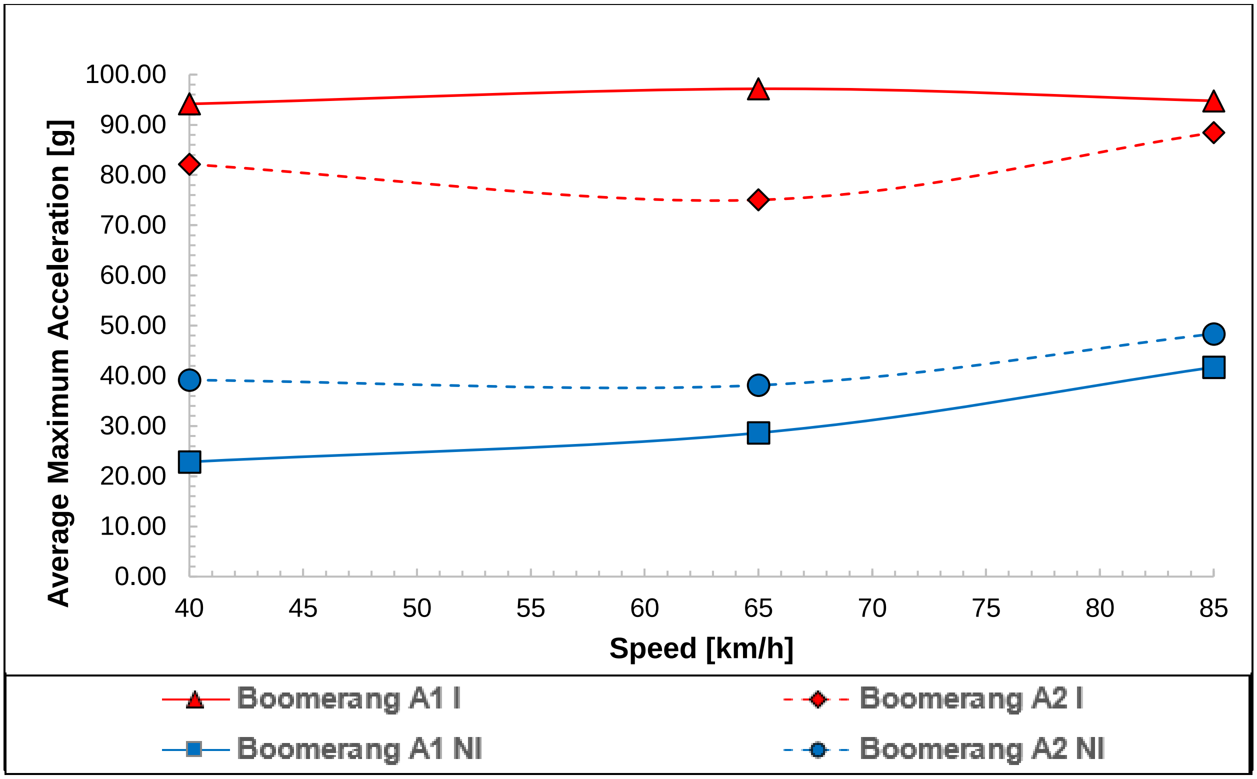

Figure 38. Experiment 245 loaded bearing with cone spall impact (I) and no-impact (NI) Boomerang Accelerometer 1 (A1) and Accelerometer 2 (A2) average maximum [g] results

Further inspection of the no-impact results revealed other trends. A1 exhibited higher maximum g's than A2 under unloaded conditions with an average difference of 6g between accelerometers. However, once a full load was exerted, A2 displayed higher maximum g's than A1 with an average difference of 10g between accelerometers. In comparison to the results of Section 4.2 (i.e., control bearing experiment), both accelerometers registered an increase in no-impact maximum g values. In turn, this caused the maximum g gap between impact and no-impact to decrease. The average maximum g output difference between the impact and no-impact results of A1 and A2 was now around 69g and 50g, respectively, as opposed to the 91g and 89g difference for A1 and A2, respectively, in the control (healthy) bearing results. This discrepancy is likely due to the roller interactions with the spalled raceway which create higher vibration signatures compared to the rollers rotating against the smooth (defect-free) cone raceway of the control bearing. Nevertheless, even though there was an increase in the maximum g values under no-impacts, the Boomerang could still plainly detect the presence of the 72-kip impact.

4.4 Laboratory Experiment 246: Wheel Impact Detection with a Cup Defect

As shown in Figure 39, laboratory Experiment 246 involved impact testing while simultaneously running a class F bearing containing a cup defect of 10.13 cm^2 (1.57 in^2) in area. The purpose of this experiment was to determine whether the Boomerang could detect a high-wheel impact while a bearing with a cup defect was in operation. The cup defect was positioned directly under the full load to amplify the vibrational output of the bearing, thus creating a worst scenario. Table 13 provides the results for all the test conditions described in Section 4.1. The average maximum g output of the Boomerang accelerometers at 17% and 100% applied load are plotted in Figure 40 and Figure 41, respectively.

Figure 39. Experiment 246 cup containing a raceway spall of 10.13 cm^2 (1.57 in^2)

Table 13. Experiment 246 Boomerang Accelerometer 1 (A1) and Accelerometer 2 (A2) impact (I) and no-impact (NI) average maximum acceleration [g] results – bearing with cup defect

Speed [km/h] / [mph]	**40 / 25**		**65 / 40**		**85 / 53**	
Railcar Load	17%	100%	17%	100%	17%	100%
A1 – I [g]	92	96	87	91	95	90
A1 – NI [g]	15	35	19	46	40	55
A2 – I [g]	62	88	55	93	71	99
A2 – NI [g]	9	70	25	78	51	97

In contrast to the maximum g behavior displayed by the Boomerang in Sections 4.2 (i.e., control bearing experiment) and 4.3 (i.e., defective cone experiment), where both accelerometers were able to detect the 320 kN (72 kip) impact at all speed and load combinations, Experiment 246 revealed an opposing outcome.

Observing the unloaded results of Figure 40, both Accelerometer 1 (A1) and Accelerometer 2 (A2) were able to detect the simulated high wheel impact, albeit with A1 having better reliability. The average maximum g output with impacts was 91g and 63g for A1 and A2, respectively. On average, A1 displayed an average maximum g difference of 67g between impact and no-impact, while A2 exhibited a difference of only 34g. However, it can be observed that as the test speed increased, the maximum g output between impact and no-impact started to converge for A2.

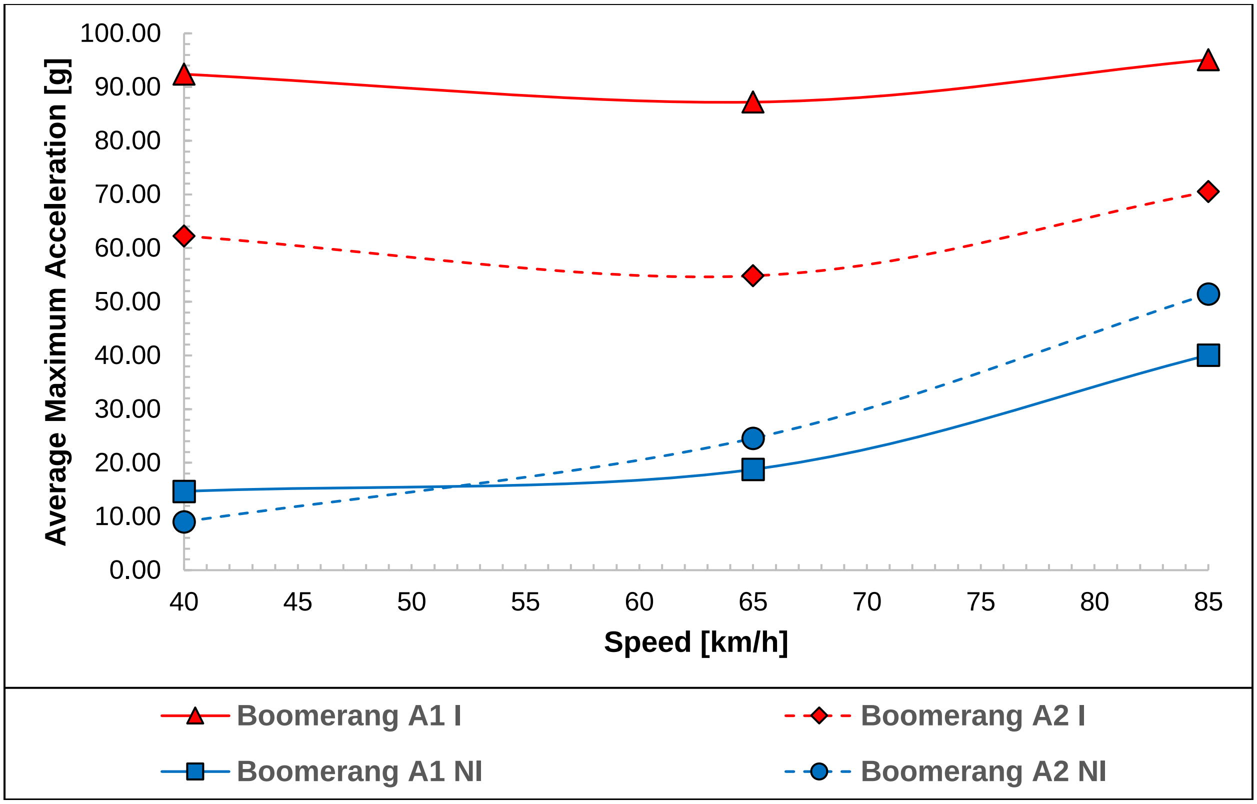

Figure 40. Experiment 246 unloaded bearing with cup spall impact (I) and no-impact (NI) Boomerang Accelerometer 1 (A1) and Accelerometer 2 (A2) average maximum [g] results

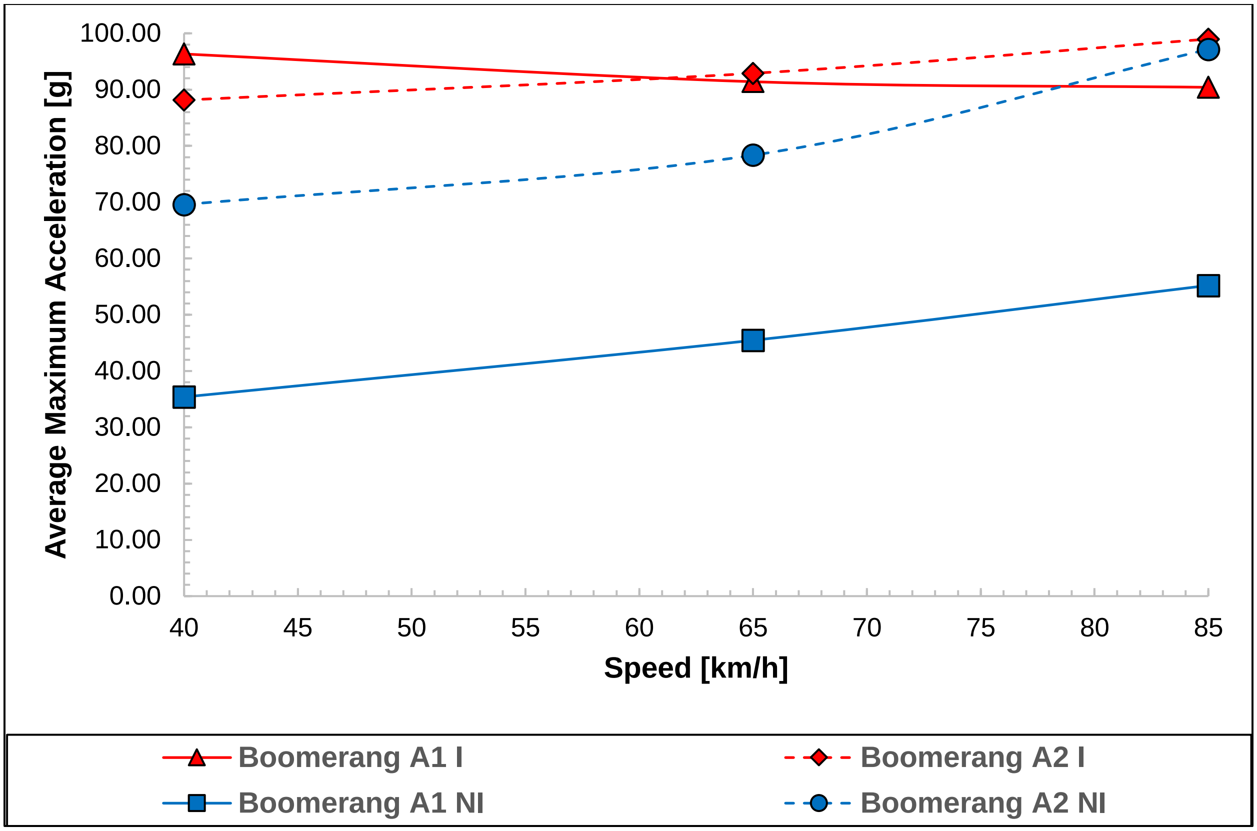

Figure 41. Experiment 246 loaded bearing with cup spall impact (I) and no-impact (NI) Boomerang Accelerometer 1 (A1) and Accelerometer 2 (A2) average maximum [g] results

For the fully loaded tests, the detectability of the 72-kip impact, while a bearing with a cup spall was in operation, was compromised, especially for the A2 accelerometer. In fact, once the highest test speed of 85 km/h (53 mph) was employed, the impact and no-impact maximum g data almost completely converged for the A2 accelerometer, as seen in Figure 41 and Table 13. Although both accelerometers were able to detect the 72-kip impact for the lower test speeds, A2 was already demonstrating signs of susceptibility towards the mechanical noise being generated by the cup spall. The average difference between impact and no-impact maximum g for A2 was about 11g with the difference at the highest tested speed diminishing to a meager 2g. Thus, the A2 accelerometer was incapable of effectively diagnosing whether the maximum g output was representative of a high wheel impact or a defective bearing. On the other hand, the A1 accelerometer demonstrated a better capability of recognizing the wheel impacts with an average difference of 47g between impact and no-impact results, and a 35g minimum difference at the highest speed tested.

The converging behavior between impact and no-impact maximum g data for the A2 accelerometer, seen in both the loaded and unloaded (to a lesser extent) results which was not the case in the cone defect experiment (i.e., Experiment 245), can be explained by the direct loading condition imposed on the cup defect. Unlike the cone defect which cycles in and out of the load zone, the cup defect is in constant engagement with the applied load, intensifying vibration emissions as the rollers pass through the defect area. Increases in speed or load tend to amplify the vibration levels within the bearing, which explains why the maximum g values for the impact and no-impact conditions start to converge. Furthermore, the Boomerang was also positioned in direct alignment with the defective region of the cup, thus increasing the susceptibility of the device to the test conditions. Note that the A1 accelerometer was still able to distinguish between the defective bearing with a cup spall and the wheel impact even at these operating conditions.

CHAPTER V

SUPPLEMENTAL TESTING USING UTCRS WIRELESS MODULE

When in transit, the components of a railcar bogie inherently generate mechanical noise. Service environments, operating conditions, and accrued component wear are some factors that can increase the output of this byproduct. In turn, the presence of these aftereffects can interfere with signal clarity by increasing the noise to signal ratio, thus, affecting the performance of signal processing devices (i.e., sensor devices). Because the HUM Boomerang (a signal processing device) is destined to be a component of these rail vehicles, it is crucial to explore feasible solutions that can neutralize aliasing and other possible signal susceptibilities that the device may sustain in field service. An active signal processing practice at the University Transportation for Railway Safety (UTCRS) has been the use of electronic filters, rendering effective noise suppression. Therefore, this chapter showcases the possible integration of an electronic filter in the HUM Boomerang by featuring results obtained from a laboratory assessment. Specifically, since the electronic hardware of the tested Boomerang model was tailored to function as is, any alterations within the circuitry could cause the device to malfunction. Incorporating a filter in the module would require HUM to redesign and manufacture a new version of the Boomerang device, entailing an unknown lead time that could potentially affect the testing schedule. As the UTCRS wireless module (UWM) utilizes the same accelerometer as the HUM Boomerang (i.e., Accelerometer 1) and possesses manageable component interchangeability, an 8th order elliptical filter with a high frequency cut-off of 2.1 kHz was integrated into the UWM and systematically tested Additionally, aside from demonstrating the effects of an added filter on high wheel impact detection and noise cancellation, the ability of the UWM in detecting bearing defect type, even with the introduction of an impact, was also evaluated by using the UTCRS Level 2 algorithm. This effort would provide additional understanding of simultaneous dynamic bearing and wheel signal interactions and facilitate a future feature in the HUM Boomerang that would allow bearing defect type identification in terms of percentage-based confidence levels.

5.1 Filter Testing Methodology

Filtered and unfiltered wireless module impact tests were conducted simultaneously within Experiments 244, 245, and 246 seen in Sections 4.2, 4.3, and 4.4, respectively. Therefore, the same class F bearings, single bearing test rig (SBT), impact system setup, and operating conditions were used as described in those sections. Namely, the testing conditions included 320 kN (72 kip) impact and no-impact trials under dynamic bearing operations of 40, 65, and 85 km/h (i.e., 25, 40, and 53 mph) at 17% and 100% load. Again, 17% load represents an unloaded (empty) railcar (i.e., 26 kN or 5.85 kip per bearing) while 100% load represents a fully loaded railcar (i.e., 153 kN or 34.4 kip per bearing). It is also important to state that, as the main goal of this thesis was to assess the high wheel impact detection efficacy of the HUM Boomerang and not the UTCRS wireless module (UWM), the filtered sensor was affixed angularly on the bearing adapter as seen in Figure 17. This allowed the HUM Boomerang to be secured vertically on the bearing adapter, adopting the same mounting position as in a field setup. Since this was a supplemental test, performing an additional experiment with a vertical orientation of the filtered sensor could impose unnecessary and unwanted wear on the components of the impact tester.

Two data acquisition procedures were enacted for this test. To adequately compare filter response for all bearing conditions, the first procedure involved using code (a) defined in Section 3.2.2. Ten maximum acceleration [g] data points were collected for both impact and no-impact conditions under both filtered and unfiltered UWM settings. An average maximum g calculation was performed after the results were obtained and used to delineate the UWM response for each tested condition as represented in the figures and tables shown in Sections 5.2, 5.3, and 5.4.

The second procedure was conducted only for the tests involving the bearings with a defective cone and cup. Four instances of one second raw voltage data were collected for both filter settings using code (b) defined in Section 3.2.2. This last procedure would enable the execution of the UTCRS Level 2 analysis algorithm in MATLAB® to determine whether bearing defect type could be recognized despite the elevated noise and vibration levels generated by the high-wheel impacts. A Level 2 analysis was not performed on the control bearing experiment as no defect was present. As a note, UTCRS defect classification protocol for the Level 2 analysis requires at least a 50% confidence level to indicate a valid defect type designation.

5.2 Laboratory Experiment 244: Filter Impact Test with a Control Bearing

The data on Table 14 demonstrates the average maximum acceleration [g] response by the UTCRS wireless module (UWM) with and without a filter on the control (defect-free) bearing test of Experiment 244. Using the data from this table, Figure 42 and Figure 43 were plotted to give the empty (17%) and fully loaded (100%) railcar results, respectively.

For each tested speed and load combination, the UWM was able to detect the 320 kN (72 kip) impacts under both filtered and unfiltered settings in terms of maximum g output. However, the filter did alter the maximum g magnitude that was collected by the UWM as filtered maximum g values were lower than the unfiltered throughout the extent of the experiment.

Unfiltered results for both loading conditions indicated that the UWM was saturating at the 65 km/h (40 mph) and 85 km/h (53 mph) test speeds as the maximum operating range of 123g was reached while, on average, the filtered data remained consistently under that threshold. The effect of the filter on the maximum g output of the wireless module was subtle for tests conducted under a no-impact setting. On average, the maximum g difference between the filtered and unfiltered no-impact condition was roughly 3g. However, the effect of the filter on the maximum g output was more pronounced when impacts were introduced. Bearing loading conditions were also a significant factor in the filtered response of the UWM when impacts were introduced.

Table 14. Experiment 244 UTCRS wireless module filter (F) and no filter (NF) average maximum [g] results for impact (I) and no-impact (NI) – control (healthy) bearing

Speed [km/h] / [mph]	**40 / 25**		**65 / 40**		**85 / 53**	
Railcar Load	17%	100%	17%	100%	17%	100%
F – I [g]	81	41	106	54	102	55
F – NI [g]	2	2	4	3	7	6
NF – I [g]	112	99	123	122	123	122
NF – NI [g]	3	3	7	7	11	12

For the unloaded impact test results, the average maximum g response with a filter was 96g while the average maximum g response without a filter was about 119g. Comparing the maximum g behavior between impact and no-impact, the average difference was 92g and 112g for the filtered and unfiltered conditions, respectively. This difference is highlighted by the data plotted in Figure 42. The gradual increase in maximum g output seen in the unloaded no-impact condition data is directly related to the increase in operating speed.

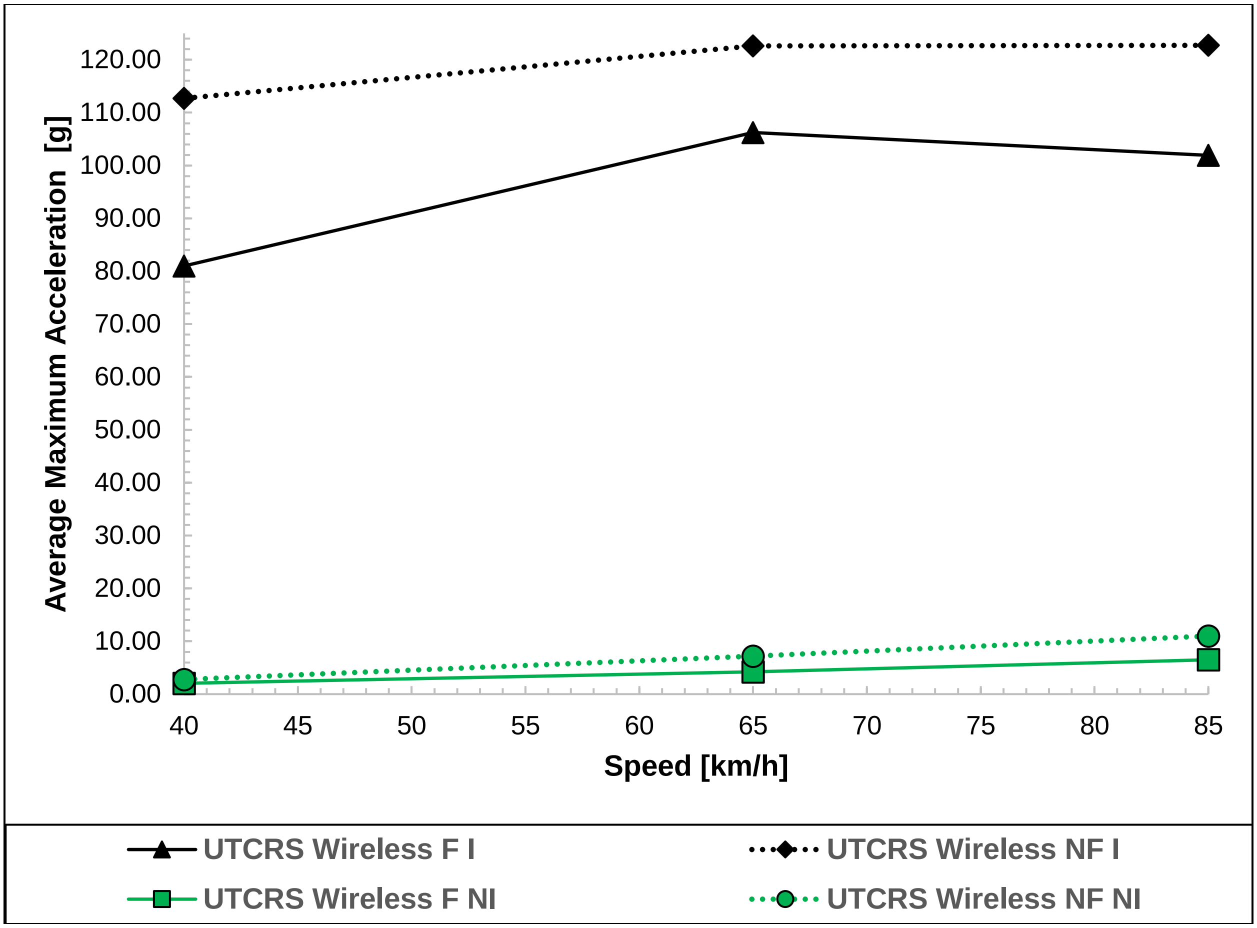

Figure 42. Experiment 244 unloaded control bearing impact (I) and no-impact (NI) UTCRS wireless module filter (F) and no filter (NF) average maximum [g] results

The fully loaded railcar impact results demonstrated a higher sensibility towards the filter compared to the unloaded impact results as seen in Table 14 and by comparing Figure 42 and Figure 43. Under impacts, the filtered average maximum g output was now 50g compared to the 96g of the unloaded results. Without a filter, the average maximum g response was 114g, remaining close to the average response of 119g for the unloaded results. Although the loaded impact results were more affected by the filter, the difference between impact and no-impact was still evident. On average, at 100% load, the difference between impacts and no-impacts was 46g for the filtered setting. Without a filter, the average maximum g difference between impact and no-impact conditions was 107g. Like the unloaded results, a gradual increase in maximum g can be seen for the no-impact data indicative of an increase in test speed.

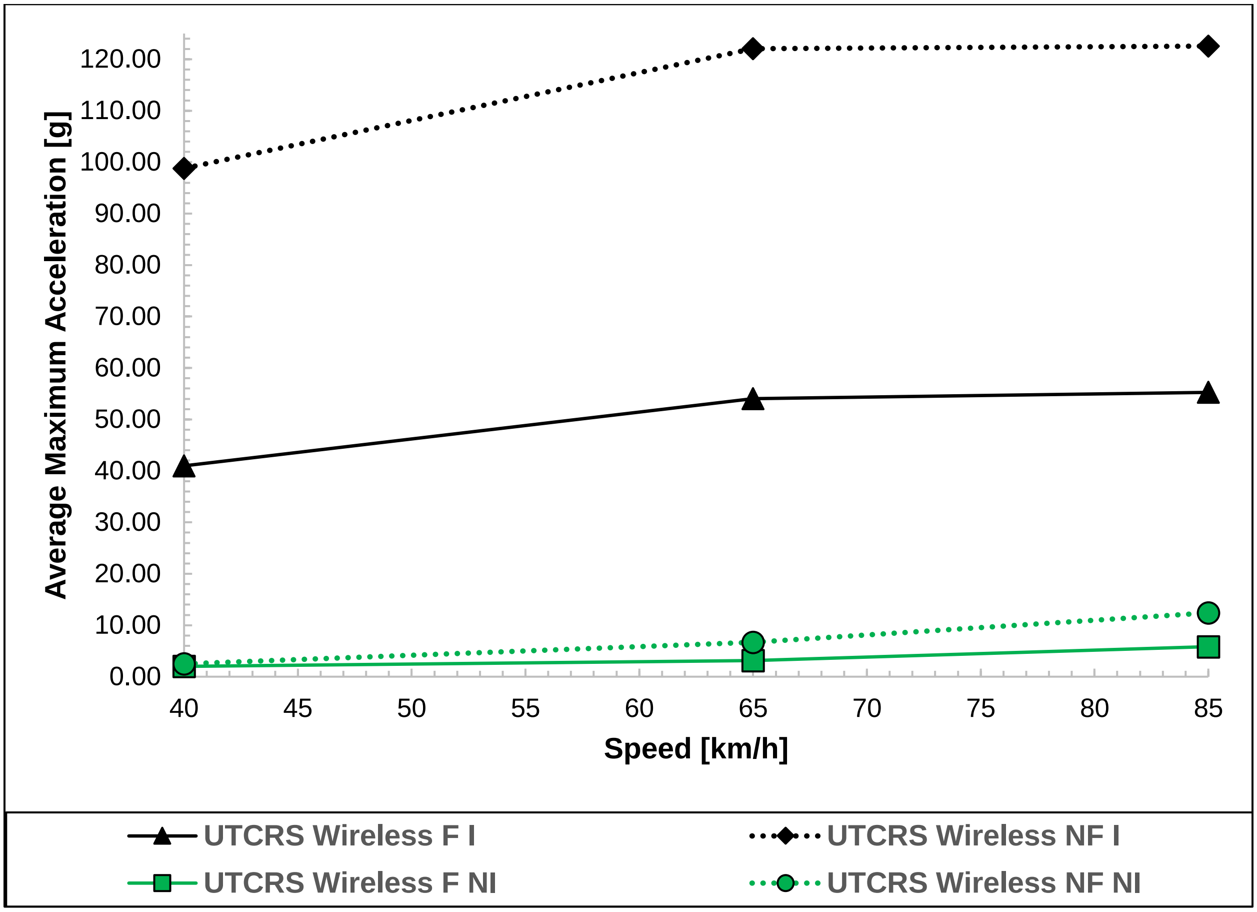

Figure 43. Experiment 244 loaded control bearing impact (I) and no-impact (NI) UTCRS wireless module filter (F) and no filter (NF) average maximum [g] results

5.3 Laboratory Experiment 245: Filter Impact Testing with a Cone Defect

The average maximum g output for the filtered and unfiltered impact data of Experiment 245 (i.e., cone spall test) is displayed in Table 15. Like the control bearing experiment results of Section 5.2, the filtered test results of this experiment demonstrated lower maximum g values than the unfiltered results for all tested conditions. The applied impacts also caused the accelerometer to exhibit signs of saturation as the maximum g values acquired through the unfiltered setting of the UWM neighbored the 123g maximum operating range.

Table 15. Experiment 245 UTCRS wireless module filter (F) and no filter (NF) average maximum acceleration [g] results for impact (I) and no-impact (NI) – bearing with cone defect

Speed [km/h] / [mph]	**40 / 25**		**65 / 40**		**85 / 53**	
Railcar Load	17%	100%	17%	100%	17%	100%
F – I [g]	83	46	84	50	99	72
F – NI [g]	6	10	12	21	19	51
NF – I [g]	106	115	116	121	122	122
NF – NI [g]	11	57	23	63	26	87

The average maximum g output results for the 17% load condition (empty railcar) are plotted in Figure 44. Increases in test speed caused a decrease in the maximum g gap between the impact and no-impact data sets, mimicking the behavior seen in Figure 37 of Section 4.3 (i.e., Boomerang and cone spall test results). Although this effect was present, the difference between an impact and no-impact condition could still be appreciated. In reference to Table 15, the average maximum g output by the UWM, under the influence of impacts, was 89g and 115g between the filter and no filter setting, respectively. Correspondingly, the impact and no-impact maximum g difference was 77g and 95g for the filtered and unfiltered results, respectively.

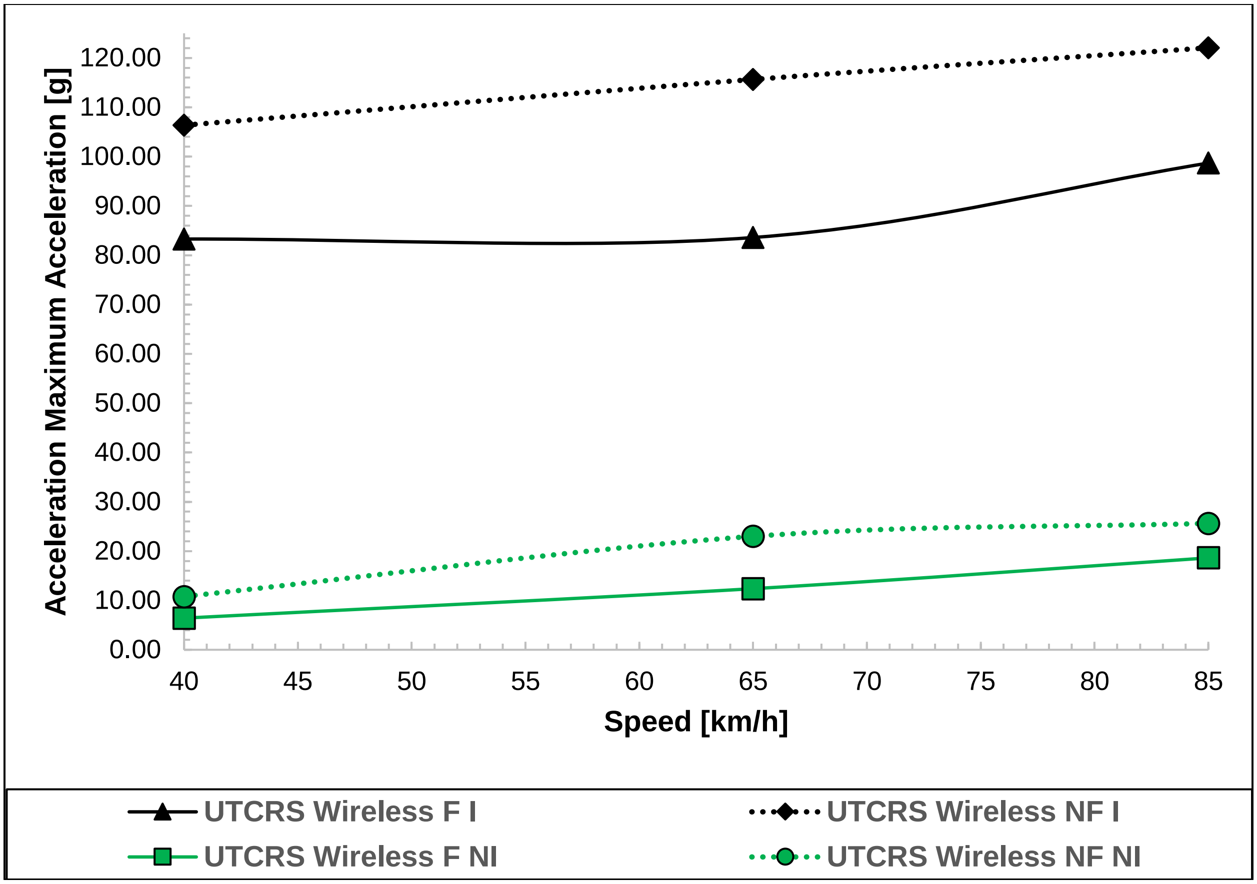

Figure 44. Experiment 245 unloaded bearing with cone spall impact (I) and no-impact (NI) UTCRS wireless module filter (F) and no filter (NF) average maximum [g] results

Figure 45 presents the fully loaded test results. Like the behavior seen in the fully loaded control bearing experiment results of Section 5.2, the filter also caused the maximum g output of the UWM to be lower than that of the unloaded results when an impact was introduced. On average, the maximum g output read by the UWM, under the influence of impacts, was 56g and 119g for the filtered and unfiltered results, respectively. Correspondingly, the average difference between impact and no-impacts was about 29g and 50g between filtered and unfiltered results, respectively. The increase in load also had a more noticeable effect on the UWM maximum g output compared to the unloaded results. As the operating speed increased, the maximum g difference between impact and no-impact conditions decreased, causing the maximum g values to converge for both filter settings until the final test speed of 85 km/h (53 mph) was executed.

This behavior can be attributed to the cone spall in the operating bearing. As previously mentioned in Section 4.3, the increase in speed and load trigger higher vibrational output from the spalled raceway and the rollers interaction. Nonetheless, regardless of filter setting or loading condition, the UWM was still able to register maximum g values that permitted high wheel impact and no-impact conditions to be distinguished. Yet, the filter provided a more collected maximum g output.

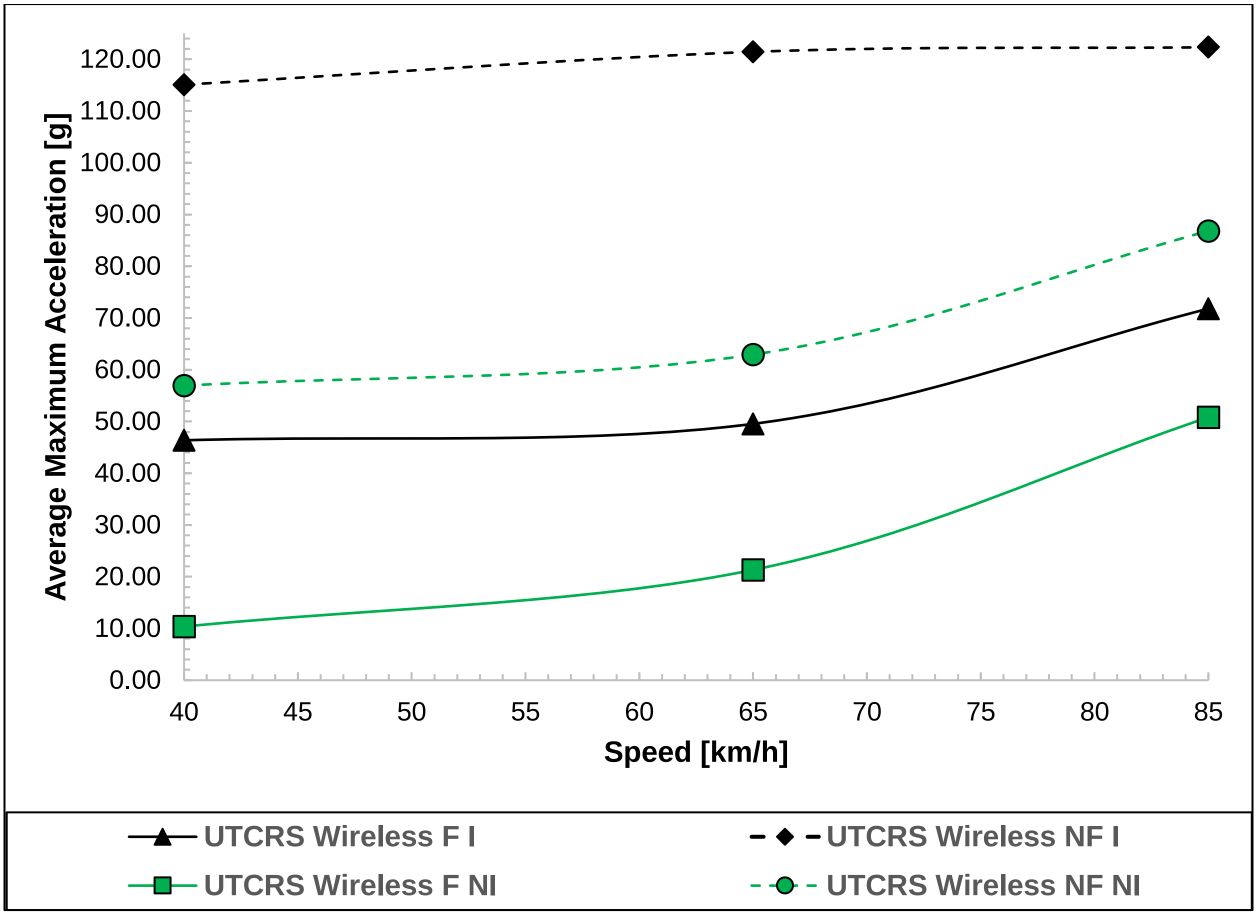

Figure 45. Experiment 245 loaded bearing with cone spall impact (I) and no-impact (NI) UTCRS wireless module filter (F) and no filter (NF) average maximum [g] results

Table 16 and Table 17 present the Level 2 analysis results for Experiment 245 for both filtered and unfiltered impact tests, respectively. With filtered impacts, the cone defect was recognized 5 out of the 6 tested railcar conditions while the algorithm accurately detected the defect type 4 out of 6 instances for the unfiltered impacts. The 5 asserted cases displayed an average confidence level of 91%. For the unfiltered results, the 4 affirmed cases presented an average confidence level of 71%. These results demonstrate that despite a high-wheel impact being present, the algorithm can still accurately and reliably determine the bearing defect type. In addition, the functionality of the filter was validated as it allowed for increased confidence levels and accurate defect type detections by the developed algorithm.

Table 16. Experiment 245 Level 2 analysis results using UTCRS Wireless Module (UWM) impact data with active filter

Filter						
Speed [km/h] / [mph]	**40 / 25**		**65 / 40**		**85 / 53**	
Railcar Load	17 %	100%	17%	100%	17%	100%
Algorithm Confidence Level [%]	**92**	**75**	**90**	63	**98**	**98**
Defect Type	Cone	Cone	Cone	Cup	Cone	Cone

Table 17. Experiment 245 Level 2 analysis results using UTCRS Wireless Module (UWM) impact data without active filter

No Filter						
Speed [km/h] / [mph]	**40 / 25**		**65 / 40**		**85 / 53**	
Railcar Load	17 %	100%	17%	100%	17%	100%
Algorithm Confidence Level [%]	79	**71**	**51**	**90**	**67**	76
Defect Type	Cup	Cone	Cone	Cone	Cone	Cup

5.4 Laboratory Experiment 246: Filter Impact with a Cup Defect

The average filtered and unfiltered maximum g response by the UWM for Experiment 246 (i.e., cup spall test) are provided in Table 18. Like the control bearing (Experiment 244) and the defective cone bearing (Experiment 245) test results, the filter was able to minimize mechanical noise in terms of maximum g, maintaining all filtered maximum g values lower than the unfiltered values for each tested condition. The UWM also presented signs of saturation as maximum g values near the 123g threshold operating range were met when unfiltered impacts at the 100% load condition were being conducted.

Table 18. Experiment 246 UTCRS wireless module filter (F) and no filter (NF) average maximum acceleration [g] results for impact (I) and no-impact (NI) – bearing with cup defect

Speed [km/h] / [mph]	**40 / 25**		**65 / 40**		**85 / 53**	
Railcar Load	17%	100%	17%	100%	17%	100%
F – I [g]	43	51	52	61	64	62
F – NI [g]	4	5	7	9	11	14
NF – I [g]	99	122	104	122	112	121
NF – NI [g]	19	66	41	111	71	115

Figure 46 presents the unloaded test results for this experiment. As shown in the graph, both filter settings were able to distinguish the 320 kN (72 kip) impacts for all tested speeds. With impacts, the average maximum g output by the UWM with an active filter was around 53g. In contrast, the unfiltered UWM setting produced an average maximum acceleration of about 105g. Without impacts, the average maximum g output by the UWM was 7g and 44g for filtered and unfiltered data, respectively. These values correspond to an impact condition difference of 46g and 61g between filtered and unfiltered data, respectively, at 17% load (i.e., empty railcar load). Furthermore, for the unfiltered test results, it can also be observed how the maximum g difference between impact and no-impact progressively lessens as operating speed increases. On the other hand, the maximum g difference for the filtered results exhibited a slight increase with the operating speed.

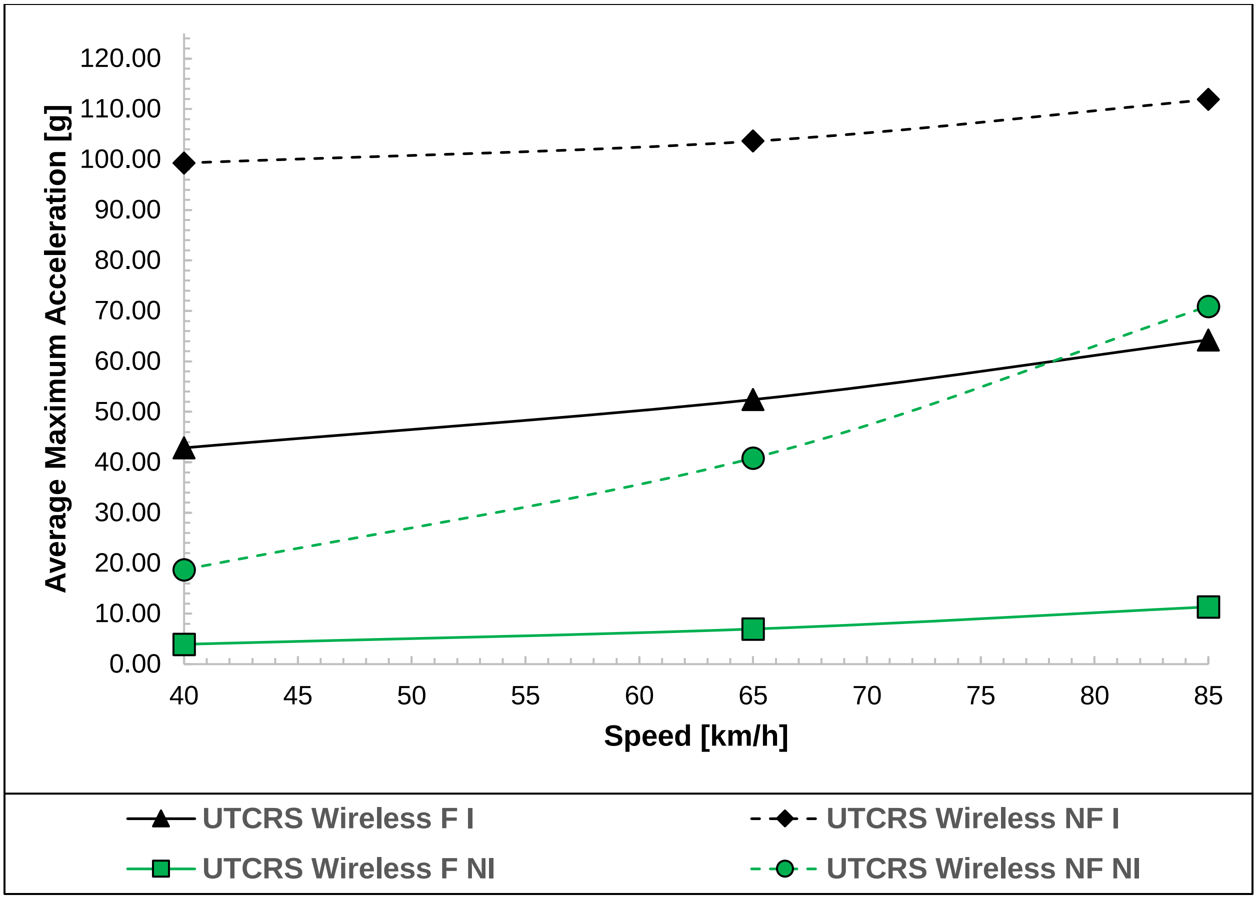

Figure 46. Experiment 245 unloaded bearing with cup spall impact (I) and no-impact (NI) UTCRS wireless module filter (F) and no filter (NF) average maximum [g] results

The fully loaded test results, represented by Figure 47, exhibit different trends than those of the unloaded results. Although the filter helped maintain a consistent difference between the maximum g values for the impact and no-impact results, the unfiltered results displayed similar behavior to the Boomerang results for the defective cup test discussed in Section 4.4. That is, for the unfiltered results of the final two test speeds, the UWM could not distinguish the difference between the 320 kN (72 kip) impact and the cup spall in terms of maximum g. For the filtered impact results, the average maximum g output was about 58g while all the unfiltered impact results remained saturated at 122g. Now, without an impact, the average maximum g output was around 9g and 97g with and without an active filter, respectively. Using these results to calculate the difference between an impact and no-impact maximum g response still yields a significant maximum g difference of about 49g for the filtered results. However, for the unfiltered data, the relative proximity in maximum g between the impact and no-impact results at 65 km/h (40 mph) and 85 km/h (53 mph) is concerning, equaling to differences of 11g and 6g, respectively. Hence, these results suggest that for bearings containing relatively large cup spalls, the filter feature is crucial to being able to differentiate between a high wheel impact and the defective bearing. The Level 2 analysis results for this experiment support this latter conclusion.

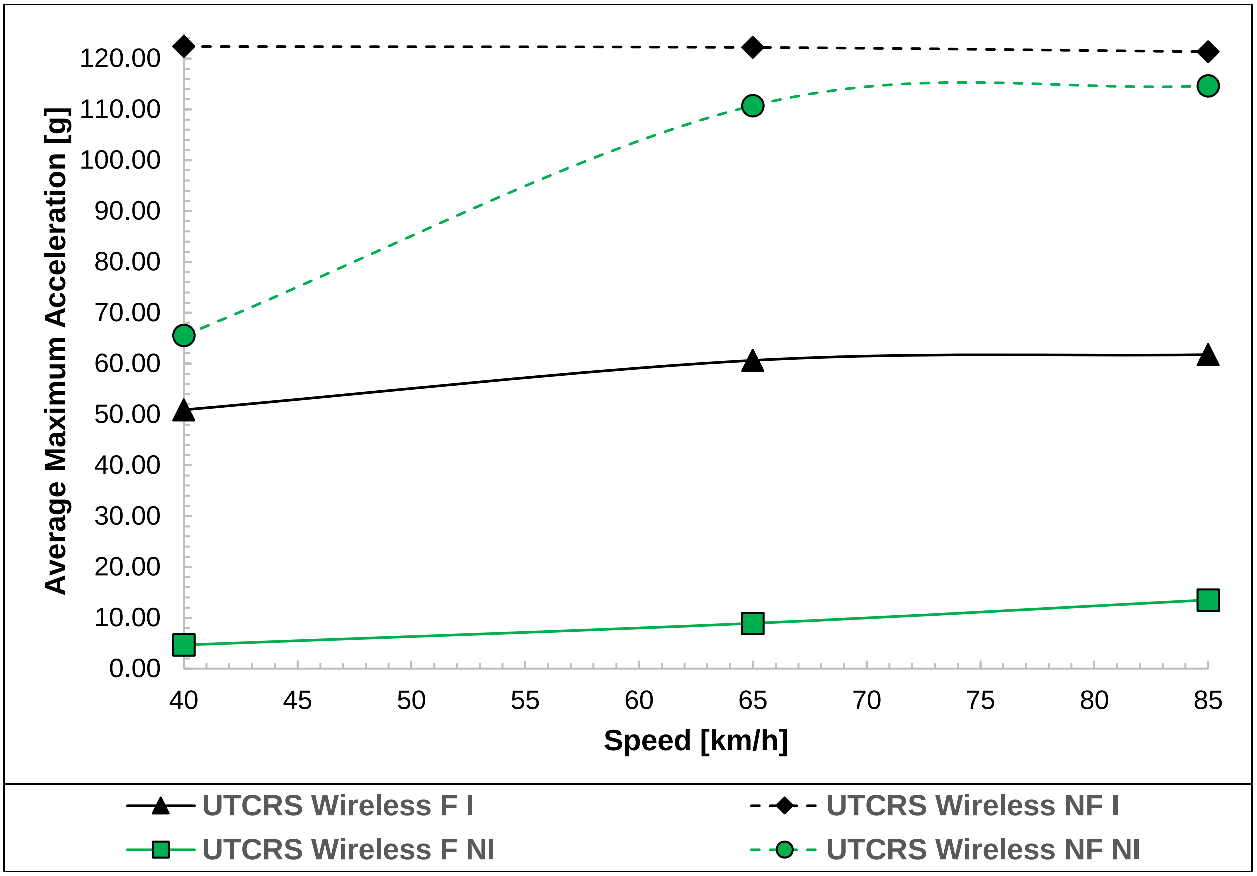

Figure 47. Experiment 246 loaded bearing with cup spall impact (I) and no-impact (NI) UTCRS wireless module filter (F) and no filter (NF) average maximum [g] results

The Level 2 analysis results for the filtered and unfiltered impact tests of Experiment 246 are shown in Table 19 and Table 20, respectively. Out of the six tested railcar operating conditions, the algorithm correctly identified the cup defect four times for the filtered data with an average confidence level of 80%. More importantly, the algorithm was able to identify the cup defect in all the fully loaded railcar operating conditions with a confidence level of at least 83%. However, without a filter, the algorithm was unable to distinguish the defect in each of the tested operating conditions. Specifically, the algorithm indicated a cone defect in all six tested scenarios. Therefore, the filter feature in the wireless sensor modules proves to be essential in providing accurate and reliable defect type detection in the presence of high wheel impacts.

Table 19. Experiment 246 Level 2 analysis results using UTCRS Wireless Module (UWM) impact data with an active filter

Filter						
Speed [km/h] / [mph]	40 / 25		65 / 40		85 / 53	
Railcar Load	17 %	100%	17%	100%	17%	100%
Algorithm Confidence Level [%]	86	**83**	72	**86**	**53**	**98**
Defect Type	Cone	Cup	Cone	Cup	Cup	Cup

Table 20. Experiment 246 Level 2 analysis using UTCRS Wireless Module (UWM) impact data without an active filter

No Filter						
Speed [km/h] / [mph]	40 / 25		65 / 40		85 / 53	
Railcar Load	17 %	100%	17%	100%	17%	100%
Algorithm Confidence Level [%]	80	79	61	80	51	82
Defect Type	Cone	Cone	Cone	Cone	Cone	Cone

CHAPTER VI

PILOT FIELD TEST RESULTS

The following chapter presents the maximum acceleration [g] data collected over a two-month period for the pilot field test conducted on an active service route referenced in Section 3.5. Pre- and post-changeout maximum g indices for the removed healthy axles (Axle 1 and 2) and the defective axle (Axle 2) are provided to allow for a direct comparison between typical and atypical wheel condition maximum g outputs.

6.1 Field Test Data Analysis Methodology

To support the results and characterize certain maximum g ranges, a preliminary nominal operation maximum g threshold and experimentally established thresholds were introduced. The first limit, at 20g, was introduced in relation to the dominant maximum acceleration behavior seen in the pre- and post-changeout data of the removed healthy axles. That is, within both healthy axle data sets, the maximum g levels remained generally under 20g for all operating speeds. At 55g, the second threshold is the equivalent of a 133 kN (30 kip) wheel impact determined from the experimental data referenced in Table 10 of Section 3.4. As this limit is half the 267 kN (60 kip) threshold at which the FRA has advised maintenance for wheels, it prompts that any wheels operating within the 20g and 55g boundaries should be observed closer but are of low concern. Lastly, a 267 kN (60 kip) limit was set at 100g. This maximum g to kip threshold can be referenced back to Table 10 in Section 3.4. As previously discussed, a wheel presenting this impact is deemed worthy of a maintenance advisory. Hence, any wheels displaying maximum g values within the 133 kN (30 kip) and 267 kN (60 kip) limits enter a state of high concern where railcar owners should attentively monitor their vehicles for any 100g indications. Once at 100g, railcar owners should follow the appropriate measures dictated by the FRA.

Although these implemented thresholds are established from conducted experiments, they are not an official wheel monitoring standard. Nonetheless, their role sets the foundation for understanding the behavior of normal and abnormal wheel dynamics. With continued research efforts, these thresholds can be optimized and additional maximum g to kip indices can be created to improve wheel health classifications for the HUM Boomerang condition monitoring device.

6.2 Field Data Analysis

Figure 48 and Figure 49 represent the collective maximum g behavior for the healthy axles (Axles 1 and 2) before and after their wheelset interchange, respectively. Despite the occasional outlier, which could be the result of bad track segments, there were no significant deviations in the maximum g output caused by the changeout operation, establishing that the original wheelsets were indeed performing under nominal conditions. The pre- and post-changeout predominant maximum g values that fall within the 20g threshold further justify the introduction of the preliminary nominal wheel operation threshold.

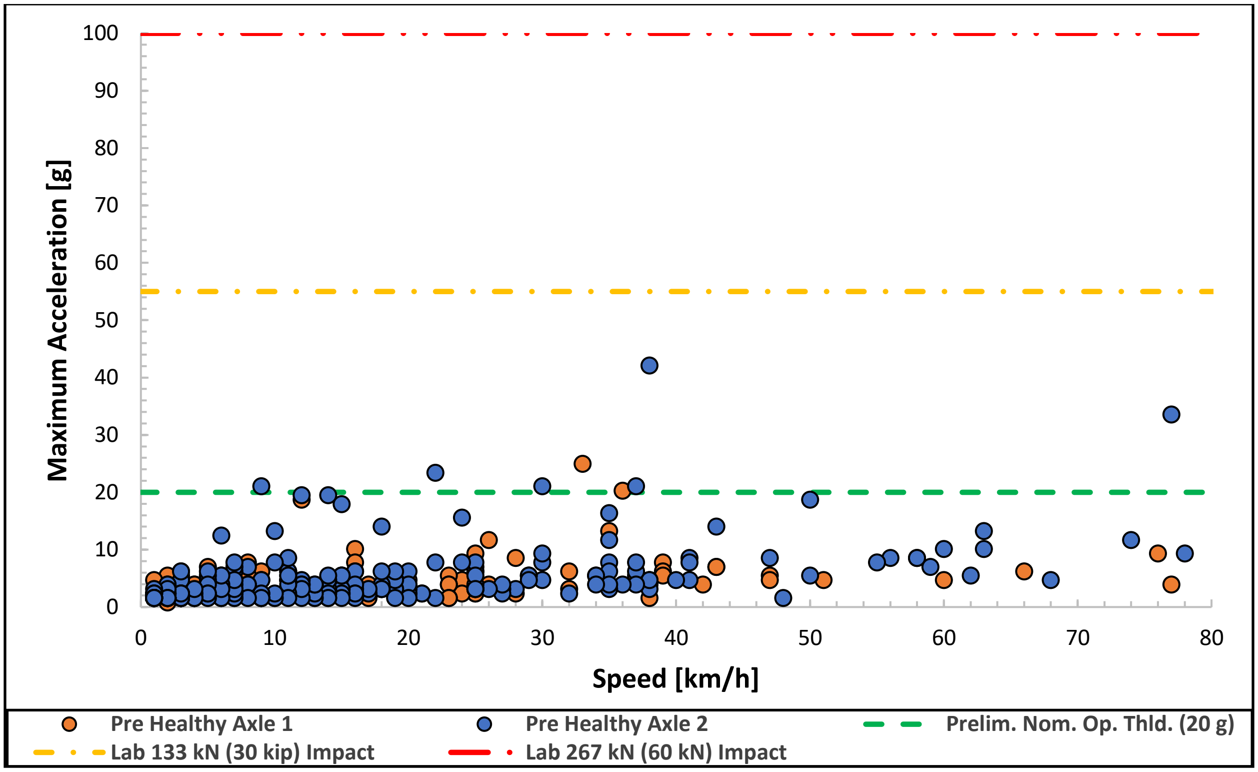

Figure 48. Healthy Axle 1 and 2 maximum acceleration [g] values pre-changeout

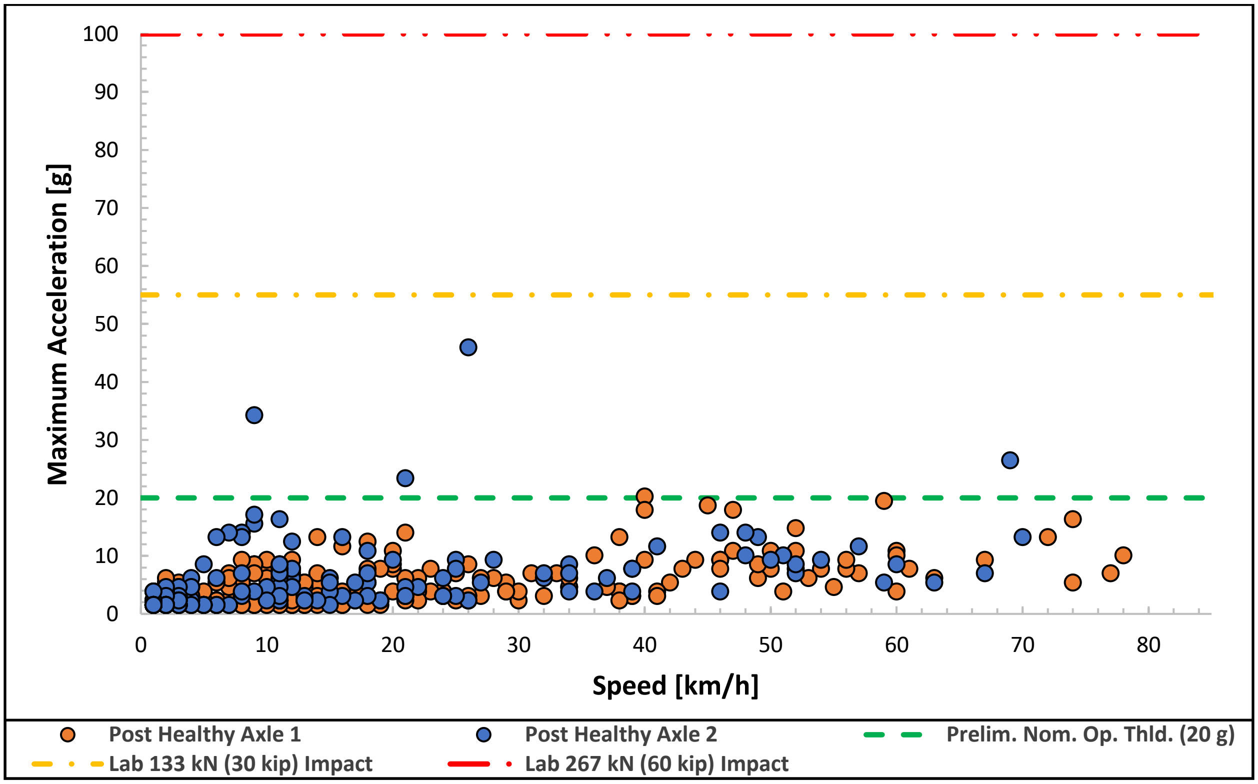

Figure 49. Healthy Axle 1 and 2 maximum acceleration [g] values post-changeout

Unlike the healthy Axle 2, a smaller set of data was acquired for the defective Axle 2 wheelset post-changeout, as seen in Figure 51. This impeded a robust analysis to be performed between the exchanged axles of the Axle 2 position. Yet, comparing Figure 50 and Figure 51, it can still be observed that, at the 30 to 40 km/h (19 to 25 mph) speed range, the maximum g values decreased below the proposed nominal wheel health index of 20g.

Nonetheless, by juxtaposing Figure 48 and Figure 49 onto Figure 50, the non-normative wheelset behavior for Axle 2 is clear. Furthermore, superposition of the previously discussed maximum g thresholds onto Figure 50 clearly map the transition of the wheelset into all the denoted maximum g limits until reaching the FRA advised maintenance stage around 50 km/h (31 mph). The behavior of the data in Figure 50 also shows that the effects of wheel irregularities are amplified with increases in operating speed.

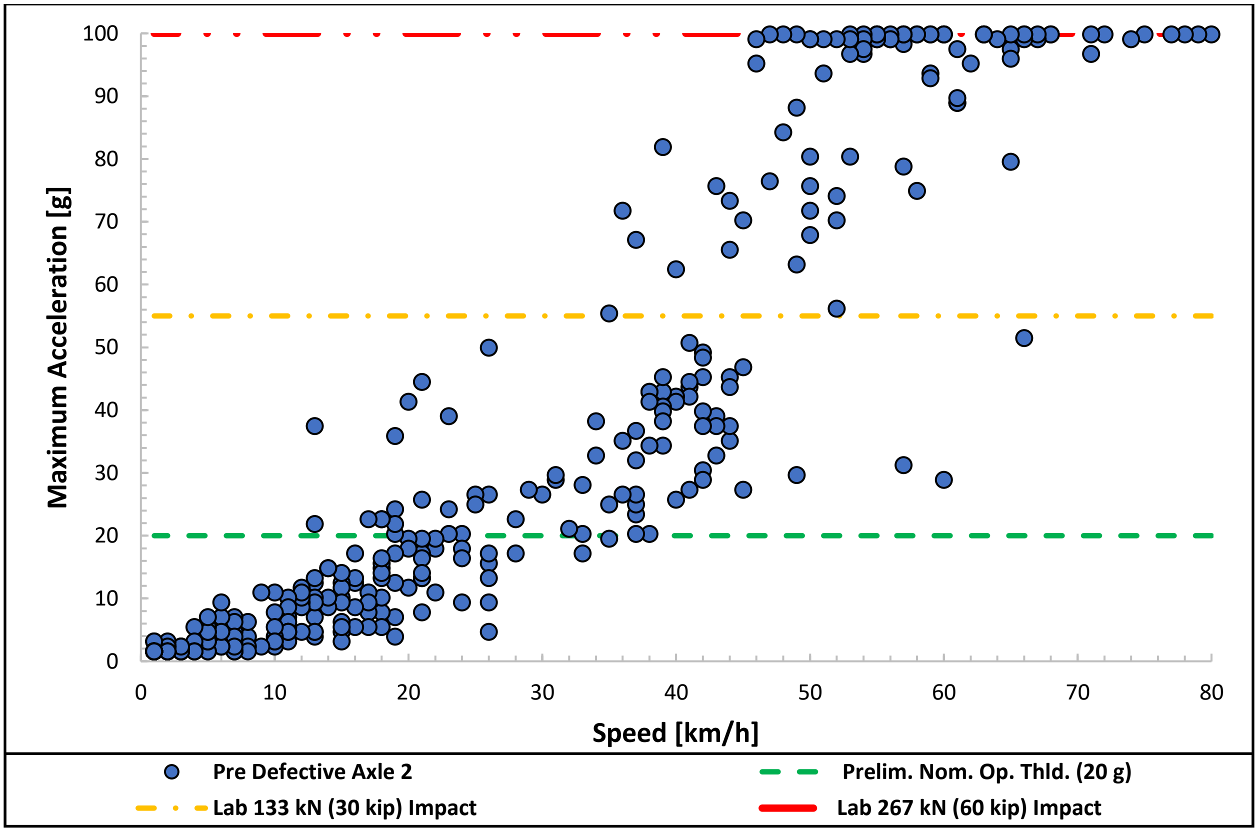

Figure 50. Defective Axle 2 maximum acceleration [g] values pre-changeout

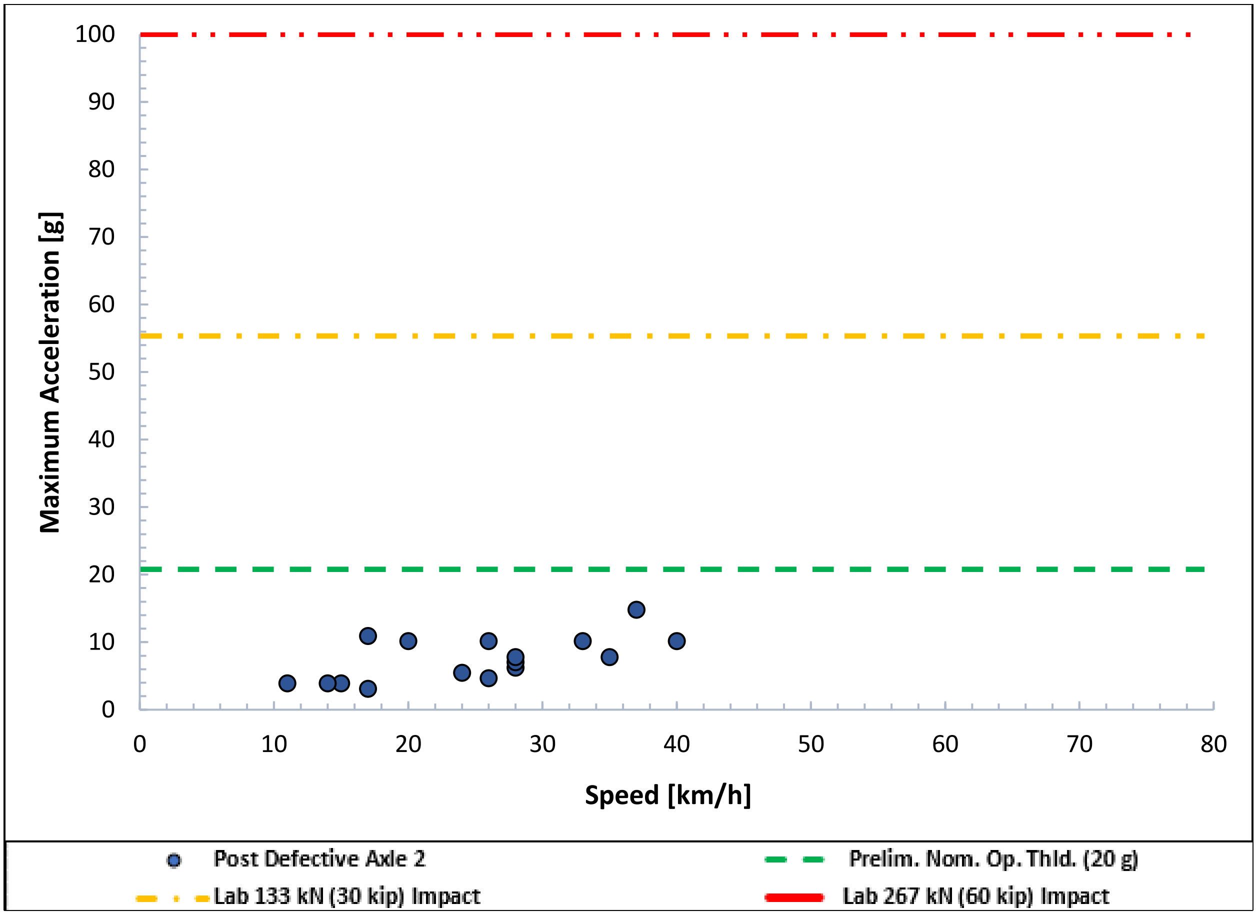

Figure 51. Defective Axle 2 maximum acceleration [g] values post-changeout

Ultimately, Figure 52 provides visual evidence of the wheel flats and spalls found on the defective Axle 2. These defects further justify the maximum g values seen in Figure 50. Reconditioning of the faulty wheelset was deemed improbable as the geometric tolerances of the wheels, in accordance with AAR standards, had met their wear limit. A railcar wheel rim requires a minimum thickness of 1 inch and the defective Axle 2 wheelset was found to have reached this condemning limit [25]. Therefore, the wheelset was discontinued from service.

Figure 52. Defective Axle 2: wheel R2 defects (left) and wheel L2 defects (right)

CHAPTER VII

CONCLUSIONS AND FUTURE WORK

7.1 Test Limitations and Encountered Challenges

Throughout this study, a series of challenges were encountered in the process of evaluating the wheel health monitoring capability of the HUM Boomerang. For instance, the maximum impact frequency output by the impact mechanism was 3 Hz (i.e., 3 hits per second). This impact frequency is the equivalent of a railcar traveling at roughly 31 km/h (19 mph) on a 91.44 cm (36 in) wheelset containing a single defect. Following this dynamic railcar scenario, a railcar will experience a unique impact frequency at each speed it operates. For the experiments performed on the single bearing tester (SBT), wheel impact simulations were conducted at operating speeds of 40, 65, and 85 km/h with a 3 Hz impact. However, in order to exactly mimic the behavior seen in field service, the imposed impact frequencies at each tested speed should have consisted of 3.9, 6.2, and 8.3 Hz, respectively, for a 91.44 cm (36 in) diameter wheel. Even though the experimental approach was conservative in nature, the laboratory testing demonstrated that the accelerometer sensor embedded in the HUM Boomerang was able to detect the maximum impact frequencies associated with a potential defective wheel even when operating at speeds as low as 31 km/h.

The impact tester also posed some limitations. The original design was previously used utilizing a maximum impact frequency setting of 1 Hz (i.e., 1 hit per second). With the introduction of a 3 Hz impact frequency, the mechanism presented some structural design flaws that prevented prolonged impact testing. Therefore, three re-engineering practices were carried out to remediate the observed deficiencies.

The first involved the redesigning of the impact head to maintain the brass pinned disk from ejecting while in operation. The solution was to bore the top of the impact head into two bore levels: (a) one to secure the pin, and (b) the other to secure a portion of the disk. Only a fraction of the brass disk structure would protrude from the impact head, which was sufficient for contact with the axle impact ring when in operation.

Second, the impact rod incorporated a threaded end where the impact head would be fastened like a nut on a bolt. However, after a few seconds of sustained impacts, the threads would deteriorate and cause the impact head to slide which affected the consistency and repeatability of the impacts and, thus, the data output. To solve this issue, the impact rod threaded end was relieved of its threads and machined to a diameter of 14 mm (9/16 in). The threads at the connecting end of the impact head were also eliminated to create a cylindrical cavity of 19 mm (3/4 in) in diameter and 22 mm (7/8 in) in depth. Based on the successful implementation of Delrin plastic in a past UTCRS study involving cyclic loading and the mechanical properties of the material [51], the acetal homopolymer was used to create a sleeve that coupled the impact rod and head in a pressure-fitted fashion. This design modification eliminated the thread deterioration issue and enabled prolonged data acquisition procedures.

The third design modification performed on the impact mechanism involved the lever and cam contact point. Before the upgrade, the end of the lever in contact with the cam included three steel yoke roller bearings. The bearings would facilitate the transfer of energy between the components once the system was in operation. However, because the cam was also machined steel, the bearings, being less robust, would shatter after a few test trials. Like the impact thread fix, Delrin plastic was used to resolve the issue by replacing the bearings in their function. A 25 mm (1 in) long roller with a 25 mm (1 in) diameter was machined, including a 6 mm (1/4 in) hole bored out of the cylinder to allow the rotation of the roller on a stainless-steel hex bolt on which the yoke bearings previously rotated.

Nevertheless, even though the design modifications implemented on the impact mechanism significantly improved the functionality and life of the mechanism, the concern of unforeseeable delays due to a possible structural malfunction were still present. This led to the next and final encountered challenge -- data acquisition duration. Both the HUM Boomerang and the UTCRS wireless modules have an internal clock that enables both systems to transmit data at specific time intervals. The duration of these data relay cycles can be tailored to convey information at reduced stretches, yet only to a certain degree. As some of the data inquiry codes used for the experiments required prolonged intermissions, the severity of the impacts elevated apprehension as to whether their hammering intensity could cause unintended maintenance interludes within a test. For this reason, the course of action was to optimize the amount of data collected, thus, minimizing the wear on the impact system while still permitting sufficient data sets to be acquired for an adequate validation of the wireless condition monitoring modules.

7.2 Conclusions

Despite the experienced hurdles, the high wheel impact detection capability of the HUM Boomerang was successfully validated. The prototype sensor module distinguishably detected high wheel impacts in the laboratory even with the presence of defective bearings at both unloaded and loaded railcar operating conditions. Wheel impact detection was also achieved at various railcar speeds (i.e., 40 to 85 km/h). However, Accelerometer 2 in the HUM Boomerang could not reliably detect the impacts at the highest test speed for a fully loaded bearing containing a cup defect (i.e., cup spall). Nonetheless, with the notional adoption of this sensor and the implementation of current rail industry maintenance protocols, the abnormal behavior of either wheel or bearing would warrant the removal of the entire wheelset for later disassembly and visual inspection. In other words, regardless of the component in distress as identified by the wireless onboard sensor module, whether it be the bearing or the wheel, continued operation of either could propose a potential risk for property and safety. Furthermore, as diverse entities coordinate these wheel removal procedures, established protocols constrain individual wheelset components to be interchanged on-site.

In Chapter VI, the inclusion of an electronic filter for future HUM Boomerang optimization was also investigated. The results of this assessment demonstrated noise reduction in the acquired data as maximum g levels were suppressed. The latter did not affect wheel impacts from being detected, rather, the suppressed signal offered a better distinction between impact and defective bearing conditions. Overall, the results promoted that the possible mechanical noise susceptibility of the Boomerang in the field could be mitigated. Another matter of interest within Chapter VI was assessing the capability of the UTCRS Level 2 algorithm in determining defect type despite the presence of wheel impacts. The algorithm successfully detected the cone spall defect of Experiment 245 under both filter and no filter conditions, but the application of a filter displayed appreciably better results. For the cup spall defect test of Experiment 246, the algorithm was not able to correctly diagnose the defect without a filter while the filtered trials realized proper diagnoses of the cup defect. The aforementioned results further justify the importance of an integrated signal processing filter as noisier signal outputs may result in false positives. Other possible factors that may lead to an erroneous defect type diagnosis include the sampling rate and the position of the defect in respect to the sensor location.

Sampling at higher rates can provide increased accuracy in defect type recognition as more data is available for the algorithm to analyze. Positioning the wireless module to vertically align with the bearing center may have improved resolution to capture cup defects. For cone defects, sensor alignment is not a factor in defect recognition as the defect is not fixed like in the case of a cup defect but is rotating with the cone assembly. The slight imprecision of the wireless module in detecting bearing defect type, nevertheless, highlights why the incorporation of an electronic filter to the HUM Boomerang prototype is highly recommended.

Moreover, the conducted pilot field study correspondingly verified the efficacy of the HUM Boomerang as an abnormal wheel performance prognosis led to the removal of a faulty wheelset. After inspection, the flagged axle was deemed as unfit for service operation as the wheel profiles lacked adherence to AAR standards. In turn, this provided physical evidence of the capability of the HUM Boomerang in providing accurate and critical wheel health metrics. Although additional field and laboratory tests are needed to continue optimizing the module for its official integration into the railway industry, the presented findings support the HUM Boomerang as a prospective onboard wheel health monitoring tool for rail service operations.

7.3 Future Work

Testing of additional springs with varied spring constants would allow for optimization of the preliminary predictive wheel health indices delineated in this work. Ideally, maximum g to kip correlations could serve as embedded wheel health gauge thresholds in the HUM Boomerang to provide optimized wheel life expectancy feedback for future field deployments. In addition, the inclusion of wheel impact vibration signatures into the UTCRS Level 2 algorithm database can also be grounds for future work, creating another tier of defect recognition within the algorithm.

Although the wheel detection efficacy of the HUM Boomerang was validated, pilot field tests in which the railcars retrofitted with the HUM Boomerang technology pass through multiple WILD sites during their service operation can be greatly beneficial. Validation of the maximum g to kip correlations seen in the laboratory could improve the agreement between the field and laboratory results. Moreover, pilot tests involving the employment of both accelerometers (i.e., A1 and A2) for the HUM Boomerang are also needed. As seen in the laboratory evaluation, Accelerometer 1 (A1) had superior wheel impact detection capability as compared to Accelerometer 2 (A2). However, unlike A1 which has a maximum acceleration range of 100g, A2 has a maximum range of 200g, which means that it can capture higher vibration levels of generated by wheel impacts. Hence, deployment of both A1 and A2 accelerometers would guarantee the accuracy in wheel analytics being transmitted. Overall, combining WILD data with the outputs from both A1 and A2 accelerometers can lead to a better understanding of wheel dynamics in field service. The latter information can be used for additional refinements and optimizations of the HUM Boomerang condition monitoring technology.

Lastly, the limitations created by the variable frequency drive (VFD) and the impact mechanism call for a redesign in the way high wheel impacts are simulated in the laboratory. An ideal design would include an integrated user interface (UI) where impact force and frequency selection would be dependent on the testing interests of the user instead of spring substitutions and VFD limited frequency inputs.

REFERENCES

[1] “Freight Rail Overview.” [Online]. https://railroads.dot.gov/rail-network-development/freight-rail-overview [Accessed 3 October 2021].

[2] “AAR United States Rail Fast Facts for 2019.” [Online]. https://www.aar.org/wp-content/uploads/2021/02/AAR-United-States-Fact-Sheet.pdf [Accessed 3 October 2021].

[3] “Economic and Fiscal Impact Analysis of Class I Railroads in 2017.” [Online]. https://www.aar.org/wp-content/uploads/2018/11/AAR-Class-I-Railroad-Towson-Economic-Impact-October-2018.pdf [Accessed 3 October 2021].

[4] “2020 Census Statistics Highlight Local Population Changes and Nation’s Racial and Ethnic Diversity.” [Online]. https://www.census.gov/newsroom/press-releases/2021/population-changes-nations-diversity.html [Accessed 4 October 2021].

[5] “U.S. Census Bureau Today Delivers State Population Totals for Congressional Apportionment.” [Online]. https://www.census.gov/library/stories/2021/04/2020-census-data-release.html [Accessed 4 October 2021].

[6] “North American freight rail cars in service from 2009 to 2020, by car type.” [Online]. https://www.statista.com/statistics/571343/number-of-north-american-freight-rail-cars-by-type/ [Accessed 4 October 2021].

[7] “Introduction to Rail Transportation.” [Online]. https://web.engr.uky.edu/~jrose/papers/REES%202012%20Introduction.pdf [Accessed 4 October 2021].

[8] “Freight & Tank Car Parts.” [Online]. https://www.progressrail.com/en/Segments/RollingStock/FreightParts.html. [Accessed 2 December 2021]

[9] Desai, Rajiv. *Train Wheel*. October 28, 2017. [Online]. https://drrajivdesaimd.com/2017/10/28/derailment/comment-page-1/. [Accessed 2 December 2021].

[10] *Manual of Standards and Recommended Practices Wheels and Axles*. M-107/M-208, Association of American Railroads, 2016.

[11] Karttunen, Kalle. *Influence of Rail, Wheel and Track Geometries on Wheel and Rail Degradation*. 2015. Chalmers University of Technology, Thesis. Chalmers Library, https://publications.lib.chalmers.se/records/fulltext/216927/216927.pdf

[12] Yan, Quan S., et al. "Wheel–rail Wear Investigation on a Heavy Haul Balloon Loop Track through Simulations of Slow Speed Wagon Dynamics." *Transport*, vol. 33, no. 3, 2018, pp. 843-852. http://dx.doi.org/10.3846/16484142.2017.1355843.

[13] *Wheel defects – Code of Practice.* Rail Industry and Standards Board. [Online]. https://www.rissb.com.au/wp-content/uploads/2020/08/2020_08_Wheel-defects_CoP_PC.pdf. [Accessed 20 November 2021].

[14] "NRC Publications Archive (Archives Des Publications DU CNRC)." [Online]. https://nrc-publications.canada.ca/eng/view/ft/?id=99071dbf-48a1-4b41-bd27-14c0730bdc0e. [Accessed 20 November 2021].

[15] Government of Canada, Transportation Safety Board of Canada. "Rail Transportation Safety Investigation Report R18W0007." *Transportation Safety Board of Canada*, / Transportation Safety Board of Canada, 5 Dec. 2019, https://www.bst-tsb.gc.ca/eng/rapports-reports/rail/2018/r18w0007/r18w0007.html. [Accessed 20 November 2021].

[16] "Rail/Weld Failures.", [Online]. https://www.iricen.gov.in/ModelRoom/X5_Tyre%20Defects.html. [Accessed 30 November 2021].

[17] Nielsen, J. C. O., Johansson, A. "Out-of-round railway wheels-a literature survey.", *Proceedings of the Institution of Mechanical Engineers, Part F: Journal of Rail and Rapid Transit*, vol. 214 (F2), 2000, pp. 79–91.

[18] Fesharakifard, Rasul, et al. "Dynamics of Railway Track Subjected to Distributed and Local out-of-Round Wheels." *Mechanics & Industry*, vol. 14, no. 5, 2013, pp. 347–359., https://doi.org/10.1051/meca/2013074.

[19] Barke, D. W., & Chiu, W. K. "A review of the effects of out-of-round wheels on track and vehicle components." *Proceedings of the Institution of Mechanical Engineers Part F: Journal of rail and Rapid transit*, vol. 219, no. 3, 2005, pp. 151-175., https://doi.org/10.1234/095440905x8853.

[20] "Rail Insider-When a Train Derails, Many Railroads Turn to Contractors to Contain and Clean up Spills. Information for Rail Career Professionals from Progressive Railroading Magazine." Progressive Railroading, [Online]. https://www.progressiverailroading.com/mow/article/When-a-train-derails-many-railroads-turn-to-contractors-to-contain-and-clean-up-spills--13396#:~:text=%E2%80%9CIt%20costs%20a%20railroad%20%2425%2C000,on%20w here%20the%20derailment%20occurs.%E2%80%9D. [Accessed 24 November 2021].

[21] "3.16 – Summary of Train Accidents with Reportable Damage, Casualties, and Major Causes." [Online]. https://safetydata.fra.dot.gov/OfficeofSafety/publicsite/Query/TrainAccidentDamage.aspx [Accessed 3 October 2021].

[22] Stewart, M. F., Flynn, E., Marquis, B., Sharma & Associates. Department of Transportation. Federal Railroad Administration. *An Implementation Guide for Wayside Detector Systems*. Washington: GPO, 2019. Web. 10 Dec. 2020.

[23] United States, Federal Railroad Agency, "Mechanical Inspections and Wheel Impact Load Detector Standards for Trains Transporting Large Amounts of Class 3 Flammable Liquids." Vol.80 Fed. Reg. Page 23318-23321 (April 27, 2015)

[24] "Rail Insider-Railroading in the Laboratory: Recapping TTCI's 17th Annual Aar Research Review. Information for Rail Career Professionals from Progressive Railroading Magazine." *Progressive Railroading*, [Online]. https://www.progressiverailroading.com/mow/article/Railroading-in-the-Laboratory-Recapping-TTCIs-17th-Annual-AAR-Research-Review--30594. [Accessed 24 November 2021].

[25] United States, Department of Transportation, Federal Railroad Administration. "Wheels and tire defects." Code of Federal Regulations, Government Printing Office, 2010, p.457.

[26] Mermec Group. "Wheel Profile and Diameter." *Mermec Group,* 2021, http://staging1.mermecgroup.com/inspect/train-monitoring/87/wheel-parameters.php [Accessed 2 December 2021]

[27] Government of Canada, Transportation Safety Board of Canada. "Railway Investigation Report R14M0002." *Transportation Safety Board of Canada*, / Transportation Safety Board of Canada, 27 Mar. 2018, https://www.bst-tsb.gc.ca/eng/rapports-reports/rail/2014/r14m0002/r14m0002.html. [Accessed 20 November 2021].

[28] Tarawneh, C., Montalvo, J., Wilson, B. "Defect Detection in Freight Railcar Tapered-Roller Bearings using Vibration Techniques." *Railway Engineering Science*, vol. 29, no. 1, 2021, pp. 42-58. http://dx.doi.org/10.1007/s40534-020-00230-x.

[29] Cuanang, J., Tarawneh, C., Amaro, M. Jr., Lima, J., & Foltz, H. “Optimization of Railroad Bearing Health Monitoring System for Wireless Utilization.” Proceedings of the 2020 Joint Rail Conference. 2020. Joint Rail Conference. St. Louis, Missouri, USA. April 20-22, 2020. V001T03A007. ASME. https://doi.org/10.1115/JRC2020-8060

[30] Amaro, M. Jr., Tarawneh, C., Foltz, H., & Garcia, R. A. “Energy Harvesting Device for Powering Onboard Condition Monitoring Modules in Rail Service.” Proceedings of the 2021 Joint Rail Conference. 2021. Joint Rail Conference. Virtual, online. April 20-21, 2021. V001T07A002. ASME. https://doi.org/10.1115/JRC2021-58326

[31] Stratman, Brant, et al. “Structural Health Monitoring of Railroad Wheels Using Wheel Impact Load Detectors.” *Journal of Failure Analysis and Prevention*, vol. 7, no. 3, 2007, pp. 218–225., doi:10.1007/s11668-007-9043-3.

[32] Koenig, Frank, et al. “Condition Monitoring for Airport Baggage Handling in the Era of Industry 4.0.” *Journal of Quality in Maintenance Engineering*, vol. 25, no. 3, 2019, pp. 435–451., https://doi.org/10.1108/jqme-03-2018-0014.

[33] Barman, Jyoti Kumar, and Durlav Hazarika. “Condition Monitoring of NFR Trains with Measurements from a Single Wayside 3D Vibration Sensor.” *IEEE Sensors Journal*, vol. 20, no. 8, 2020, pp. 4096–4103., https://doi.org/10.1109/jsen.2019.2961942.

[34] Sun, Qi, et al. “An On-Board Detection Framework for Polygon Wear of Railway Wheel Based on Vibration Acceleration of Axle-Box.” *Mechanical Systems and Signal Processing*, vol. 153, 2021, p. 107540., https://doi.org/10.1016/j.ymssp.2020.107540.

[35] Anastasopoulos, Athanasios, et al., “Acoustic Emission On-line Inspection of Rail Wheels.” *European Working Group on Acoustic Emission*, 2010.

[36] Bondarenko, V.V., et al. “Experimental Study of the Method and Device for Wheel-Sets Acoustic Monitoring of Railway Cars in Motion.” *Naukovyi Visnyk Natsionalnoho Hirnychoho Universytetu*, no. 4, 2019, https://doi.org/10.29202/nvngu/2019-4/7.

[37] Pau, M, and B Leban. “Ultrasonic Assessment of Wheel—Rail Contact Evolution Exposed to Artificially Induced Wear.” *Proceedings of the Institution of Mechanical Engineers, Part F: Journal of Rail and Rapid Transit*, vol. 223, no. 4, 2009, pp. 353–364., https://doi.org/10.1243/09544097jrrt241.

[38] Cavuto, A., et al. “Experimental Investigation by Laser Ultrasonics for Train Wheelset Flaw Detection.” *Journal of Physics: Conference Series*, vol. 1149, 2018, p. 012015., https://doi.org/10.1088/1742-6596/1149/1/012015.

[39] Yamamoto, Daisuke. “Improvement of Method for Locating Position of Wheel / Rail Contact by Means of Thermal Imaging.” Quarterly Report of RTRI, vol. 60, no. 1, 2019, pp. 65–71., https://doi.org/10.2219/rtriqr.60.1_65.al.

[40] Anderson, Duwayne R. “Detecting Flat Wheels with a Fiber-Optic Sensor.” Joint Rail, 2006, https://doi.org/10.1115/jrc2006-94009.

[41] Wei, Chuliang, et al. “Real-Time Train Wheel Condition Monitoring by Fiber Bragg Grating Sensors.” International Journal of Distributed Sensor Networks, vol. 8, no. 1, 2011, p. 409048., doi:10.1155/2012/409048.

[42] Kepak, Stanislav, et al. “Compact Fiber Optic Trackside Sensor for Rail Vehicle Detection and Analysis.” IFAC-PapersOnLine, vol. 51, no. 6, 2018, pp. 220–224., https://doi.org/10.1016/j.ifacol.2018.07.157.

[43] Wang, Zhi Chen, et al. “A New Monitoring Method of Wheel/Rail Contact Forces Caused by out-of-Round Railway Wheels.” *Applied Mechanics and Materials*, vol. 178-181, 2012, pp. 1125–1130., https://doi.org/10.4028/www.scientific.net/amm.178-181.1125.

[44] Turabimana, Pacifique, and Celestin Nkundineza. “Development of an on-Board Measurement System for Railway Vehicle Wheel Flange Wear.” *Sensors*, vol. 20, no. 1, 2020, p. 303., https://doi.org/10.3390/s20010303.

[45] “Technology.” *Amsted Digital Solutions*, 12 Mar. 2021, [Online]. https://www.amsteddigital.com/technology/. [Accessed 2 December 2021].

[46] “Rail Applications.” *Perpetuum*, 2022, [Online]. https://perpetuum.com/. [Accessed 3 December 2021]

[47] “Wireless Wheel Condition Monitoring.” *Modern Railways*, 24 Mar. 2020, [Online] https://www.modernrailways.com/article/wireless-wheel-condition-monitoring. [Accessed 3 December 2021]

[48] “Harvesting Vibrations Benefits Maintenance.” *International Railway Journal*, 5 Sept. 2018, [Online] https://www.railjournal.com/in_depth/harvesting-vibrations-benefits-maintenance/. [Accessed 3 December 2021]

[49] “Powerail.” *Viezo*, [Online] https://viezo.lt/products/powerail/. [Accessed 3 December 2021]

[50] “Monitoring Train Wheels and Bearings to Improve Operations.” *RailTech.com*, 20 July. 2021, [Online] https://www.railtech.com/digitalisation/2021/07/20/monitoring-train-wheels-and-bearings-to-improve-operations/. [Accessed 3 December 2021]

[51] J.N. Bensen, Energy Harvesting Techniques to Power Onboard railway bearing Condition Monitoring Systems. Master of Science in Engineering (MSE), August 2019.

APPENDIX A

APPENDIX A

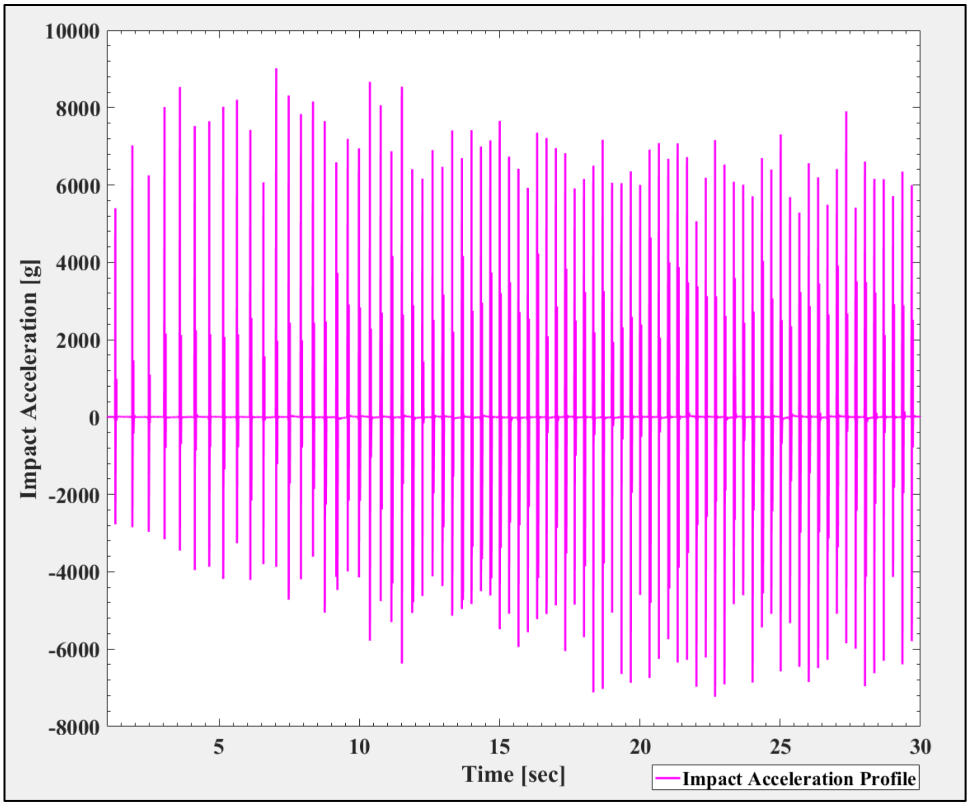

Figure A1. MATLAB generated plot for 51 N/mm (289 lb/in) spring impact acceleration profiles

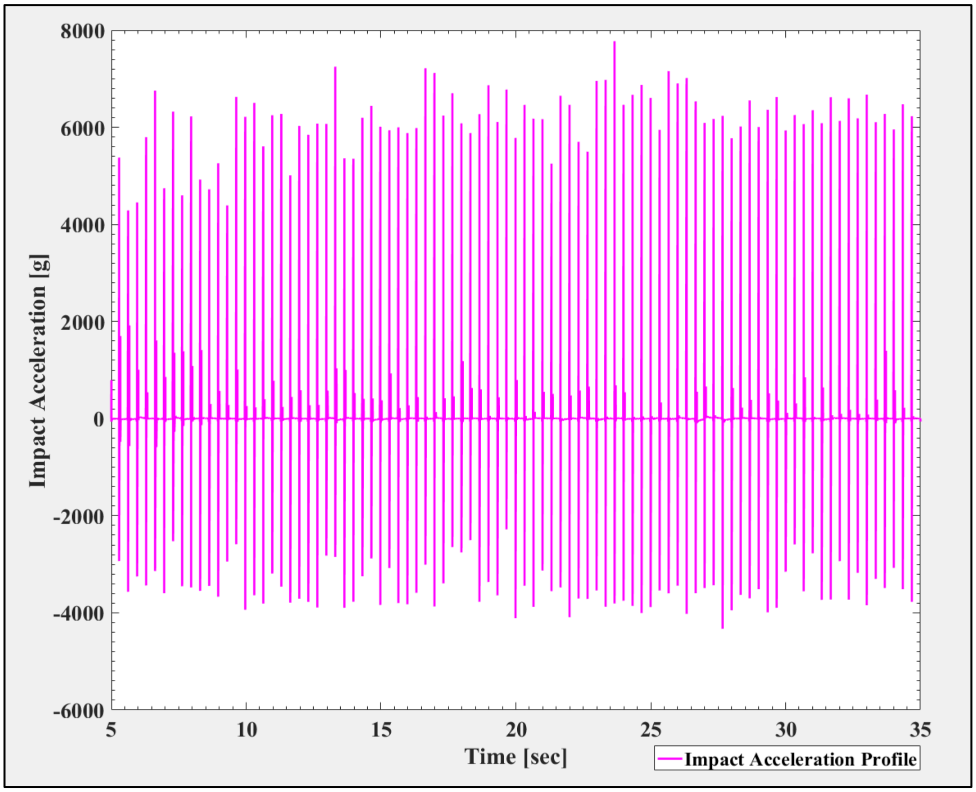

Figure A2. MATLAB generated plot for 44 N/mm (249 lb/in) spring impact acceleration profiles

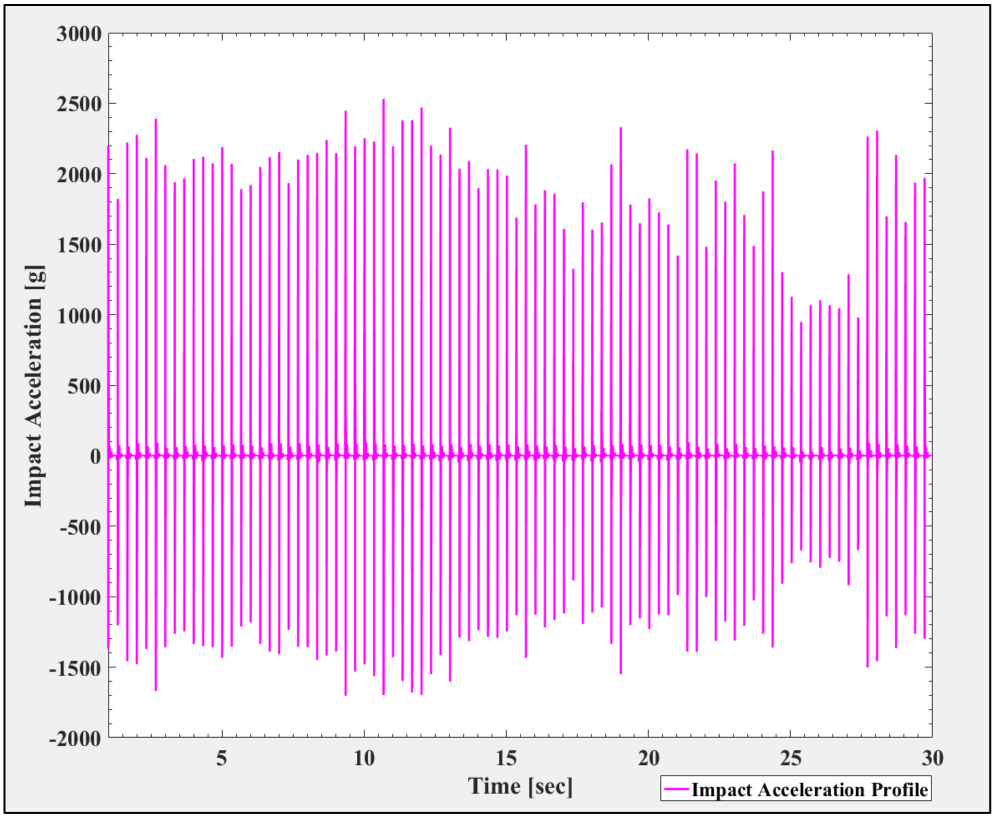

Figure A3. MATLAB generated plot for 26 N/mm (149 lb/in) spring impact acceleration profiles

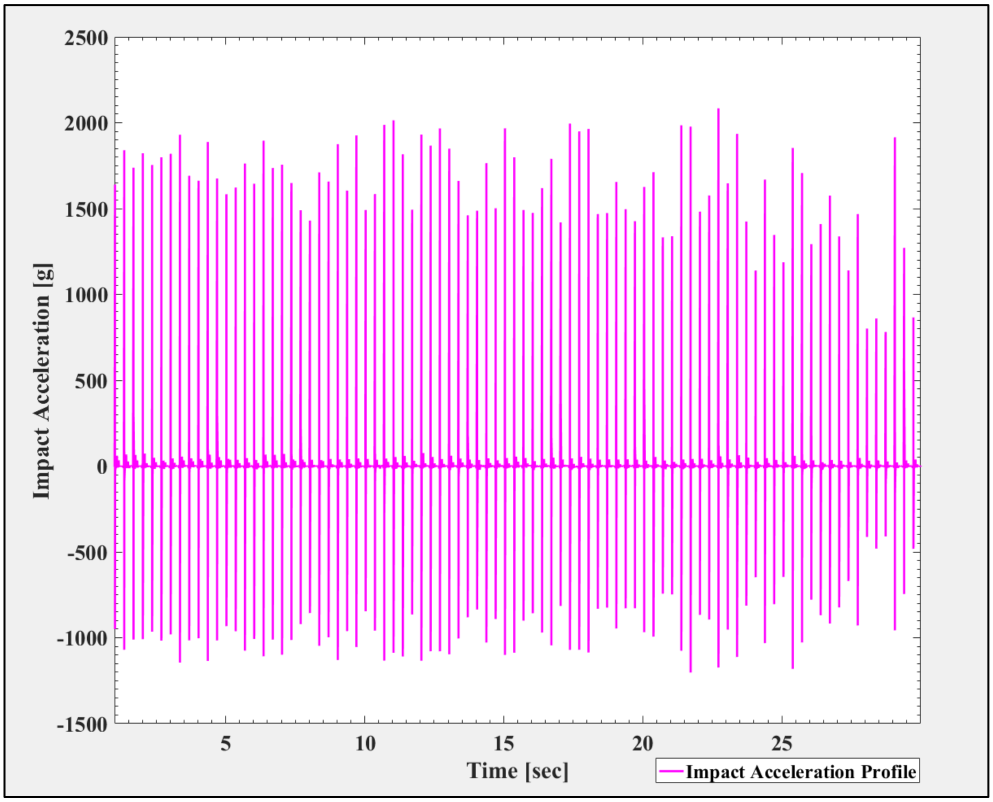

Figure A4. MATLAB generated plot for 18 N/mm (104 lb/in) spring impact acceleration profiles

APPENDIX B

APPENDIX B

No Impact -- Filter						
Speed [km/h] / [mph]	**40 / 25**		**65 / 40**		**85 / 53**	
Railcar Load	17 %	100%	17%	100%	17%	100%
Algorithm Confidence Level [%]	**50**	47	**86**	**96**	**100**	**100**
Defect Type	Cone	Cone	Cone	Cone	Cone	Cone
No Impact – No Filter						
Speed [km/h] / [mph]	**40 / 25**		**65 / 40**		**85 / 53**	
Railcar Load	17 %	100%	17%	100%	17%	100%
Algorithm Confidence Level [%]	**52**	**63**	**76**	**75**	**82**	**58**
Defect Type	Cone	Cone	Cone	Cone	Cone	Cone

Table B1. Experiment 245 Level 2 analysis results using UTCRS Wireless Module (UWM) no impact data with and without an active filter

No Impact -- Filter						
Speed [km/h] / [mph]	**40 / 25**		**65 / 40**		**85 / 53**	
Railcar Load	17 %	100%	17%	100%	17%	100%
Algorithm Confidence Level [%]	**70**	**99**	**80**	**99**	**100**	**100**
Defect Type	Cup	Cup	Cup	Cup	Cup	Cup
No Impact – No Filter						
Speed [km/h] / [mph]	**40 / 25**		**65 / 40**		**85 / 53**	
Railcar Load	17 %	100%	17%	100%	17%	100%
Algorithm Confidence Level [%]	46	**53**	**62**	**72**	**56**	**85**
Defect Type	Cup	Cone	Cone	Cone	Cone	Cone

Table B2. Experiment 246 Level 2 analysis results using UTCRS Wireless Module (UWM) no impact data with and without an active filter

APPENDIX C

APPENDIX C

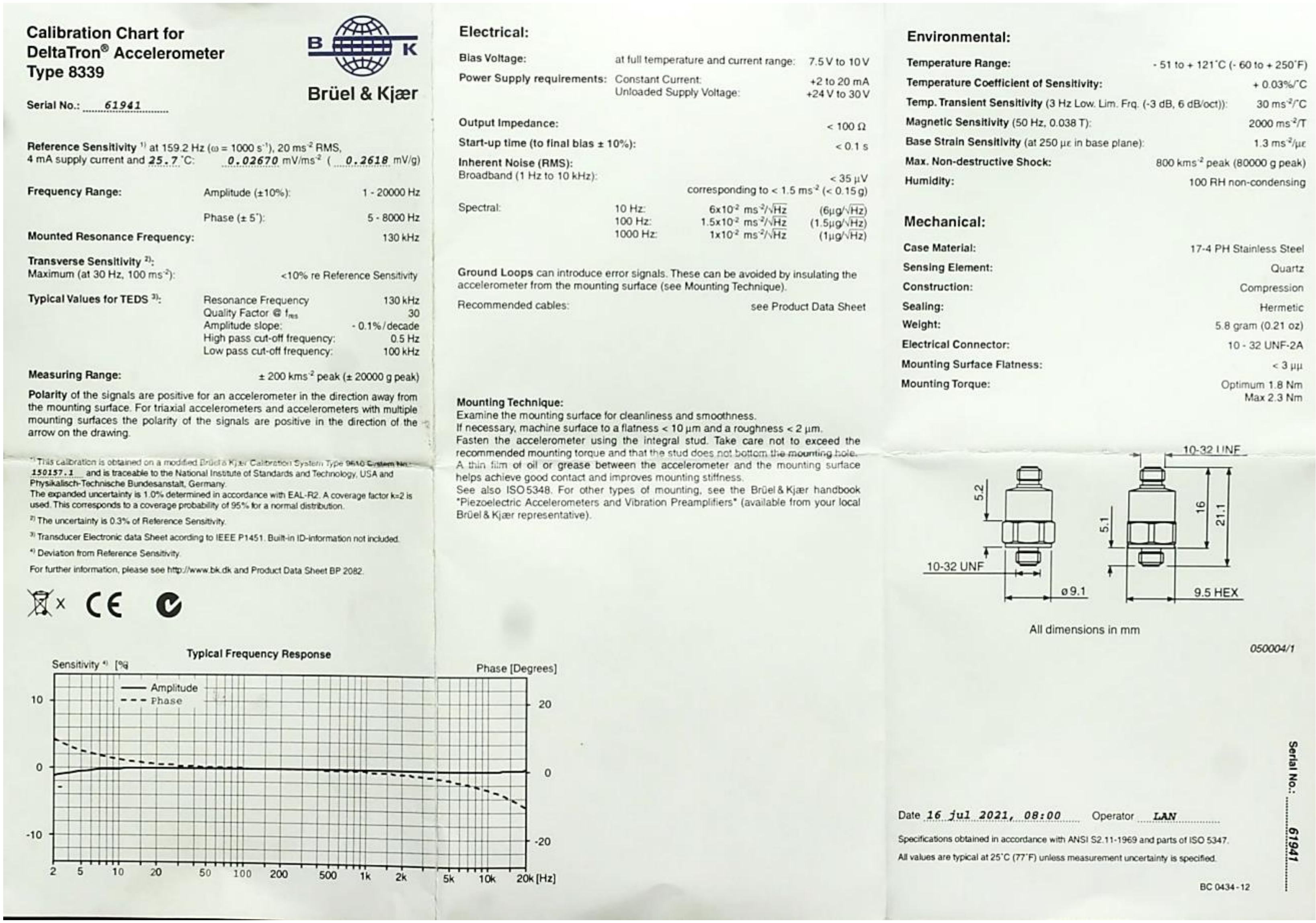

Calibration Chart for DeltaTron® Accelerometer Type 8339

Brüel & Kjær

Serial No.: 61941

Reference Sensitivity [1] at 159.2 Hz (ω = 1000 s^{-1}), 20 ms^{-2} RMS, 4 mA supply current and 25.7 °C: 0.02670 mV/ms^{-2} (0.2618 mV/g)

Frequency Range:	Amplitude (±10%):	1 - 20000 Hz
	Phase (± 5°):	5 - 8000 Hz
Mounted Resonance Frequency:		130 kHz
Transverse Sensitivity [2]: Maximum (at 30 Hz, 100 ms^{-2}):		<10% re Reference Sensitivity
Typical Values for TEDS [3]:	Resonance Frequency	130 kHz
	Quality Factor @ f_{res}	30
	Amplitude slope:	- 0.1%/decade
	High pass cut-off frequency:	0.5 Hz
	Low pass cut-off frequency:	100 kHz
Measuring Range:		± 200 kms^{-2} peak (± 20000 g peak)

Polarity of the signals are positive for an accelerometer in the direction away from the mounting surface. For triaxial accelerometers and accelerometers with multiple mounting surfaces the polarity of the signals are positive in the direction of the arrow on the drawing.

[1] This calibration is obtained on a modified Brüel & Kjær Calibration System Type 9610 System No.: 150157.1 and is traceable to the National Institute of Standards and Technology, USA and Physikalisch-Technische Bundesanstalt, Germany.
The expanded uncertainty is 1.0% determined in accordance with EAL-R2. A coverage factor k=2 is used. This corresponds to a coverage probability of 95% for a normal distribution.

[2] The uncertainty is 0.3% of Reference Sensitivity.

[3] Transducer Electronic data Sheet acording to IEEE P1451. Built-in ID-information not included.

[4] Deviation from Reference Sensitivity.

For further information, please see http://www.bk.dk and Product Data Sheet BP 2082.

Typical Frequency Response

Electrical:

Bias Voltage:	at full temperature and current range:	7.5 V to 10 V
Power Supply requirements:	Constant Current:	+2 to 20 mA
	Unloaded Supply Voltage:	+24 V to 30 V
Output Impedance:		< 100 Ω
Start-up time (to final bias ± 10%):		< 0.1 s
Inherent Noise (RMS): Broadband (1 Hz to 10 kHz):		< 35 µV corresponding to < 1.5 ms^{-2} (< 0.15 g)

Spectral:	10 Hz:	6×10^{-2} $ms^{-2}/\sqrt{Hz}$	(6µg/$\sqrt{Hz}$)
	100 Hz:	1.5×10^{-2} $ms^{-2}/\sqrt{Hz}$	(1.5µg/$\sqrt{Hz}$)
	1000 Hz:	1×10^{-2} $ms^{-2}/\sqrt{Hz}$	(1µg/$\sqrt{Hz}$)

Ground Loops can introduce error signals. These can be avoided by insulating the accelerometer from the mounting surface (see Mounting Technique).

Recommended cables: see Product Data Sheet

Mounting Technique:
Examine the mounting surface for cleanliness and smoothness.
If necessary, machine surface to a flatness < 10 µm and a roughness < 2 µm.
Fasten the accelerometer using the integral stud. Take care not to exceed the recommended mounting torque and that the stud does not bottom the mounting hole.
A thin film of oil or grease between the accelerometer and the mounting surface helps achieve good contact and improves mounting stiffness.
See also ISO 5348. For other types of mounting, see the Brüel & Kjær handbook "Piezoelectric Accelerometers and Vibration Preamplifiers" (available from your local Brüel & Kjær representative).

Environmental:

Temperature Range:	- 51 to + 121°C (- 60 to + 250°F)
Temperature Coefficient of Sensitivity:	+ 0.03%/°C
Temp. Transient Sensitivity (3 Hz Low. Lim. Frq. (-3 dB, 6 dB/oct)):	30 ms^{-2}/°C
Magnetic Sensitivity (50 Hz, 0.038 T):	2000 ms^{-2}/T
Base Strain Sensitivity (at 250 µε in base plane):	1.3 ms^{-2}/µε
Max. Non-destructive Shock:	800 kms^{-2} peak (80000 g peak)
Humidity:	100 RH non-condensing

Mechanical:

Case Material:	17-4 PH Stainless Steel
Sensing Element:	Quartz
Construction:	Compression
Sealing:	Hermetic
Weight:	5.8 gram (0.21 oz)
Electrical Connector:	10 - 32 UNF-2A
Mounting Surface Flatness:	< 3 µµ
Mounting Torque:	Optimum 1.8 Nm Max 2.3 Nm

All dimensions in mm

050004/1

Date 16 jul 2021, 08:00 Operator LAN

Specifications obtained in accordance with ANSI S2.11-1969 and parts of ISO 5347.

All values are typical at 25°C (77°F) unless measurement uncertainty is specified.

BC 0434 - 12

Serial No.: 61941

C1. Brüel & Kjær shock accelerometer (20,000g measuring range) calibration chart

BIOGRAPHICAL SKETCH

Marco Antonio Barrera was born in Harlingen, Texas, US, on July 11, 1997. He is a former San Benito High School alumni who graduated in the top 10% of his class in May 2015. After culminating high school, he attended the University of Texas Rio Grande Valley (UTRGV) where he obtained a Bachelor of Science in Mechanical Engineering with a GPA of 3.91 on May 2019. Marco worked as an undergraduate research assistant for the University Transportation Center for Railway Safety (UTCRS) where he learned from faculty and fellow researchers. In 2019, his hard work and dedication led him to the opportunity of obtaining a scholarship through the Dwight David Eisenhower Transportation Fellowship Program. This fellowship allowed him to present his work at the annual Transportation Research Board in January 2019 where he received the Best Poster Presentation. Upon graduation, he got employed as a Production Engineer for Keppel AmFELS in Brownsville, Texas, US where he assisted the production department in the manufacturing of their Pasha Hawaii-George III & Janet Marie LNG Container Ship projects. In Spring 2020, he took the opportunity to pursue his Master of Science in Mechanical Engineering and returned to UTRGV under a Presidential Graduate Research Assistantship. Here, Marco worked as a graduate research assistant for UTCRS where he also assisted Hum Industrial Technology, Inc. in the evaluation of their rolling stock sensor. He was also an author for a ASME Joint Rail Conference paper in 2022 and obtained his Master of Science in Mechanical Engineering with a 4.0 GPA in May 2022. He can be reached by email at giro1lucioblanco@gmail.com.